The effect of hair bundle shape on hair bundle hydrodynamics of sensory cells in the inner ear

by

Lisa Fran Shatz

Submitted to the Department of Electrical Engineering and
Computer Science
in partial fulfillment of the requirements for the degree of

Doctor of Philosophy

at the

MASSACHUSETTS INSTITUTE OF TECHNOLOGY

May 1996

Author ....
Department of Electrical Engineering and Computer Science
May 3, 1996

Certified by ....
Dennis M. Freeman
Assistant Professor
Thesis Supervisor

Accepted by ....
Frederic R. Morgenthaler
Chairman, Departmental Committee on Graduate Students

The effect of hair bundle shape on hair bundle hydrodynamics of sensory cells in the inner ear

by

Lisa Fran Shatz

Submitted to the Department of Electrical Engineering and Computer Science
on May 3, 1996, in partial fulfillment of the
requirements for the degree of
Doctor of Philosophy

Abstract

Hair cells transduce acoustic or mechanical inputs to electrical signals that are interpreted by the central nervous system. The mechanically sensitive hair bundles come in a variety of shapes and sizes. In vestibular organs hair bundles are relatively long and thin. In auditory organs, hair bundles are an order of magnitude shorter and wider. Also, in auditory organs, hair cells have hair bundles that are graded in height, and the range of frequencies to which these cells are sensitive vary with height—the shorter the hair bundles, the higher the frequency range to which it responds.

We determined the relationship between size and shape of the hair bundle and its sensitivity at asymptotically high and low frequencies. We extended the results of an analysis of hair bundle hydrodynamics in two dimensions to three dimensions. A hemispheroid was used to represent the hair bundle. The hemispheroid had a number of advantages—it could represent shapes that range from thin, pencil-like shapes, to wide, flat, disk-like shapes. Also analytic methods were used in the high frequency range to obtain an exact solution to the equations of motion.

In the low frequency range, where an approximate solution was found using boundary element methods, the symmetry of the hemispheroid was exploited to reduce the number of equations that needed to be solved and so to simplify the numerics. At low frequencies, the sensitivity of the responses of hair cells was mainly proportional to the cube of the heights of their hair bundles, and at high frequencies, the sensitivity of the hair cells was mainly proportional to the inverse of their heights. An excellent match between measurements of sensitivity curves in the basillar papilla of the alligator lizard and the models predictions was found. These results also suggested why hair bundles of hair cells in vestibular organs which are sensitive to low frequencies have ranges of heights that are an order of magnitude larger than the range of heights of hair bundles of hair cells found in auditory organs.

Thesis Supervisor: Dennis M. Freeman
Title: Assistant Professor

Acknowledgments

I would like to thank Professor Freeman and Professor Weiss for giving me a project that was challenging and fun, for helping to improve my writing skills, and for sensitizing me to the importance of details. I would also like to thank Professor White, Professor Brenner of the Chemical Engineering Department and Professor Haber of the Technion Institute. Without their assistance, I expect this thesis would have taken an additional four years to complete.

I would like to thank the members of our cochlear physiology group—C. Quentin Davis, C. Cameron Abnet, Z. Karu, A. J. Aronyosi, and J. Slifka, for their help and support over the years.

I am also very grateful to Professor Rosowski and Professor Peake who taught well and provided me with important assistance in choosing my career path. I am also grateful to J. Balzer who was always nice and helpful.

I am especially, deeply, grateful to my master's thesis adviser, Dr. B. Gold.

A special thanks goes to my children, Ari, Esther, and Adina, who did not complain too much when I had to have a babysitter take care of them.

But most of all I would like to thank Dr. Michael P. Shatz, for not only our extremely useful technical discussions, but for all the love and support and faith he has in me.

Contents

5 Conclusions 143

Chapter 1

Background

1.1 Structure and function of hair bundles

Hair cells transduce the motion of their hair bundles, which is driven by acoustic or mechanical inputs, to electrical signals (Pickles, 1988). Hair cells are found in vestibular organs such as the semicircular canals, the utricle, saccule, and lagena and their signals are interpreted by the central nervous system to control balance and movement. Hair cells are also found in the amphibian papilla, and the basilar papilla of reptiles and birds, and in the cochlea of reptiles, birds, and mammals. In these auditory organs, they operate over a wide range of frequencies and are used to transduce acoustically-driven fluid motion.

The hair cells are attached to the basilar membrane; the hair bundles are surrounded by fluid and are often covered by a gelatinous membrane: the tectorial membrane for auditory organs, the cupula for the semicircular canals, and the otolithic membrane for otolithic organs. Motion of the basilar membrane, motion of the overlying membrane, and motion of the surrounding fluid result in the deflection of the hair bundles. The process by which this happens is not well understood, but previous results suggest that hydrodynamic forces are significant in causing hair bundle motion, and that the shape of the hair bundles influences the hydrodynamics (Freeman and Weiss, 1990a).

1.2 Anatomical studies of hair bundles

A thorough investigation of the anatomical details of hair bundles found in vertebrate inner ears (Lewis et al., 1985) indicated differences in the lengths and shapes of hair bundles. The hair bundles consist of an array of 10 to 220 stereocilia (Figure 1-1). The cross section of the array is often nearly circular, although in the mammalian cochlea, the shape of the cross-section is that of a line segment (for "inner" hair cells) or that of a "v" or "w" pattern (for "outer" hair cells). Stereocilia in each row have the same height, and the heights are graded, giving the hair bundles a "pipe organ" appearance as indicated in Figure 1-2 and Figure 1-3.

Hair bundles tend to be tall (40-120 μm) in vestibular organs and to be short (.8-30 μm) in hearing organs. The range of heights is from .8-120μm, the range of widths is 1-10 μm (Freeman and Weiss, 1988), and the aspect ratio of height to width varies from about 16 for hair cells in the cristae of the semicircular canals (Lewis et al., 1985) to about 0.1 for hair cells in the organ of Corti of the horseshoe bat (Vater and Lenoir, 1992).

The hair bundles of the outer hair cells of echolocating bats are distinctive—these have extremely short heights (.8 μm), a wider "w" pattern, and an exaggerated angle of inclination of the shortest row of stereocilia to the next taller one (Vater and Lenoir, 1992). These distinctions are possibly micromechanical adaptations to ultra-high frequency hearing.

Hair bundle morphology of the basilar papilla of two species of lizards has been thoroughly investigated (Koppl, 1988; Mulroy, 1974; Mulroy and Williams, 1987). In the basilar papilla of the bobtail lizard, the heights range from 6μm at the base to 13μm at the apex, and the number of stereocilia range from 30 in short hair bundles to 42 in tall hair bundles. The basilar papilla of the alligator lizard contains a region of hair bundles that are topped by a tectorial membrane, and a region of hair bundles that are a free-standing. Several differences were observed between the hair bundles of the two regions. In the tectorial region, hair bundles are shorter, have heights that are constant along the length of the papilla, face the same direction, and are

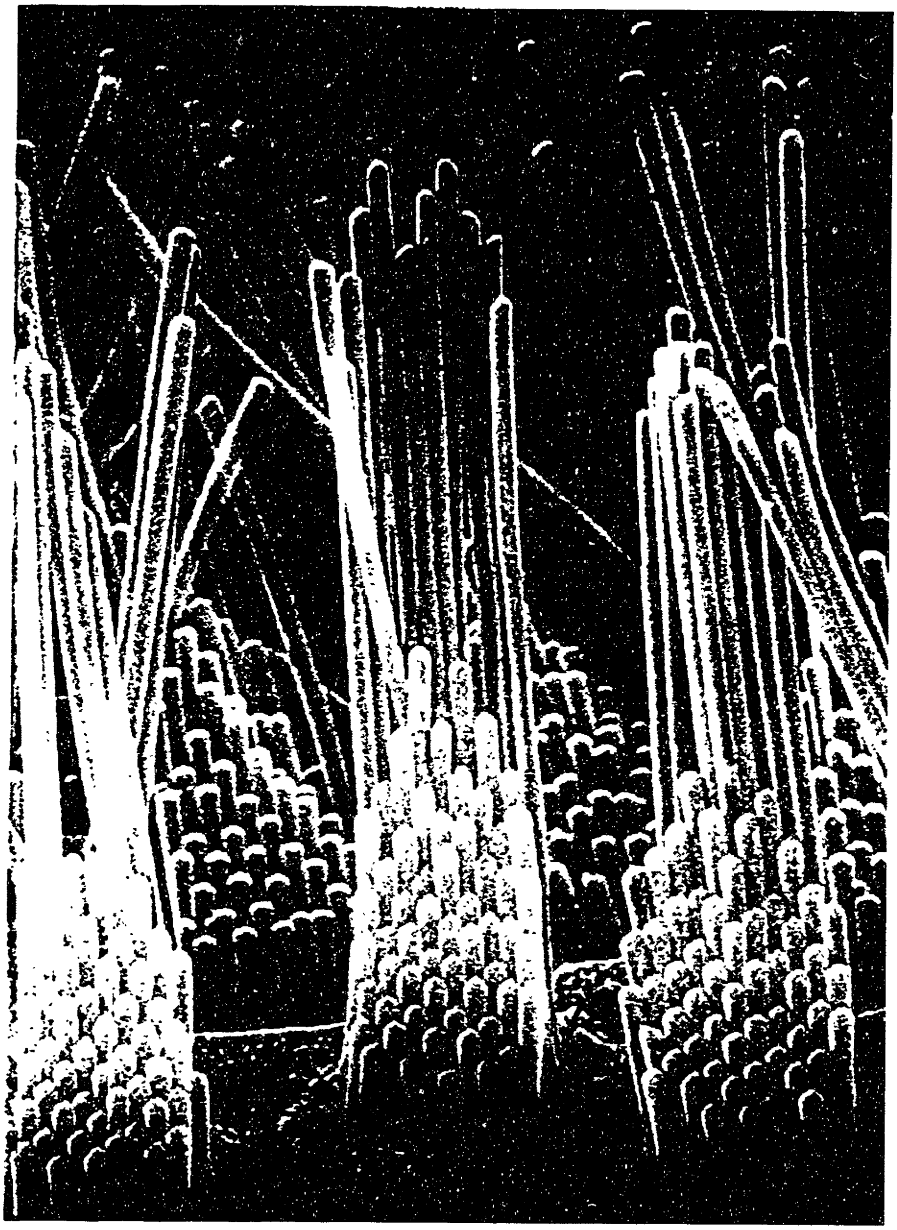

Figure 1-1: A scanning electromicrograph of hair bundles found in the basilar papilla of the alligator lizard. Hair bundles of three hair cells are shown in the foreground. Each hair bundle consists of approximately 60 hairs, organized by length (from about 2 μm to 20 μm for the cells shown here) in an orderly staircase array. Micrograph taken by Ruth Anne Eatock.

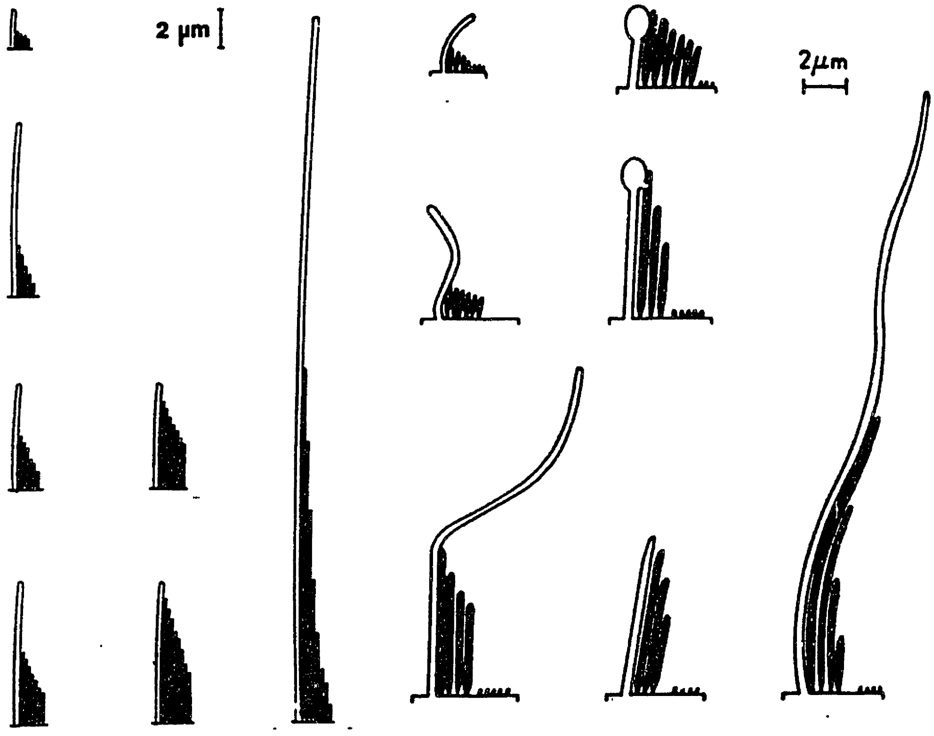

Figure 1-2: Schematic representations of hair bundle types found in vestibular organs of bony fishes, frogs, and lizards (Lewis et al., 1985). The hair bundles consist of an array of stereocilia which are indicated as black, finger-like projections. In vestibular organs, a kinocilium, indicated by the tall, white projection, is present. The aspect ratios (height to width) for the hair bundles depicted here range from ~ 16 to ~ 1.

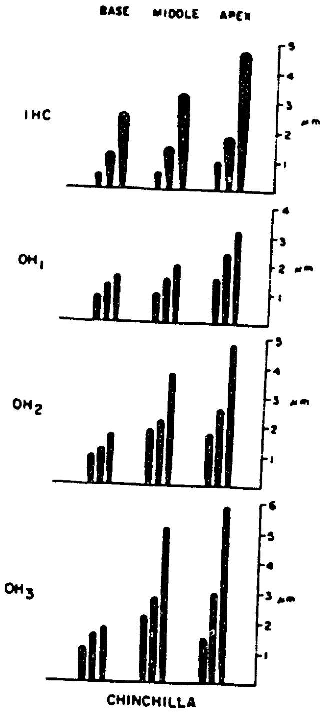

Figure 1-3: Schematic representations of hair bundle types found in the chinchilla cochlea (Lewis et al., 1985). The chinchilla cochlea contains one row of inner hair cells (IHC) and three rows of outer hair cells (OH_1, OH_2, and OH_3). The hair bundles are graded in length from base to apex.

structurally more complicated. In the free-standing region, hair bundles have heights that increase along the length of the papilla. The membrane surface areas of hair bundles in the free-standing region are greater than those of the tectorial region, and are, in fact, proportional to their heights. The hair bundles are also bidirectional in orientation.

1.3 Study of hair bundle motion in the free-standing region of the basilar papilla of the alligator lizard

This section describes observations of hair bundle motion in this free-standing region of the alligator lizard. Because there is no tectorial membrane present the role of hair bundle shape is simpler to assess.

It has been shown that, in auditory organs, hair cells are frequency selective, that is, different hair cells respond more vigorously to different tone frequencies (Pickles, 1988). Studies of hair bundle motion in the free-standing region of the basilar papilla (Figure 1-4) of the alligator lizard suggest that the origin of the frequency selectivity is the hair bundle motion (Frishkopf and DeRosier, 1983; Holton and Hudspeth, 1983). Motion of the hair bundles in the free-standing region can be accounted for by motion of the papilla and motion of the surrounding fluid. It has been shown, however, that motion of the basilar papilla is constant throughout the papilla so that it cannot be papilla movement that is determining the frequency selectivity. Moreover, as in mechanical resonators, "long" hair bundles have lower characteristic frequencies than "short" hair bundles. These results suggest that hydrodynamic forces coupled with mechanical forces of the hair bundles themselves are providing the frequency selectivity.

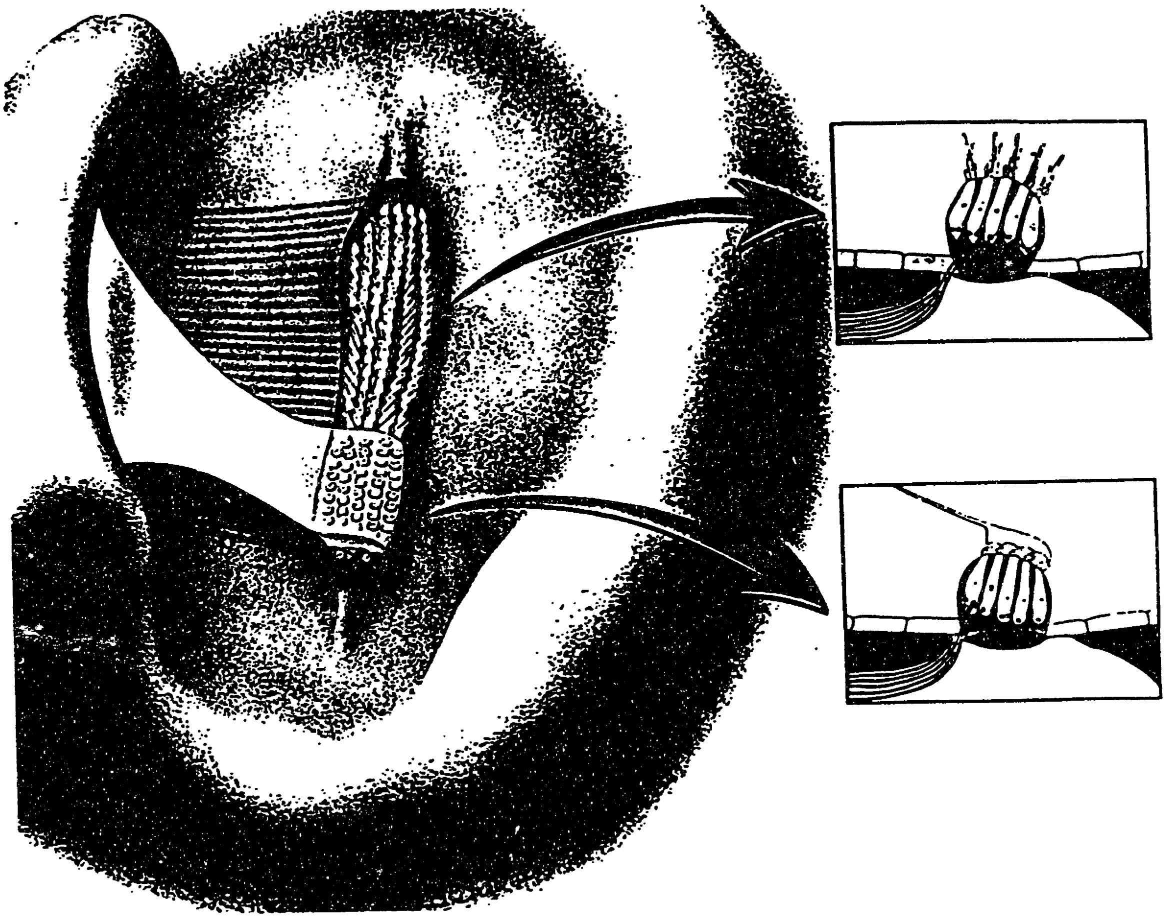

Figure 1-4: A top view of the basilar papilla in alligator lizard (Freeman et al., 1993). There are five rows of hair cells, with nerve fibers that project from the hair cells to the central nervous system. The papilla contains two regions of hair cells: a region with a tectorial membrane and a free-standing region. The insets display a transverse view of the basilar papilla.

1.4 Studies of the hydrodynamics of hair bundle motion

A previous theoretical study (Freeman and Weiss, 1990a) indicated the effects of hair bundle height on the hydrodynamics of hair bundle motion. The hair bundle was represented by a two-dimensional structure shaped as a flap with no overlying membrane present. The hydrodynamics were analyzed as a function of frequency of motion and height of the flap. The results suggest that mechanical and hydrodynamic forces can provide the frequency selectivity observed in the alligator lizard.

Although the 2-D model is very useful in illuminating the hydrodynamics of hair bundle motion, it is limited in important ways. In 2-D motion, the fluid can flow over the flap only. In 3-D motion, fluid can flow both over and around the structure. In addition, shearing forces produce no torque on a flap, since the shear is parallel to the radial vector along the flap. However, in a 3-D body of finite width, shearing forces in addition to pressure forces contribute to the torque. The effect of hair bundle shape was not addressed in the 2-D study. Hair bundles come in various sizes and shapes which surely affect the hydrodynamics.

1.5 Studies of mammalian cochlear mechanics

Unlike motion of the basilar papilla of the alligator lizard, motion of the mammalian organ of Corti is not uniform but frequency selective—different parts of the basilar membrane respond more to different tone frequencies. Moreover, the mammalian basilar membrane does not contain a free-standing region, and although hair bundles are graded in length, mechanical resonances of individual hair bundles are often not considered in models of cochlear mechanics. Instead, the frequency selectivity is mainly attributed to structural changes in the basilar membrane (Zwislocki, 1965; Siebert, 1974; Steele and Taber, 1978). More recent models (Geisler and Sang, 1995; Neely, 1993; Hubbard, 1993) contain active elements. Since the length of outer hair cells of the mammalian cochlea can change in response to a voltage across the cell membrane (Brownell et al., 1985), it has been suggested that outer hair cells can actively enhance the motion of the basilar membrane. Although these models capture many of the characteristics of of cochlear mechanics, no one model can match all experimental observations (Rhode, 1971; Khanna and Leonard, 1982). In this thesis, we explore the role of hair bundle hydrodynamics in the frequency response of hair cells.

1.6 Aims

Our purpose is to extend the previous two-dimensional hydrodynamic study to three dimensions, and study the effects of hair bundle shape on the hydrodynamics. In the 2-D study, the hydrodynamic equations of motion could not be solved exactly for all frequencies, and finite difference methods were used to obtain approximate solutions. Finite difference methods could not be extended to 3-D because discretizing a 3-D volume would result in too many equations to accurately solve. Therefore, in this 3-D study, boundary element methods, which have not been previously used in modelling the hydrodynamics of the inner ear, are used to solve the equations of motion at low frequencies. Boundary element methods reduce the three-dimensional differential equations to two-dimensional integral equations so that only a 2-D area need be discretized. Furthermore, analytic methods, which take advantage of the symmetry of the problem, will be incorporated into the BEM, and will further reduce the number of equations that need to be solved.

We will study the solution to the equations of motion in the limit of low and high frequencies where the equations of motion can be simplified, and we will use these solutions to gain insight into the hydrodynamic consequences of hair bundle shape. We will also compare these results to those of the 2-D study, to determine the validity of the results of the 2-D model. We will incorporate our model into a more general model of ear physiology and compare the model's predictions of sensitivity curves to measurements.

This study investigated the hydrodynamics of hair bundle motion for low and high frequencies. The equations of motion valid for all frequencies have not been solved, since these equations are more difficult to solve. The results of this study, however, can serve as a check on a future solution to the equations of motion for all frequencies.

Results of this dissertation are not only relevent to the field of hearing research but could also prove useful to the field of computational fluid dynamics. Although there are known exact and approximate solutions to the hydrodynamics of full spheroids (Chwang and Wu, 1975), (Pozrikidis, 1989), there are not known solutions for the hydrodynamics of hemispheroids on a plate. These results could also find applications in the field of micromachines, where, as in the inner ear, the dimensions are small, and the linear approximations used in this thesis are appropriate.

Chapter 2

Hemispheroid model of hair bundle mechanics

In this chapter, we describe the hemispheroid model used to represent the hair bundle mechanics. The hemispheroid model is a specific application of a general model of a hair bundle represented by a rigid body of some arbitrary shape developed elsewhere (Freeman and Weiss, 1990b; Freeman and Weiss, 1990c; Freeman and Weiss, 1990d). The general model has already been applied to a 2-D structure shaped as a flap (Freeman and Weiss, 1990a) and the results of that study will be described at the end of this chapter.

2.1 Hemispheroid model

A hemispheroid will represent the shape of the hair bundle (Figure 2-1). This shape was chosen because the shape of the hemispheroid can be easily changed by modifying a single parameter ξ_o which determines the aspect ratio of the hemispheroid (Figure 2-2), and the size of the hemispheroid can be easily changed by varying the focal length L. The hemispheroid was also chosen because the surface of a hemispheroid is a coordinate surface in spheroidal coordinates, and an exact solution to the equations of motion can be derived in the high frequency limit using spheroidal coordinates. An exact solution simplifies the analysis of the effect of shape by clarifying the roles

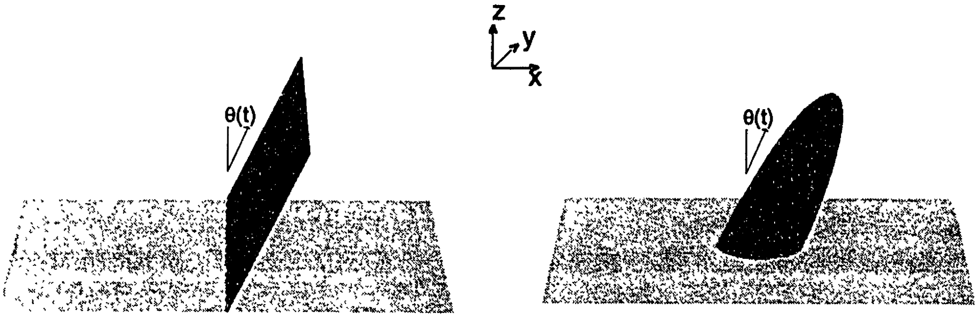

Figure 2-1: A comparison of two and three dimensional models of hair bundles. The flap structure (left) is 2D: it has finite height ($\hat{z}$ direction), zero thickness ($\hat{x}$ direction), and infinite width ($\hat{y}$ direction). The flap is attached to an infinite plate by a spring-loaded hinge. Motions of the structure in the $\hat{x}$ and $\hat{\theta}$ directions cause fluid to flow over the flap. The free-standing hemispheroid (right) is 3D: it has finite dimensions in all three directions. Motions of this structure in $\hat{x}$ and $\hat{\theta}$ cause fluid to flow over and around the hemispheroid.

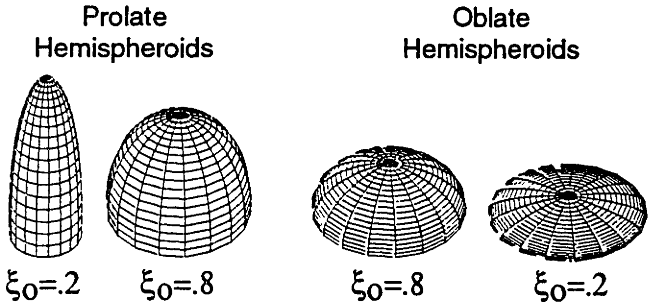

Figure 2-2: The shapes of prolate and oblate hemispheroids are illustrated as a function of the parameter, ξ_o.

of the shape parameter ξ_o and the size parameter L. The properties of hemispheroids will be described in greater detail in Section 2.4.

2.2 Description of model

The hair bundle is modelled as a hemispheroid attached with a compliant hinge to a basal plate that represents the epithelium of the hair cells (Figure 2-1). We assume there is no overlying membrane because this assumption simplifies the analysis, and also because considerable investigation into the properties of hair cells of the free-standing region of the basilla papilla has been performed (Mulroy, 1974; Holton and Weiss, 1983b; Holton and Weiss, 1983a; Frishkopf and DeRosier, 1983; Mulroy and Williams, 1987; Eatock et al., 1993). The basal plate is translating sinusoidally in its plane with magnitude U_b and radian frequency ω. This oscillation results in the hemispheroid translating sinusoidally, and also rotating sinusoidally about the hinge with an angle of rotation, Θ. Motion of the hemispheroid and basal plate results in a torque on the hemispheroid. The torque results from mechanical torques caused by its attachments, and hydrodynamic torques that result from fluid inertial forces and viscous forces.

2.2.1 Equations of motion for the fluid

For infinitesmal motions of the hemispheroid with basal plate, the equations of fluid motion are linear and can be solved in the sinusoidal steady state (Freeman and Weiss, 1990a). Let $\mathbf{U}(\mathbf{r},\omega)$ and $P(\mathbf{r},\omega)$ represent the complex amplitudes of the fluid velocity and pressure, let ρ represent the density of the fluid, μ represent the viscosity of the fluid, ω, represent the radian frequency of vibration in the steady state, and j represent $\sqrt{-1}$. Since fluid momentum is conserved (Landau and Lifshitz, 1959),

$$j\omega\rho\mathbf{U}(\mathbf{r},\omega) = -\nabla P(\mathbf{r},\omega) + \mu\nabla^2\mathbf{U}(\mathbf{r},\omega), \tag{2.1}$$

and since the fluid is incompressible,

$$\nabla \cdot \mathbf{U}(\mathbf{r},\omega) = 0. \tag{2.2}$$

For infinitesimal motions the torque on the hemispheroid is given by (Freeman and Weiss, 1990a)

$$T_h(\omega) = \hat{\mathbf{y}} \cdot \int_S \mathbf{r} \times d\mathbf{F}(\mathbf{r},\omega), \tag{2.3}$$

where

$$d\mathbf{F}(\mathbf{r},\omega) = -P(\mathbf{r},\omega)d\mathbf{S} + \mu d\mathbf{S} \cdot \nabla\mathbf{U}(\mathbf{r},\omega) + \mu\nabla(d\mathbf{S} \cdot \mathbf{U}(\mathbf{r},\omega)), \tag{2.4}$$

r represents a point on the surface of the hemispheroid, S represents the surface, and $d\mathbf{S}$ is in the normal direction to the surface.

2.2.2 Boundary conditions

The equations of motion must be solved subject to boundary conditions. Equation 2.2 requires that normal components of the fluid velocity adjacent to the surfaces of the hemispheroid and the plates be equal to the normal components of the velocities of these structures. The no-slip condition requires that the tangential components of the fluid velocity next to the surfaces equal the tangential components of the velocities of these structures.

In the sinusoidal steady state the velocity of the basal plate is $U_b\hat{\mathbf{x}}$. Because the motions of the hemispheroid are infinitesmal, a stationary boundary approximation can be used (Freeman and Weiss, 1990a). The velocity of a point on the hemispheroid can be described by the sum of a component due to translation of the plate (Freeman and Weiss, 1990d) and a component due to rotation of the hemispheroid about its hinge,

$$\mathbf{U}(\mathbf{r},\omega) = U_b\hat{\mathbf{x}} - j\omega\Theta\sqrt{x^2+z^2}\hat{\theta} \tag{2.5}$$

where Θ is the complex amplitude of the angle the hemispheroid makes with x-y plane.

Far away from the basal plate and hair bundle, the fluid velocity is equal to that which would result if the body were not present. This velocity can be expressed as (Freeman and Weiss, 1990c),

$$\mathbf{U}(\mathbf{r},\omega) = U_b e^{-z\sqrt{\frac{j\omega\rho}{\mu}}}\hat{\mathbf{x}}. \tag{2.6}$$

2.2.3 Use of superposition

The hemispheroid has two distinct modes of motion — translation and rotation. In translation, the plate is translated and the hinge is fixed to the plate so that

$\Theta = 0$. The torque on the hemispheroid is determined by the hydrodynamic transfer function $H_b = T_t/U_b$ where T_t is the torque on the hemispheroid due to a translation of the plate. In rotation, the hemispheroid is rotated about its hinge and the plate is stationary so that $U_b = 0$. The torque on the hemispheroid is determined by the rotational impedence $Z_r = T_r/(-j\omega\Theta)$ where T_r is the torque due to rotation of the hemispheroid about its hinge. T_t and T_r are determined by solving the fluid equations. Because the hydrodynamic equations are linear, the torques due to translation of the plate and rotation of the hemispheroid can be determined separately and then superposed (Freeman and Weiss, 1990d). Therefore the hydrodynamic torque that results for arbitrary combinations of U_b and Θ is

$$T_h = H_b U_b - j\omega Z_r \Theta.$$

2.2.4 Network model

A linear network that represents the components of the torque on the hemispheroid is illustrated in Figure 2-3.

The separation of mechanical forces from hydrodynamic forces minimizes the number of hydrodynamic computations needed to analyze models of hair bundle motion and clarifies the role of fluid forces. The analysis of the hydrodynamic torque is simplified with the use of superposition to separate the computation of the components due to translation of the plate and rotation of the hinge.

The sensitivity transfer function $H_\mu(f)$

The sensitivity transfer function $H_\mu(f) = \Theta/U_b$ describes the response of the hair bundle to hydrodynamic and mechanical torques and can be obtained from the linear network of Figure 2-3,

$$H_\mu(f) = \frac{\Theta}{U_b} = \frac{H_b + H_i}{\frac{1}{C} + j\omega Z_r + j\omega I}. \tag{2.7}$$

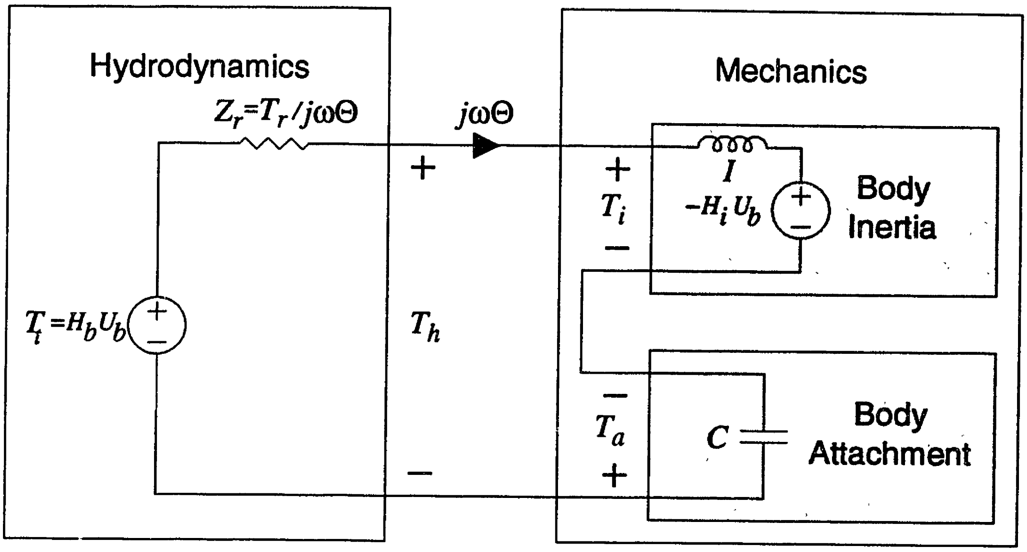

Figure 2-3: A linear network that represents the components of the torque on the hemispheroid. The hydrodynamic torque is represented by a source term, $H_b U_b$ that is proportional to basal plate velocity, and an impedance, Z_r, that is proportional to angular velocity. The mechanics are represented by a mass, I, that represents the moment of inertia of the body, a source, $H_i U_b$, proportional to plate velocity that accounts for the accelerating reference frame, and a compliance, C, that represents the hinged attachment.

Because H_b, H_i, Z_r, and I, are functions of both shape of the hair bundle and frequency, the frequency response of $H_\mu(f)$ will be different for different shapes and for different frequencies.

2.2.5 Hydrodynamic forces on hair bundles for asymptotically low and high frequencies

The equations of motion can be made simpler, and, therefore easier to solve, if we consider asymptotically low frequencies and asymptotically high frequencies.

Hydrodynamic forces on hair bundles for the low frequency asymptote

We can expand the hydrodynamic variables and the boundary conditions in terms of powers of $j\omega$. By equating like powers of $j\omega$, the Navier-Stokes equation reduces to the simpler Stokes equation.

Translational motion. For translational motion the distant boundary condition is given by Equation 2.6. Therefore let us expand the hydrodynamic variables in a power series of $\sqrt{j\omega\rho/\mu}$,

$$\begin{aligned} \mathbf{U}(\mathbf{r},\omega) &= \mathbf{U}_0(\mathbf{r},\omega) + \sqrt{\frac{j\omega\rho}{\mu}}\mathbf{U}_1(\mathbf{r},\omega) + \frac{j\omega\rho}{\mu}\mathbf{U}_2(\mathbf{r},\omega) + \ldots && (2.8) \\ P(\mathbf{r},\omega) &= P_0(\mathbf{r},\omega) + \sqrt{\frac{j\omega\rho}{\mu}}P_1(\mathbf{r},\omega) + \frac{j\omega\rho}{\mu}P_2(\mathbf{r},\omega) + \ldots && (2.9) \\ U_b e^{-z\sqrt{\frac{j\omega\rho}{\mu}}} &= U_b - z\sqrt{\frac{j\omega\rho}{\mu}}U_b + z^2\frac{j\omega\rho}{2\mu}U_b + \ldots \end{aligned}$$

Substituting Equations 2.8 and 2.9 into Equation 2.1 and Equation 2.2, we have, for the zero order term and the first order term, Stokes equation, instead of the linearized Navier-Stokes equation. For the zero order term, the equations of motion can be expressed as,

$$\begin{aligned} \nabla P_0(\mathbf{r},\omega) &= \mu\nabla^2\mathbf{U}_0(\mathbf{r},\omega), \\ \nabla\cdot\mathbf{U}_0(\mathbf{r},\omega) &= 0, \end{aligned}$$

For points along the plate and hemispheroid described by the surface $\mathbf{r} = \mathbf{r}'$,

$$\mathbf{U}_0(\mathbf{r} = \mathbf{r}') = U_b\hat{\mathbf{x}},$$

and far from the body,

$$\mathbf{U}_0(r \to \infty) = U_b\hat{\mathbf{x}}.$$

The solution to the zero order equations is trivial—$\mathbf{U}_0(\mathbf{r},\omega) = \mathbf{U}_b\hat{\mathbf{x}}$ everywhere in the fluid.

For the first order term we have,

$$\begin{aligned} \nabla P_1(\mathbf{r},\omega) &= \mu\nabla^2\mathbf{U}_1(\mathbf{r},\omega), && (2.10) \\ \nabla\cdot\mathbf{U}_1(\mathbf{r},\omega) &= 0, && (2.11) \end{aligned}$$

with boundary conditions along the plate and hemispheroid,

$$\mathbf{U}_1(\mathbf{r} = \mathbf{r}') = 0, \tag{2.12}$$

$$\mathbf{U}_1(r \rightarrow \infty) = -zU_b\hat{\mathbf{x}}. \tag{2.13}$$

The solution to the first order term is non-trivial and requires numerical methods (Brenner, 1995). Since $\omega \rightarrow 0$, only zero order and first order terms are significant.

Rotational motion. To simplify the low-frequency analysis for rotational motion, let us expand the hydrodynamic variables in integer powers of $j\omega$, i. e.,

$$\mathbf{U}(\mathbf{r},\omega) = \mathbf{U}_0(\mathbf{r},\omega) + j\omega\mathbf{U}_1(\mathbf{r},\omega) - \omega^2\Theta^2\mathbf{U}_2(\mathbf{r},\omega) + ... \tag{2.14}$$

$$P(\mathbf{r},\omega) = P_0(\mathbf{r},\omega) + j\omega P_1(\mathbf{r},\omega) - \omega^2 P_2(\mathbf{r},\omega) + ... \tag{2.15}$$

Substituting Equations 2.14 and 2.15 into Equation 2.1 and Equation 2.2, and equating like powers of $j\omega$, we have for the zero order term, $\mathbf{U}_0(\mathbf{r},\omega) = 0$, $P_0(\mathbf{r},\omega) = 0$ everywhere, and for the first order term,

$$\nabla P_1(\mathbf{r},\omega) = \mu\nabla^2\mathbf{U}_1(\mathbf{r},\omega), \tag{2.16}$$

$$\nabla \cdot \mathbf{U}_1(\mathbf{r},\omega) = 0, \tag{2.17}$$

$$\mathbf{U}_1(\mathbf{r} = \mathbf{r}') = \Theta(z\hat{\mathbf{x}} - x\hat{\mathbf{z}}), \tag{2.18}$$

$$\mathbf{U}_1(r \rightarrow \infty) = 0. \tag{2.19}$$

Numerical methods are needed to solve these equations of motion (Brenner, 1995).

Hydrodynamic forces on hair bundles for the high frequency asymptote

In the high frequency range, the boundary layer becomes vanishingly small, so that the fluid can be considered inviscid and hence irrotational (Freeman and Weiss, 1990b). Because viscous forces are negligible, conservation of momentum is expressed by

$$\mathbf{U}(\mathbf{r},\omega) = -\nabla P(\mathbf{r},\omega)/(j\omega\rho). \tag{2.20}$$

Substituting Equation 2.20 into Equation 2.2 we obtain Laplace's equation,

$$\nabla \cdot \nabla P(\mathbf{r}, \omega) = \nabla^2 P(\mathbf{r}, \omega) = 0. \qquad (2.21)$$

We see that in the limit of high frequencies, instead of solving the Navier-Stokes equation, which is a vector equation involving velocity and pressure, we can solve Laplace's equation which is a scalar equation in pressure only. Moreover, for some simple geometries, an exact solution can be obtained.

2.3 Application of the hair bundle mechanics model to a 2-D flap structure

2.3.1 Summary of results

The results of Section 2 have been applied in a two dimensional structure (Freeman and Weiss, 1990a). The rigid body is a flap that extends to infinity in y. The basal plate extends to infinity in both x and y and no overlying plate is present (Figure 2-1 left). Analytic solutions were determined for the hydrodynamic torque, fluid pressure and velocity in the high frequency and low frequency limits. In the mid-frequency range, the results were determined numerically. The effects of hinge compliance, mass of flap, and height of flap on the transfer function Θ/U_b were studied and the results were compared to experimental results measured in the alligator lizard. The results suggested that hydrodynamics can be important in determining the frequency selectivity of hair bundles on the basilar papilla of the alligator lizard.

2.4 Spheroidal coordinates

The simplest way to mathematically describe the surfaces of a hemispheroid on a plate is with spheroidal coordinates. Spheroidal coordinates, represented by ξ, η, and q, are similar to spherical coordinates, represented by r, θ, and q (q is the azimuthal angle, usually labeled ϕ). Figure 2-4 illustrates surfaces of constant r and θ in spherical coordinates and surfaces of constant ξ and η in spheroidal coordinates. In spherical coordinates, surfaces of constant r define spheres; in spheroidal coordinates, surfaces of constant ξ define spheroids. A cross-section of a spheroid in the x-y plane has the shape of a circle; a cross-section of a spheroid in the x-z plane or the y- z plane has the shape of an ellipse. There are two types of spheroids—prolate and oblate. For prolate spheroids, the heights of the cross-sectional ellipses are larger than the widths; for oblate spheroids, the converse is true. As $\xi_o \rightarrow \infty$, both the prolate and oblate spheroids approach a sphere. As $\xi_o \rightarrow 0$, the prolate spheroid becomes pencil-shaped (i.e., its width becomes vanishingly small in the x- and y-directions) whereas the oblate spheroid approaches the shape of a thin disk (i.e., its height in the z-direction becomes vanishingly small). In spherical coordinates, surfaces of constant θ, are half-cones; in spheroidal coordinates, the corresponding surfaces are hyperboloids described by surfaces of constant η. The azimuthal angle q is the same in both coordinate systems and a surface of constant q describes a half-plane in z; $q = 0$ describes the half-plane, $x > 0$, $y = 0$; $q = \pi/2$ describes the half-plane, $x = 0$, $y > 0$. In the limit, as $\xi \rightarrow \infty$, surfaces of constant ξ approach spheres, surfaces of constant η approach half-cones, and spheroidal coordinates become spherical coordinates. Spheroidal coordinates (Moon and Spencer, 1971) are defined for prolate spheroidal coordinates as

$$\begin{aligned} x &= L \sinh \xi \sin \eta \cos q, \\ y &= L \sinh \xi \sin \eta \sin q, \\ z &= L \cosh \xi \cos \eta, \end{aligned} \tag{2.22}$$

and for oblate spheroidal coordinates as

$$\begin{aligned} x &= L \cosh \xi \sin \eta \cos q, \\ y &= L \cosh \xi \sin \eta \sin q, \\ z &= L \sinh \xi \cos \eta. \end{aligned} \tag{2.23}$$

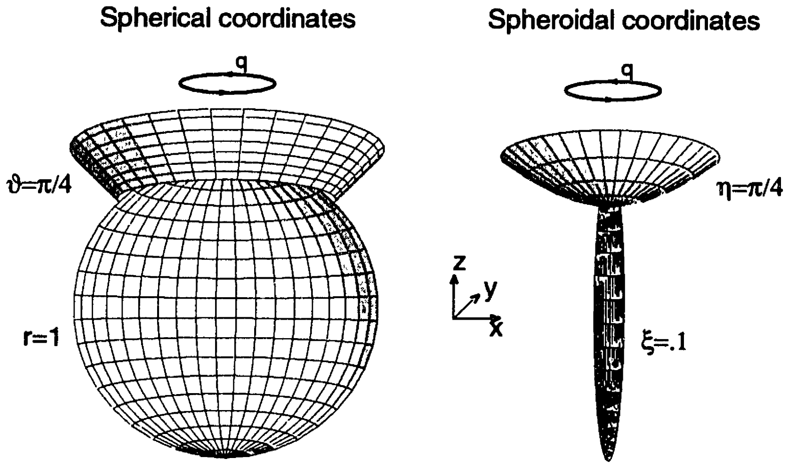
Spherical coordinates

Spheroidal coordinates

Figure 2-4: Left: A surface of constant r describes a sphere and a surface of constant θ describes a half-cone in spherical coordinates.
Right: A surface of constant ξ describes a spheroid and a surface of constant η describes a hyperboloid in spheroidal coordinates.

ξ ranges from 0 to ∞, η ranges from 0 to π, and q ranges from 0 to 2π. An infinitesmal distance is written as

$$(ds)^2 = (h_1 d\xi)^2 + (h_1 d\eta)^2 + (h_2 dq)^2,$$

where h_i are the metric coefficients. For prolate spheroidal coordinates, the metric coefficients are expressed as

$$h_1 = L\sqrt{(\sinh^2 \xi + \sin^2 \eta)}$$

and

$$h_2 = L \sinh \xi \sin \eta.$$

For oblate spheroidal coordinates, h_1 and h_2 are given by

$$h_1 = L\sqrt{(\sinh^2 \xi + \cos^2 \eta)}$$

and

$$h_2 = L \cosh \xi \sin \eta.$$

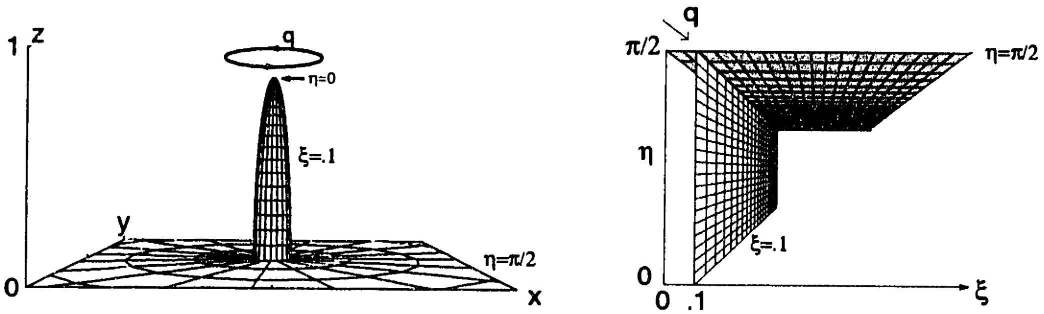

Figure 2-5: The hemispheroid on a plate is defined by a surface of constant ξ and the surface $\eta = \pi/2$. The hemispheroid and plate in rectangular coordinates (left panel) transform to orthogonal planes in prolate spheroidal coordinates (right panel).

In spheroidal coordinates, Laplace's equation is (Moon and Spencer, 1971)

$$\nabla^2\Phi(\xi,\eta,q) = h_1^{-2}\left(\frac{\partial^2\Phi}{\partial\xi^2} + \coth\xi\frac{\partial\Phi}{\partial\xi} + \frac{\partial^2\Phi}{\partial\eta^2} + \cot\eta\frac{\partial\Phi}{\partial\eta}\right) + h_2^{-2}\frac{\partial^2\Phi}{\partial q^2}. \tag{2.24}$$

Hemispheroid and plate

To describe a hemispheroid, we restrict η to range from zero to $\pi/2$. The tip of the hemispheroid is at $\eta = 0$; the base is at $\eta = \pi/2$. Figure 2-5 illustrates the hemispheroid on a plate in rectangular coordinates and in spheroidal coordinates. In rectangular coordinates, the surface of a prolate hemispheroid is described by

$$\frac{x^2+y^2}{(L\sinh\xi_o)^2} + \frac{z^2}{(L\cosh\xi_o)^2} = 1, \text{ for } z > 0,$$

and the surface of an oblate hemispheroid,

$$\frac{x^2+y^2}{(L\cosh\xi_o)^2} + \frac{z^2}{(L\sinh\xi_o)^2} = 1, \text{ for } z > 0.$$

The surface of the plate is described by $z = 0$. In prolate or oblate spheroidal coordinates, the surface of the hemispheroid is described by $\xi = \xi_o$ and the surface of the basal plate is described by $\eta = \pi/2$. So we see that the hemispheroid and plate are coordinate surfaces in spheroidal coordinates.

Chapter 3

High frequency solution

3.1 Introduction

We will show that, in the limit of high frequencies, the full linearized Navier-Stokes equation need not be solved, and the simpler Laplace's equation can be used. We will solve Laplace's equation exactly, using prolate and oblate spheroidal coordinates, and, with that solution, we will derive the hydrodynamic pressure, velocity, and torque. We will study the effects of shape on these hydrodynamic quantities, and we will show that height, width, and focal length are important in determining the hydrodynamic torque in this frequency limit.

3.2 Hydrodynamic model

3.2.1 Hydrodynamic equations

In the high frequency limit, the fluid velocity $\mathbf{U}(\mathbf{r})$ is proportional to the gradient of the pressure (Equation 2.20) and the pressure $P(\mathbf{r})$ is a solution to Laplace's equation (Equation 2.21). To simplify the analysis, let us express $\mathbf{U}(\mathbf{r})$ as the gradient of a scalar velocity potential function $\Phi(\mathbf{r})$,

$$\mathbf{U}(\mathbf{r}) = \nabla\Phi(\mathbf{r}). \tag{3.1}$$

$P(\mathbf{r})$ is then represented by

$$P(\mathbf{r}) = -j\omega\rho\Phi(\mathbf{r}), \tag{3.2}$$

and the velocity potential satisfies Laplace's equation,

$$\nabla \cdot \nabla\Phi(\mathbf{r}) = \nabla^2\Phi(\mathbf{r}) = 0.$$

Laplace's equation must be solved subject to boundary conditions. The normal velocity of the fluid at the surface of the hemispheroid must equal the normal velocity of the hemispheroid. The velocity of the hemispheroid depends on both translation of the basal plate and rotation of the hemispheroid about the hinge. The velocity of a point on the surface is given in Equation 2.5. The normal velocity of the fluid at the surface of the plate must equal the normal velocity of the plate which is zero. In addition, far away from the hemispheroid, the fluid velocity must go to zero.

The hydrodynamic torque $\mathbf{T}_h$ on the hemispheroid is

$$\mathbf{T}_h = -\int \mathbf{r} \times \hat{\mathbf{n}}\mathbf{P}(\mathbf{r})\mathbf{dA}, \tag{3.3}$$

where $\mathbf{r}$ is a vector from the hinge (located at the center of the hemispheroidal surface on the basal plate) to a point on the surface of the hemispheroid, and $\hat{\mathbf{n}}$ is the normal to the surface of the hemispheroid (pointing outward). Due to the reflection symmetry about the x-z plane, the torque has only a y component whose magnitude is T_h.

3.2.2 The velocity potential $\Phi(\mathbf{r})$

Translation of the plate

We first solve Laplace's equation for the fluid motion resulting when the plate is translated in its plane and the hinge is fixed so that the hemispheroid cannot rotate. To solve Laplace's equation in spheroidal coordinates, we need to express the boundary conditions in these coordinates. We will use prolate spheroidal coordinates to derive the solution. The solution in oblate spheroidal coordinates can be obtained from the solution in prolate spheroidal coordinates by letting $\cosh\xi \longrightarrow j\sinh\xi$, and $L \longrightarrow -jL$.

On the surface of the hemispheroid, the normal component of the fluid velocity is equal to the normal component of the velocity of the hemispheroid, $U_b\hat{\mathbf{x}}$, i.e.,

$$\nabla\Phi(\mathbf{r})\cdot\hat{\mathbf{n}} = U_b\hat{\mathbf{x}}\cdot\hat{\mathbf{n}}, \text{ for } \xi = \xi_o.$$

The unit vectors can be expressed as $\hat{\mathbf{n}} = -\hat{\xi}$ and $\hat{\mathbf{x}} = \nabla x$. Taking ∇x in prolate spheroidal coordinates yields

$$\frac{\partial\Phi(\mathbf{r})}{\partial\xi} = LU_b\cosh\xi\sin\eta\cos q, \text{ for } \xi = \xi_o. \tag{3.4}$$

In addition, the normal component of the fluid velocity at the plate is zero,

$$\nabla\Phi(\mathbf{r})\cdot\hat{\mathbf{z}} = 0, \text{ for } z = 0,$$

which in spheroidal coordinates yields

$$\frac{\partial\Phi(\mathbf{r})}{\partial\eta} = 0, \text{ for } \eta = \pi/2. \tag{3.5}$$

At $\xi = \infty$, we impose the condition that the fluid potential is finite.

As shown in the Appendix, the solution to Laplace's equation subject to these boundary conditions is

$$\Phi(\mathbf{r}) = \frac{U_b L \cosh \xi_o}{C_1^1(\xi_o)} Q_1^1(\cosh \xi) \sin \eta \cos q, \tag{3.6}$$

where $Q_1^1(\cosh \xi)$ is an associated Legendre function of the second kind, and

$$C_i^k(\xi_o) = \left. \frac{\partial Q_i^k(\cosh \xi)}{\partial \xi} \right|_{\xi=\xi_o} .$$

A similar solution results for an oblate hemispheroid,

$$\Phi(\mathbf{r}) = \frac{U_b L \sinh \xi_o}{D_1^1(\xi_o)} Q_1^1(j \sinh \xi) \sin \eta \cos q, \tag{3.7}$$

where

$$D_i^k(\xi_o) = \left. \frac{\partial Q_i^k(j \sinh \xi)}{\partial \xi} \right|_{\xi=\xi_o} .$$

For both hemispheroids, $\Phi(\mathbf{r})$ is a product of five terms. The first term is the velocity of the plate (U_b). The second term depends only upon the shape of the hemispheroid through its height ($L\cosh(\xi_o)$ for the prolate hemispheroid and $L\sinh(\xi_o)$ for the oblate hemispheroid) and the shape factor ξ_o. Each of the remaining three terms express the dependence of $\Phi(\mathbf{r})$ on one of the coordinates — ξ, η, and q.

Rotation of the hemispheroid

The boundary condition on the surface of the hemispheroid for the fluid motion resulting from rotation of the hemispheroid while the plate is stationary is

$$\nabla\Phi(\mathbf{r}) \cdot \hat{\mathbf{n}} = -j\omega\Theta\sqrt{x^2+z^2}\,\hat{\theta} \cdot \hat{\mathbf{n}}, \text{ for } \xi = \xi_o, \tag{3.8}$$

which in prolate spheroidal coordinates is

$$\frac{\partial \Phi(\mathbf{r})}{\partial \xi} = L^2 j\omega\Theta \sin \eta \cos \eta \cos q, \text{ for } \xi = \xi_o.$$

The other boundary conditions are the same as for translational motion. As shown in the Appendix, the solution for the prolate hemispheroid is

$$\Phi(\mathbf{r}) = j\omega\Theta L^2 \cos q \sum_{l=0}^{\infty} \frac{I_l}{C^1_{2l+1}(\xi_o)} P^1_{2l+1}(\cos\eta) Q^1_{2l+1}(\cosh\xi), \tag{3.9}$$

where $I_l = \sqrt{\pi}(4l+3)/(8\Gamma(1.5-l)\Gamma(3+l))$. For an oblate hemispheroid, $\Phi(\mathbf{r})$ is

$$\Phi(\mathbf{r}) = j\omega\Theta L^2 \cos q \sum_{l=0}^{\infty} \frac{I_l}{D^1_{2l+1}(\xi_o)} P^1_{2l+1}(\cos\eta) Q^1_{2l+1}(j\sinh\xi). \tag{3.10}$$

The velocity potentials for both the prolate and oblate hemispheroids share several properties. Both are proportional to the product of the angular velocity of the hemispheroid ($j\omega\Theta$) and L^2. As for the solution in response to translation of the plate, both solutions for rotation of the hemispheroid depend upon $\cos q$. In contrast to solutions in response to translation of the plate, both solutions for rotation of the hemispheroid, have a velocity potential that depends upon the shape factor of the hemispheroid and on ξ and η through an infinite sum of Legendre functions.

Because all the hydrodynamic variables (e.g., fluid velocity, torque on the hemispheroid) are computed from the velocity potential, we examined the numerical convergence of the series solution for the velocity potential of a prolate hemispheroid (Equation 3.9) in order to determine the number of terms required to adequately approximate the velocity potential. Since we have a closed form expression for the normal derivative of the velocity potential on the surface of the hemispheroid (Equation 3.5), we compared this value to that derived from the partial sum of the series solution. For convenience, we used the normalized velocity potential defined as $\widehat{\Phi}(\mathbf{r}) = \Phi(\mathbf{r})/(j\omega\Theta L^2 \cos q)$. The normal derivative of the normalized velocity potential on the surface of the hemispheroid is $\widehat{\Phi}'(\mathbf{r}) = \partial\widehat{\Phi}(\mathbf{r})/\partial\xi|_{\xi=\xi_o} = \sin\eta\cos\eta$. We compared this expression to the derivative computed from normalized partial sum based on Equation 3.9, by evaluating $\widehat{\Phi}'_n(\mathbf{r}) = \partial\widehat{\Phi}_n(\mathbf{r})/\partial\xi$ at $\xi = \xi_o$ where $\widehat{\Phi}_n(\mathbf{r})$ is given by

$$\widehat{\Phi}_n(\mathbf{r}) = \sum_{l=0}^{n} \frac{I_l}{C^1_{2l+1}(\xi_o)} P^1_{2l+1}(\cos\eta) Q^1_{2l+1}(\cosh\xi)$$

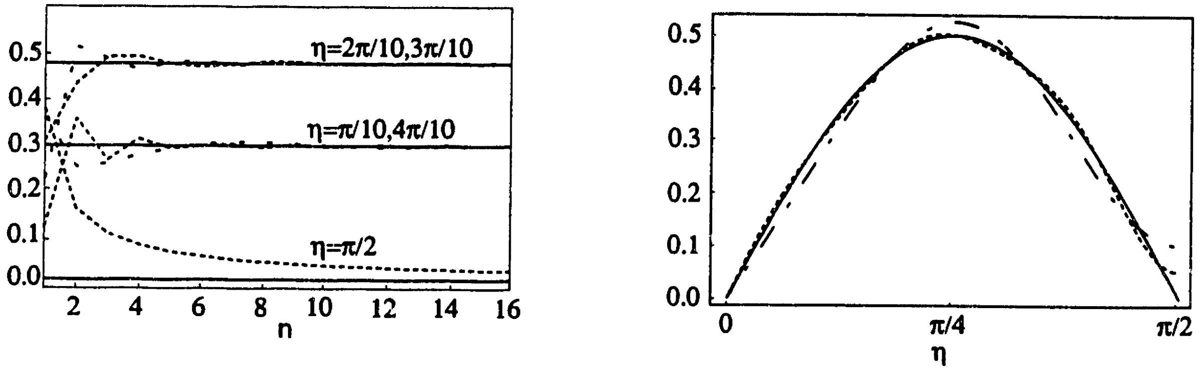

Figure 3-1: A comparison of $\widehat{\Phi}'(\mathbf{r})$ (solid) with $\widehat{\Phi}'_n(\mathbf{r})$ (dashed). The left panel shows the partial derivatives plotted versus n for different values of η. The right panel shows the partial derivatives plotted versus η for $n = 4$ (dot-dash) and $n = 6$ (dash).

for different values of n. The results are shown in Figure 3-1. For values of η other than $\pi/2$, $\widehat{\Phi}'_n(\mathbf{r})$ is within 2% of $\widehat{\Phi}'(\mathbf{r})$ for $n > 4$ terms. The convergence is somewhat slower for $\eta = \pi/2$, where $\widehat{\Phi}'(\mathbf{r}) = 0$. At $\eta = \pi/2$ with $n = 5$, $\widehat{\Phi}'_n(\mathbf{r}) = 0.06$, and with $n = 40$, $\widehat{\Phi}'_n(\mathbf{r}) = 0.008$. To facilitate the computation, subsequent evaluations of $\Phi(\mathbf{r})$ will include only the first five terms.

3.3 The hydrodynamic pressure, fluid velocity, and torque on the hemispheroid

3.3.1 Pressure

Translational motion

The pressure on the hemispheroid surfaces due to translation of the plate can be obtained from Equations 3.2, 3.6, and 3.7. The pressure on a flap and on a sphere are given elsewhere (Freeman and Weiss, 1990a), (Batchelor, 1967). By examining these equations, we see that the pressure varies linearly with the height of the structure which is L for the flap, $L \cosh \xi_o$ for the prolate hemispheroid, $L \sinh \xi_o$ for the oblate hemispheroid and L for the hemisphere of radius L. Thus, it is informative to examine the effect of the shape of the structure on the fluid pressure by normalizing the structures to have the same height. Therefore, we define the dimensionless, normalized pressures on the surface of each structure as $\widehat{P}_{flap}(\mathbf{r}) = P_{flap}(\mathbf{r})/(j\omega\rho U_b L)$ for the flap, $\widehat{P}_{prolate}(\mathbf{r}) = P_{prolate}(\mathbf{r})/(j\omega\rho U_b L \cosh \xi_o)$ for the prolate hemispheroid, $\widehat{P}_{oblate}(\mathbf{r}) = P_{oblate}(\mathbf{r})/(j\omega\rho U_b L \sinh \xi_o)$ for the oblate hemispheroid, and, $\widehat{P}_{sphere}(\mathbf{r}) = P_{sphere}(\mathbf{r})/(j\omega\rho U_b L)$ for the hemisphere. Therefore, the normalized pressures are

$$\begin{aligned}
\widehat{P}_{flap}(\mathbf{r}) &= \sin \eta, \\
\widehat{P}_{prolate}(\mathbf{r}) &= -\left(\frac{Q_1^1(\cosh \xi_o)}{C_1^1(\xi_o)}\right) \sin \eta \cos q, \\
\widehat{P}_{oblate}(\mathbf{r}) &= -\left(\frac{Q_1^1(j \sinh \xi_o)}{D_1^1(\xi_o)}\right) \sin \eta \cos q, \\
\widehat{P}_{sphere}(\mathbf{r}) &= \frac{1}{2} \sin \eta \cos q.
\end{aligned} \tag{3.11}$$

For all these geometries, the normalized pressure is proportional to $\sin \eta$. Thus, the pressure is zero at the tip of the flap and hemispheroids ($\eta = 0$), because displacement of the tip displaces no fluid. The pressure is maximal at the base ($\eta = \pi/2$), because maximal fluid is displaced there. For the hemispheroids, normalized pressure is also proportional to $\cos q$ because the normal component of the surface velocity is proportional to $\cos q$. Thus, a displacement in the positive x-direction applies a compressive force to fluid for $|q| < \pi/2$ and a tensile force on the fluid for $\pi/2 < |q| < \pi$. In addition, the magnitude of the pressure must be zero at $q = \pi/2$ where the velocity of the hemispheroid is tangential to the fluid, and maximal at $q = 0$ where the velocity is normal to the fluid.

The dependence of the normalized pressure on η for different shapes of hemispheroids, some of which are illustrated in Figure 3-3, and for the flap and hemisphere is shown in Figure 3-2. In this comparison, all the structures have the same height. All these structures show a sinusoidal increase in normalized pressure from the tip of the structure ($\eta = 0$) to its base along the plate ($\eta = \pi/2$). As the $\xi_o \rightarrow \infty$, both the prolate and oblate hemispheroids approach hemispheres and the normalized pressure approaches that of a hemisphere. For prolate hemispheroids, as $\xi_o \rightarrow 0$ the hemispheroid becomes infinitesimally narrow and the pressure produced on its surface becomes infinitesimal. For oblate hemispheroids, as $\xi_o \rightarrow 0$ the hemispheroid infinitely wide and the results approach most closely those of the flap. The flap has the largest pressure because it displaces the most fluid when it is translated. It exceeds the pressure even on an infinitely wide oblate hemispheroid, because translation of the flap is normal to its surface whereas that for the oblate hemispheroid is not.

The effect of shape is examined more directly in Figure 3-4 which shows the normalized pressure at the base of the hemispheroid as a function of its shape. As shown in Figure 3-3, for small values of ξ_o, the prolate hemispheroid is more pencil-shaped and the pressure is small because the cross-sectional area of the prolate hemispheroid is small and little fluid is displaced by its motion. If we restrict ourselves to exclude narrow hemispheroids ($\xi_o < .2$), which displace little fluid, the pressures for hemispheroids of fixed height whose shapes range from infinitely wide oblate hemispheroids down to narrow prolate hemispheroids differ by less than a factor of 4. The change in pressure with ξ_o for hemispheroids of fixed height is greatest for thin prolate hemispheroids. For prolate hemispheroids, if ξ_o is increased from .2 to .6, then the pressure is increased by a factor of two.

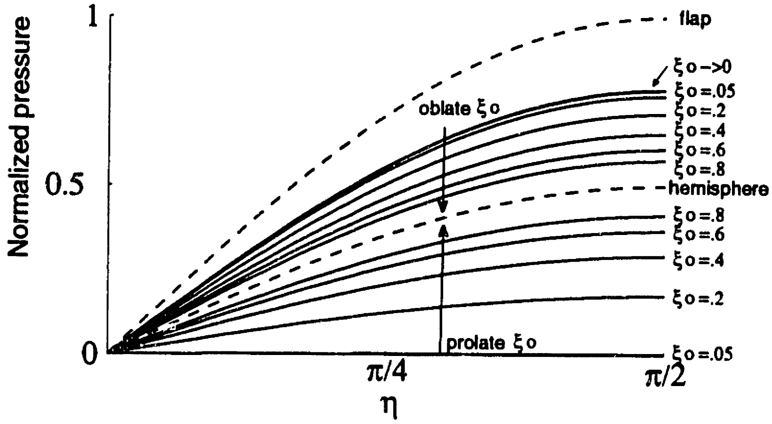

Figure 3-2: The normalized pressure on the flap, hemisphere, prolate hemispheroids, and oblate hemispheroids resulting from translational motion of the plate plotted versus η for different geometry shapes. All structures have the same height. Results for the hemispheroids are given for different values of the parameter ξ_o. The arrows point in the direction of increasing ξ_o.

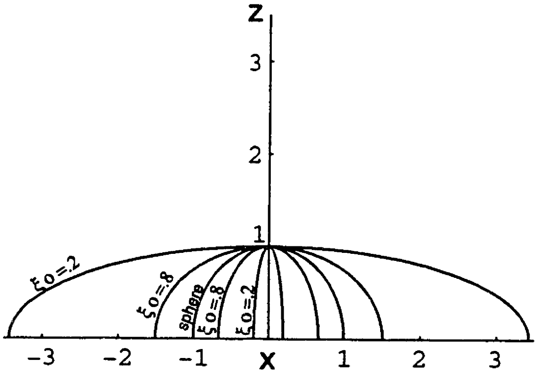

Figure 3-3: A cross-section of prolate and oblate hemispheroids of fixed height.

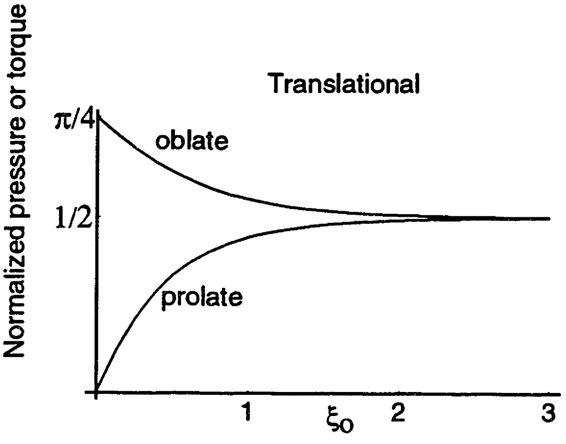

Figure 3-4: The normalized pressure as a function of ξ_o for $\eta = \pi/2$ for prolate and oblate hemispheroids as well as the normalized torque for translational motion, $T_t/(j\omega\rho U_b L^2 hw\pi/4)$.

Rotational motion

The pressure on the hemispheroid surface due to rotation of the hemispheroid can be obtained from Equations 3.2, 3.9, and 3.10, and the pressure on the flap is given elsewhere (Freeman and Weiss, 1990a). It will soon be shown that it is the focal length, L, and not the height, that mainly determines the pressure; therefore, we shall compare the pressure of structures with the same focal length.

For rotational motion, we define the normalized pressures as $P_{flap}(\mathbf{r})/(-\omega^2\rho\Theta L^2)$ for the flap, $P_{prolate}(\mathbf{r})/(-\omega^2\rho\Theta L^2)$ for the prolate hemispheroid, $P_{oblate}(\mathbf{r})/(-\omega^2\rho\Theta L^2)$ for the oblate hemispheroid. The normalized pressures are

$$\begin{aligned}
\widehat{P}_{flap}(\mathbf{r}) &= \sum_{l=0}^{\infty} J_l \sin(2l+1)\eta, \\
\widehat{P}_{prolate}(\mathbf{r}) &= \sum_{l=0}^{\infty} \frac{I_l}{C^1_{2l+1}(\xi_o)\cosh^2\xi_o} P^1_{2l+1}(\cos\eta) Q^1_{2l+1}(\cosh\xi), \\
\widehat{P}_{oblate}(\mathbf{r}) &= \sum_{l=0}^{\infty} \frac{I_l}{D^1_{2l+1}(\xi_o)\sinh^2\xi_o} P^1_{2l+1}(\cos\eta) Q^1_{2l+1}(j\sinh\xi), \\
\widehat{P}_{sphere}(\mathbf{r}) &= 0,
\end{aligned} \tag{3.12}$$

where $I_l = 4(-1)^{(2l+1)}/((2l+1)((2l+1)^2-4))$.

Figure 3-5 and Figure 3-7 illustrate the normalized pressure on the surface for hemispheroids with the same focal length. These hemispheroids are shown in Figure 3-6. We see that, except for prolate hemispheroids with very small cross-sectional area, the normalized pressure varies by less than a factor of four for fixed L so that it is the focal length that, to first order, determines the pressure for rotational motion.

For both prolate and oblate shapes, for fixed L, the size of the hemispheroids increases with increasing ξ_o, approaching infinity as $\xi_o \to \infty$ and the shape becomes hemispherical.

The reason why L determines the pressure in rotational motion is because, except for very thin prolate hemispheroids, the more eccentric the hemispheroid (or the lower ξ_o), the more fluid is displaced by its rotational motion so that small prolate hemispheroids and small oblate hemispheroids displace as much fluid as large, nearly

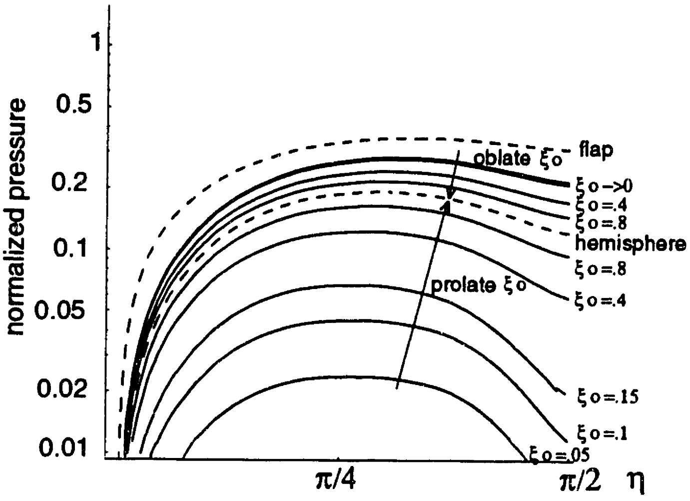

Figure 3-5: Plotted versus η are the normalized pressure for rotational motion on flap, prolate, and oblate hemispheroids. All structures have the same focal length L.

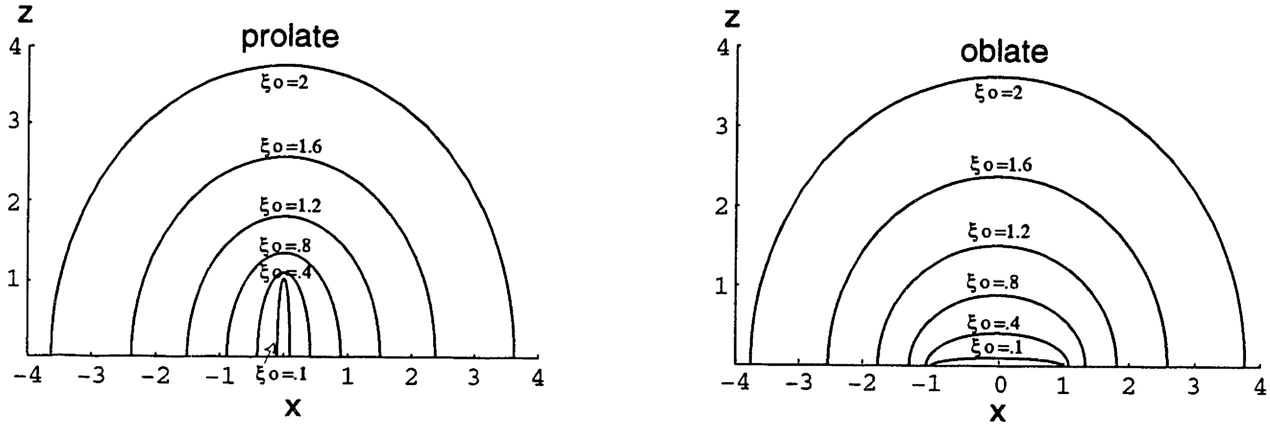

Figure 3-6: A cross-section of prolate and oblate hemispheroids of fixed L.

hemispherical hemispheroids. For a hemisphere, since its normal, $\hat{\mathbf{n}} = \hat{\mathbf{r}}$ is everywhere perpendicular to its direction of motion, $\hat{\theta}$, no fluid is displaced, and for a finite hemisphere, the fluid pressure everywhere is zero (Figure 3-5 and Figure 3-7 illustrate the pressure for an infinite hemisphere). As $\xi_o \rightarrow 0$, for both prolate and oblate shapes, $\hat{\mathbf{n}} \rightarrow \hat{\theta}$. For very thin prolate hemispheroids, however, the cross-sectional area approaches zero as $\xi_o \rightarrow 0$ and the amount of fluid displaced approaches zero.

For fixed L and ξ_o, the pressure first increases and then decreases with η (Figure 3-5), in contrast to the pressure for translational motion which monotonically increases with η (Figure 3-2). The increase in pressure with increasing η results from the

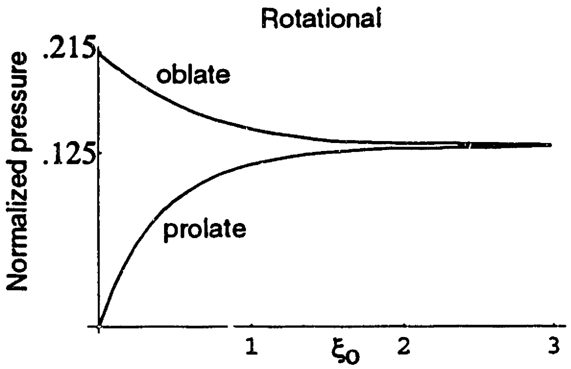

Figure 3-7: The normalized pressure for rotational motion on the prolate and oblate hemispheroids as a function of ξ_o at $\eta = \pi/2$ for constant L.

increase in the width with η, and the decrease in pressure with further increase in η results from the decrease in the normal component of surface velocity of the hemispheroid with η (Equation 3.8) which negates the effects of the increasing cross-sectional area.

Hydrodynamic pressure far from surface

We can derive the behaviour of the hydrodynamic pressure far from the surface in the following manner: From Equations 2.22 and 2.23, we see that as $\xi \longrightarrow \infty$, r (which equals $\sqrt{x^2+y^2+z^2}$) approaches $Le^{\xi}/2$. Therefore, let $\xi = \log 2r/L$ in the expressions for $\Phi(\mathbf{r})$, Equation 3.6, Equation 3.7, Equation 3.9, and Equation 3.10. For each expression, we find that $\Phi(\mathbf{r})$ is proportional to $1/r^2$, so that independent of shape, the pressure, which is proportional to $\Phi(\mathbf{r})$, decays as $1/r^2$.

3.3.2 Fluid velocity

In this section we examine the fluid velocity induced by the motion of the hemispheroid. The fluid velocity, $\mathbf{U}(\xi,\eta,q)$, is the gradient of the fluid potential, $\Phi(\xi,\eta,q)$ (Equation 3.1) and for either prolate or oblate hemispheroids for either translational or rotational motion can be expressed as a simple function of q,

$$\begin{aligned} U_\xi(\xi,\eta,q) &= f_1(\xi,\eta)\cos q \\ U_\eta(\xi,\eta,q) &= g_1(\xi,\eta)\cos q, \\ U_q(\xi,\eta,q) &= h_1(\xi,\eta)\sin q, \end{aligned} \tag{3.13}$$

$U_\xi(\xi,\eta,q)$ represents the velocity in a direction perpendicular to a contour of constant ξ. Hence, this velocity is perpendicular to the hemispheroid on its surface. Similarly $U_\eta(\xi,\eta,q)$ and $U_q(\xi,\eta,q)$, represent velocities that are perpendicular to contours of constant η and constant q respectively. On the surface of the hemispheroid, $U_\eta(\xi,\eta,q)$ and $U_q(\xi,\eta,q)$ are tangential to the surface, with $U_\eta(\xi,\eta,q)$ representing flow over the hemispheroid, and $U_q(\xi,\eta,q)$ representing flow around the hemispheroid. The q dependence of the velocity components can be understood in the following way. In the x-z plane, where $q = 0$ or $q = \pi$, $U_q(\xi,\eta,q) = 0$ — there is no preferred $\hat{\mathbf{q}}$ direction in the x-z plane due to the reflection symmetry of the problem about this plane. In the y-z plane where $q = \pi/2$ or $q = 3\pi/2$, $U_\xi(\xi,\eta,q) = 0$ and $U_\eta(\xi,\eta,q) = 0$ because $U_\xi(\xi,\eta,q)$ and $U_\eta(\xi,\eta,q)$ are antisymmetric about this plane due to the antisymmetry of the velocity of the surface of the hemispheroid. Therefore if fluid at a point x, y, z is flowing away from (positive $\hat{\xi}$ direction) and over (negative $\hat{\eta}$ direction) the hemispheroid, fluid at the corresponding point $-x, y, z$ is flowing towards the hemispheroid in the positive $\hat{\eta}$ direction.

Translational motion

The fluid velocity for a prolate hemispheroid translating sinusoidally is

$$U_\xi(\xi,\eta,q) = \frac{U_b \cosh\xi_o \sin\eta \cos q}{C_1^1(\xi_o)\sqrt{\sinh^2\xi + \sin^2\eta}} C_1^1(\xi), \tag{3.14}$$

$$U_\eta(\xi,\eta,q) = \frac{U_b \cosh\xi_o \cos\eta \cos q}{C_1^1(\xi_o)\sqrt{\sinh^2\xi + \sin^2\eta}} Q_1^1(\cosh\xi), \tag{3.15}$$

$$U_q(\xi,\eta,q) = \frac{-U_b \cosh\xi_o \sin q}{C_1^1(\xi_o)\sinh\xi} Q_1^1(\cosh\xi). \tag{3.16}$$

Figure 3-8 illustrates the velocity fields for translational motion for a thin prolate hemispheroid ($\xi_o = .1$). The $\cos q$ dependence of $U_\xi(\xi,\eta,q)$ and $U_\eta(\xi,\eta,q)$, and the $\sin q$ dependence of $U_q(\xi,\eta,q)$ are evident when comparing the upper right panel (the velocity field in the x-z plane ($q = 0$ or $q = \pi$)), and the lower right panel (the velocity field in the $x = -y$ plane ($q = 3\pi/4$ or $q = 7\pi/4$)). In the upper right panel, the velocity has only $U_\xi(\xi,\eta,q)$ and $U_\eta(\xi,\eta,q)$ components— fluid flows out from (in the

$\hat{\xi}$ direction) and over (in the $\hat{\eta}$ direction) the hemispheroid. In the lower right panel, there is a finite $U_q(\xi,\eta,q)$ component and the $U_\xi(\xi,\eta,q)$ and $U_\eta(\xi,\eta,q)$ components are smaller.

The upper left panel indicates the magnitude of the velocity in the x-z plane close to the hemispheroid, with the lengths of the arrows proportional to the magnitudes of the velocities. At the plate (lower left panels) $U_\eta(\xi,\eta,q) = 0$. Since the plate is moving only in the $\hat{\mathbf{x}}$, direction, its normal component of velocity, which is the only component that influences the fluid, is zero.

Figure 3-9 illustrates the translational component of the velocity field in the x-z plane for points close to the surface of an almost hemispherical hemispheroid. A comparison of Figure 3-9 to the upper left panel of Figure 3-8 illustrates some of the effects of the shape on fluid velocity. For the thin, prolate hemispheroid, the fluid velocity, in the x-z plane, close to the surface, is almost all in the normal or $\hat{\xi}$ direction which is approximately $\hat{\mathbf{x}}$, the direction of motion of the hemispheroid. For the almost hemispherical hemispheroid in the x-z plane, there is more η component because there is more slip. There is also less q component and this makes sense—wider hemispheroids should have more fluid flowing over ($\hat{\eta}$ direction) than around ($\hat{\mathbf{q}}$ direction) compared to thinner hemispheroids. To understand the effect of shape on the direction of fluid flow, we study the ratios of the velocity components,

$$\frac{U_\eta(\xi,\eta,q)}{U_q(\xi,\eta,q)} = \frac{-\cos\eta\cot q\sinh\xi}{\sqrt{\sinh^2\xi+\sin^2\eta}}, \tag{3.17}$$

$$\frac{U_\xi(\xi,\eta,q)}{U_\eta(\xi,\eta,q)} = \frac{C_1^1(\xi)\tan\eta}{Q_1^1(\cosh\xi)},$$

for a prolate spheroid, and

$$\frac{U_\eta(\xi,\eta,q)}{U_q(\xi,\eta,q)} = \frac{-\cos\eta\cot q\cosh\xi}{\sqrt{\sinh^2\xi+\sin^2\eta}},$$

$$\frac{U_\xi(\xi,\eta,q)}{U_\eta(\xi,\eta,q)} = \frac{D_1^1(\xi)\tan\eta}{Q_1^1(j\sinh\xi)}, \tag{3.18}$$

for an oblate hemispheroid. We can derive the behavior of $U_\xi(\xi,\eta,q)/U_q(\xi,\eta,q)$ from the behavior of the other ratios. At first glance it would seem that shape doesn't effect the ratios since all the factors that depend on ξ_o have cancelled. However, the value of ξ on the surface equals ξ_o so that for points close to the surface the ratios depend on ξ_o and for points far from the surface, the effects of shape become small. Therefore, to understand the effects of shape, let us set $\xi = \xi_o$ and look at points in the fluid next to the surface of the hemispheroid. Also, since the q dependence of the velocities is independent of shape, let us set $q = \pi/4$, so that $\cot q = 1$ and see how the ratios vary with shape. As $\xi_o \to 0$, Equation 3.17-Equation 3.18, become

$$\frac{U_\eta(\xi = \xi_o, \eta, q = \pi/4)}{U_q(\xi = \xi_o, \eta, q = \pi/4)} = -\xi_o \cot\eta,$$

$$\frac{U_\xi(\xi = \xi_o, \eta, q)}{U_\eta(\xi = \xi_o, \eta, q)} = \frac{-\tan\eta}{\xi_o},$$

for a very thin prolate hemispheroid, and,

$$\frac{U_\eta(\xi = \xi_o, \eta, q = \pi/4)}{U_q(\xi = \xi_o, \eta, q = \pi/4)} = -\cot\eta,$$

$$\frac{U_\xi(\xi = \xi_o, \eta, q)}{U_\eta(\xi = \xi_o, \eta, q)} = \frac{-4\tan\eta}{\pi},$$

for a flat, wide, oblate hemispheroid. As $\xi_o \to \infty$, the ratios become for both oblate and prolate hemispheroids,

$$\frac{U_\eta(\xi = \xi_o, \eta, q = \pi/4)}{U_q(\xi = \xi_o, \eta, q = \pi/4)} = -\cos\eta,$$

$$\frac{U_\xi(\xi = \xi_o, \eta, q)}{U_\eta(\xi = \xi_o, \eta, q)} = -2\tan\eta.$$

For all the shapes, we see that $|U_\eta(\xi,\eta,q)/U_q(\xi,\eta,q)|$ decreases with η. At $\eta = 0$, the most fluid flows in the $\hat{\eta}$ direction, over the hemispheroid. At $\eta = \pi/2$, no fluid flows in the $\hat{\eta}$ direction—all the fluid flows in $\hat{\xi}$ and $\hat{\mathrm{q}}$, which is out from and around the hemispheroid.

We also observe that $|U_\xi(\xi,\eta,q)/U_\eta(\xi,\eta,q)|$ increases with η for all shapes. This follows from the increase in $\hat{\xi} \cdot \hat{\mathbf{x}}$, as η increases from zero to $\pi/2$ which increases $|U_\xi(\xi,\eta,q)|$. The decrease in $|U_\eta(\xi,\eta,q)|$ with η also causes the magnitude of this ratio to increase.

We find that $|U_\eta(\xi,\eta,q)/U_q(\xi,\eta,q)|$ is smallest and $|U_\xi(\xi,\eta,q)/U_\eta(\xi,\eta,q)|$ largest for the thin, prolate hemispheroids. $|U_\eta(\xi,\eta,q)/U_q(\xi,\eta,q)|$ is smallest because fluid can easily flow around the thin hemispheroid in the $\hat{\mathbf{q}}$ direction. $|U_\xi(\xi,\eta,q)/U_\eta(\xi,\eta,q)|$ is largest because for most of its surface, $\hat{\xi} \cdot \hat{\mathbf{x}}$ is largest for a prolate hemispheroid . As the shape becomes wider $|U_\eta(\xi,\eta,q)/U_q(\xi,\eta,q)|$ increases, and $|U_\xi(\xi,\eta,q)/U_\eta(\xi,\eta,q)|$ decreases. The wider hemispheroids have more fluid flowing over in $\hat{\eta}$ than the thinner hemispheroids. For wider hemispheroids, $\hat{\xi} \cdot \hat{\mathbf{x}}$ is less.

For a 2-D flap, the ratios can be expressed as

$$\frac{U_\eta(\xi,\eta,q)}{U_q(\xi,\eta,q)} = \infty,$$

$$\frac{U_\xi(\xi,\eta,q)}{U_\eta(\xi,\eta,q)} = -\tan\eta.$$

Fluid can not go around the 2-D flap so that $|U_\eta(\xi,\eta,q)/U_q(\xi,\eta,q)| = \infty$ for all points in the fluid. $|U_\xi(\xi,\eta,q)/U_\eta(\xi,\eta,q)|$ has values for all η that are closest to $|U_\xi(\xi,\eta,q)/U_\eta(\xi,\eta,q)|$ for a wide oblate hemispheroid. Recall that the pressure along the flap most resembled that of a wide oblate hemispheroid.

Figure 3-10 illustrates the ratios as a function of ξ_o with $\eta = \pi/3$ and $q = \pi/4$.

Magnitude of fluid velocity

We have shown that, to first order, the height of the hemispheroid determines the pressure due to translational motion. However, the velocity in the fluid due to translational motion, is, to first order, determined by the volume of the hemispheroid. Figure 3-11 illustrates the magnitude of fluid velocity, $|U(\xi,\eta = \pi/3, q = 0)|$ as a function of r, the radial distance for fixed volume. Hemispheroids with the same volume are illustrated in Figure 3-12. Except for points close to the surface of thin

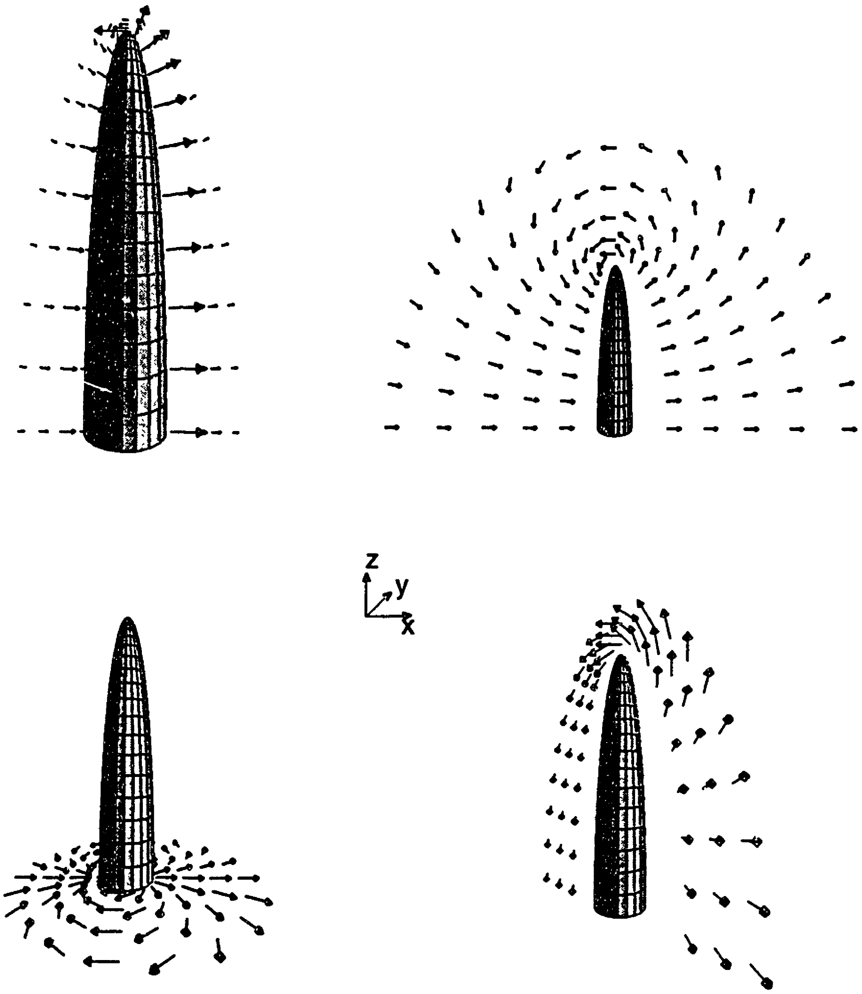

Figure 3-8: The velocity field for a thin prolate hemispheroid ($\xi_o = .1$) for translational motion. The upper panels illustrate the velocity field in the x-z plane. The tail of each vector is placed at the point in the fluid. The magnitude decreases sharply with distance. The upper left panel shows the velocity field for points close to the hemispheroid with the lengths of the arrows proportional to the magnitude of the velocity. The upper right panel shows the velocity field over the same plane. The lengths of the vectors are scaled to a constant magnitude in this right panel and in the lower panels. Apparant differences in the lengths are due to perspective. The lower panels show the vector field along the plate (left) and in the plane, $q = 3\pi/4, 7\pi/4$ (right).

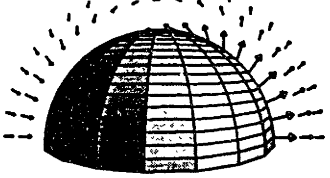

Figure 3-9: The velocity field for a hemispherical prolate hemispheroid ($\xi_o = 5$) for points close to the surface with the lengths of the arrows proportional to the magnitude of the velocity. The tail of each vector is placed at the point in the fluid.

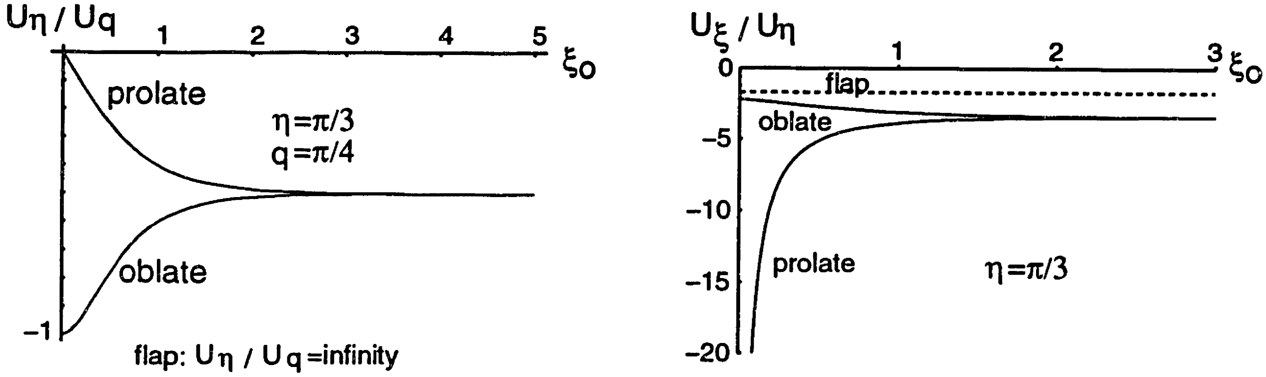

Figure 3-10: Left: $U_\eta(\xi,\eta,q)/U_q(\xi,\eta,q)$ for $\eta = \pi/3$ and $q = \pi/4$ for translational motion. Right: $U_\xi(\xi,\eta,q)/U_\eta(\xi,\eta,q)$ for $\eta = \pi/3$ and all q for translational motion. The results are also shown for a 2-D flap.

prolate hemispheroids ($\xi_o < .3$), the variation in $|U(\mathbf{r})|$ with ξ_o is less than a factor of two. On the surface, the thin prolate hemispheroid has the largest velocity, since its normal is almost parallel to the direction of motion. For the full range of shapes, for large r, $|U(\mathbf{r})|$ decays as $1/r^3$. For large ξ we can approximate $\xi \approx \log 2r/L$ and $\eta = \theta$ in Equations 3.14-3.16, and express $|U(\mathbf{r})|$ as

$$|U(\mathbf{r})|_{prolate} = \left|\frac{2L^3\cosh\xi_o}{3C_1^1(\xi_o)}\frac{U_b}{r^3}\sqrt{1+3\sin^2\theta-3\sin^2\theta\sin^2 q}\right|, \tag{3.19}$$

$$|U(\mathbf{r})|_{oblate} = \left|\frac{2L^3\sinh\xi_o}{3D_1^1(\xi_o)}\frac{U_b}{r^3}\sqrt{1+3\sin^2\theta-3\sin^2\theta\sin^2 q}\right|, \tag{3.20}$$

We consider the magnitude to be the product of two terms— a velocity shape factor that depends only on ξ_o, and a factor that contains the r, θ and q dependences. For hemispheroids with the same volume, the velocity shape factors for translational motion,

$$|vsf|_{prolate} = \left|\frac{2}{3\sinh^2\xi_o C_1^1(\xi_o)}\right|, \tag{3.21}$$

$$|vsf|_{oblate} = \left|\frac{2}{3\cosh^2\xi_o D_1^1(\xi_o)}\right|,$$

$$|vsf|_{sphere} = \frac{1}{2},$$

(3.22)

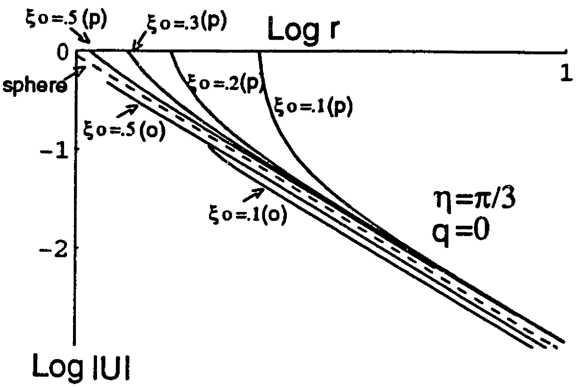

Figure 3-11: The magnitude of fluid velocity for translational motion for prolate and oblate hemispheroids of the same volume as a function of r with $\eta = \pi/3$ and $q = 0$.

are illustrated in Figure 3-13. As was indicated in Figure 3-11, for the same volume, the variation in magnitude, for large r, is at most a factor of two for all shapes, with the thin, tall, prolate hemispheroid having the largest fluid velocity, and the wide, flat, oblate hemispheroid, the smallest. Why is the volume mainly determined by $|U(\mathbf{r})|$ and not the height, which was important for pressure? Consider an infinitely wide oblate hemispheroid, with fixed height, h. The pressure for this shape is, except for very thin prolate hemispheroids, comparable to the pressure of all hemispheroids of height h (Figure 3-2). However because its width extends infinitely into the fluid, the fluid velocity due to its motion at a particular r in the fluid will be much larger than that of a hemispheroid of height h and finite width. To summarize, the magnitude of the fluid velocity, except for points close to the surface of thin prolate hemispheroids, is mainly determined by the volume of the hemispheroid. For a fixed volume, for points close to the surface, thin prolate hemispheroids have larger magnitudes than other shapes. For points far from the surface, the magnitude for all shapes varies by less than a factor of two and decays as $1/r^3$.

Rotational motion

The fluid velocity for a prolate hemispheroid rotating sinusoidally is

$$U_\xi(\xi,\eta,q) = \frac{-j\omega\Theta L\cos q}{\sqrt{\sinh^2\xi+\sin^2\eta}}\sum_{l=0}^{\infty}\frac{I_l}{C^1_{2l+1}(\xi_o)}P^1_{2l+1}(\cos\eta)\frac{dQ^1_{2l+1}(\cosh\xi)}{d\xi},$$

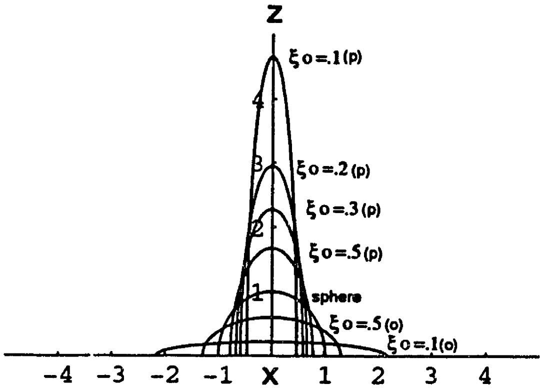

Figure 3-12: A cross-section of prolate and oblate hemispheroids of fixed volume.

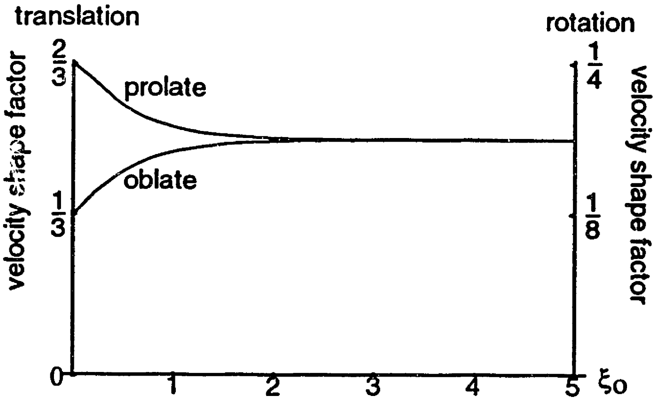

Figure 3-13: The velocity shape factors for hemispheroids with fixed volume.

$$U_\eta(\xi,\eta,q) = \frac{-j\omega\Theta L\cos q}{\sqrt{\sinh^2\xi+\sin^2\eta}}\sum_{l=0}^{\infty}\frac{I_l}{C^1_{2l+1}(\xi_o)}\frac{dP^1_{2l+1}(\cos\eta)}{d\eta}Q^1_{2l+1}(\cosh\xi), \tag{3.23}$$

$$U_q(\xi,\eta,q) = \frac{j\omega\Theta L\sin q}{\sin\eta\sinh\xi}\sum_{l=0}^{\infty}\frac{I_l}{C^1_{2l+1}(\xi_o)}P^1_{2l+1}(\cos\eta)Q^1_{2l+1}(\cosh\xi), \tag{3.24}$$

and similar expressions can be derived for the oblate case. The velocity field is shown in Figure 3-14. Unlike translational motion, the fluid closer to the base of the hemispheroid is directed downward ($U_\eta(\xi,\eta,q) > 0$ for $q = 0$ and upward for $q = \pi$ (upper panels). This feature is also evident for the 2-D flap (Freeman, 1990).

The ratios, $|U_\eta(\xi,\eta,q)/U_q(\xi,\eta,q)|$, and $|U_\xi(\xi,\eta,q)/U_\eta(\xi,\eta,q)|$ were studied and are plotted for $\eta = \pi/3$ and $q = \pi/4$ in Figure 3-15. Because the solution for rotational motion is an infinite series, simple asymptotic expressions for the ratios as $\xi_o \rightarrow 0$ for prolate and oblate hemispheroids could not be obtained. However, from studies of the ratios for the full range of ξ_o, η and q, we observe the same trends as for translational motion — for thin, prolate hemispheroids, the fluid flows mainly around the hemispheroid, and as the hemispheroid becomes wider, more fluid flows over the hemispheroid.

Magnitude of fluid velocity

In translational motion, the magnitude of the fluid velocity is mainly determined by the volume of the hemispheroid. For rotational motion, the quantity that, to first order, determines $|U(\mathbf{r})|$ is Lw, the focal length time the width, which is $L^2\sinh\xi_o$ for prolate hemispheroids and $L^2\cosh\xi_o$ for oblate hemispheroids. Figure 3-16 illustrates the magnitude of fluid velocity, $|U(\xi,\eta=\pi/3,q=0)|$ as a function of r, the radial distance, for hemispheroids with the same Lw. Hemispheroids with the same Lw are illustrated in Figure 3-17, and Figure 3-18. The curves look strikingly similar to those of Figure 3-11. For large r, the magnitudes of the velocities for the full range of hemispheroidal shapes are nearly the same, and decay as $1/r^3$.

Why is the magnitude of the velocity mainly determined by Lw? The focal length is important in determining the fluid velocity for the reasons stated in Section 3.3.1, the amount of normal component of the surface velocity for rotational motion is, to first order, determined by focal length and the relevence of width for determining $|U(\mathbf{r})|$ was discussed in Section 3.3.2.

As was done for translational motion, we let $\xi \rightarrow \infty$, and express the magnitudes of the velocities as

$$\begin{aligned} |U(\mathbf{r})|_{prolate} &= \left|\frac{L^4}{4C_1^1(\xi_o)}\frac{\omega\Theta}{r^3}\sqrt{1+3\sin^2\theta-3\sin^2\theta\sin^2 q}\right|, \\ |U(\mathbf{r})|_{oblate} &= \left|\frac{L^4}{4D_1^1(\xi_o)}\frac{\omega\Theta}{r^3}\sqrt{1+3\sin^2\theta-3\sin^2\theta\sin^2 q}\right|. \end{aligned}$$

The expressions are similar to Equations 3.19-3.20 except the velocity shape factors are different,

$$\begin{aligned} |vsf|_{prolate} &= \left|\frac{L^4}{4C_1^1(\xi_o)}\right|, \\ |vsf|_{oblate} &= \left|\frac{L^4}{4D_1^1(\xi_o)}\right|. \end{aligned} \qquad (3.25)$$

For fixed Lw ($L = 1/\sqrt{\sinh\xi_o}$ for prolate hemispheroids and $L = 1/\sqrt{\cosh\xi_o}$ for oblate hemispheroids), the velocity shape factors are the same (scale by 8/3) as those of translational motion (Equations 3.21) for fixed volume.

3.3.3 The Hydrodynamic Torque induced by the hemispheroid

The hydrodynamic torque induced by the hemispheroid is described in prolate spheroidal coordinates by

$$T = \int_0^{2\pi}\int_0^{\pi/2} P\cdot(\mathbf{r}(\xi_o,\eta)\times\hat{\xi})L^2\sinh\xi_o\sin\eta\sqrt{\sinh^2\xi_o+\sin^2\eta}\,d\eta\,dq,$$

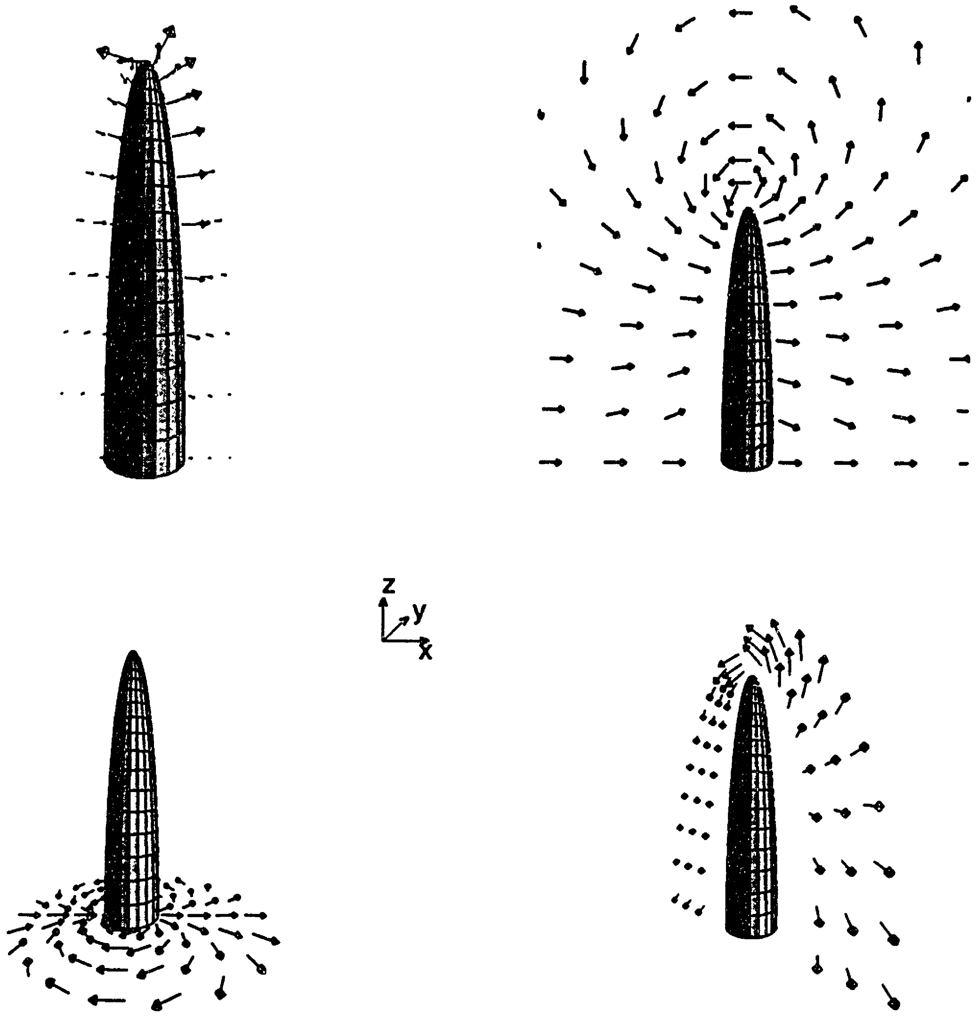

Figure 3-14: Same as Figure 3-8 for rotational motion.

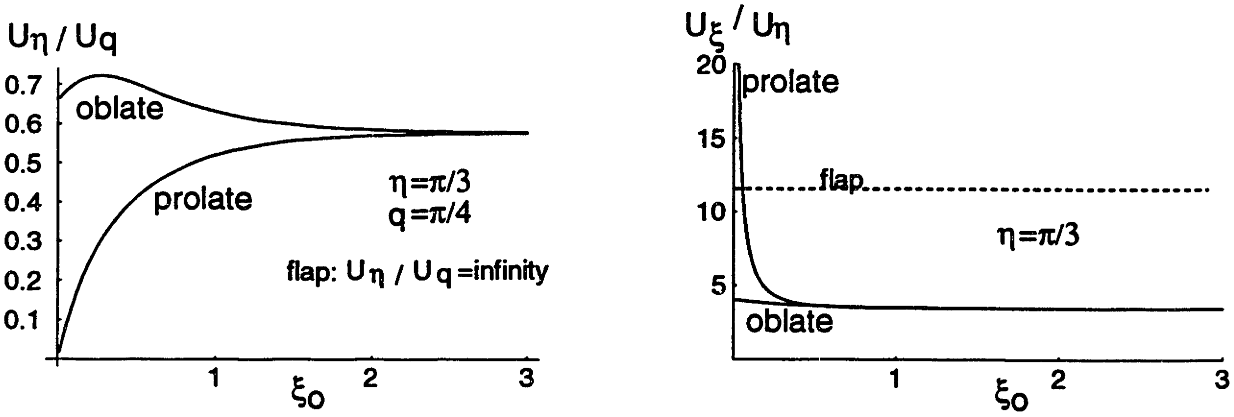

Figure 3-15: Left: $U_\eta(\xi,\eta,q)/U_q(\xi,\eta,q)$ for $\eta = \pi/3$ and $q = \pi/4$ for rotational motion. Right: $U_\xi(\xi,\eta,q)/U_\eta(\xi,\eta,q)$ for $\eta = \pi/3$ and all q for rotational motion. The results are also shown for a 2-D flap.

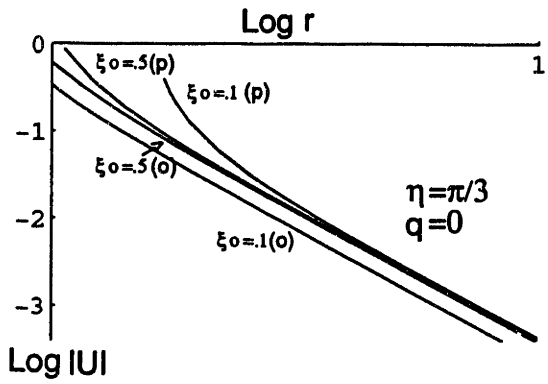

Figure 3-16: The magnitude of fluid velocity for rotational motion for prolate and oblate hemispheroids with Lw.

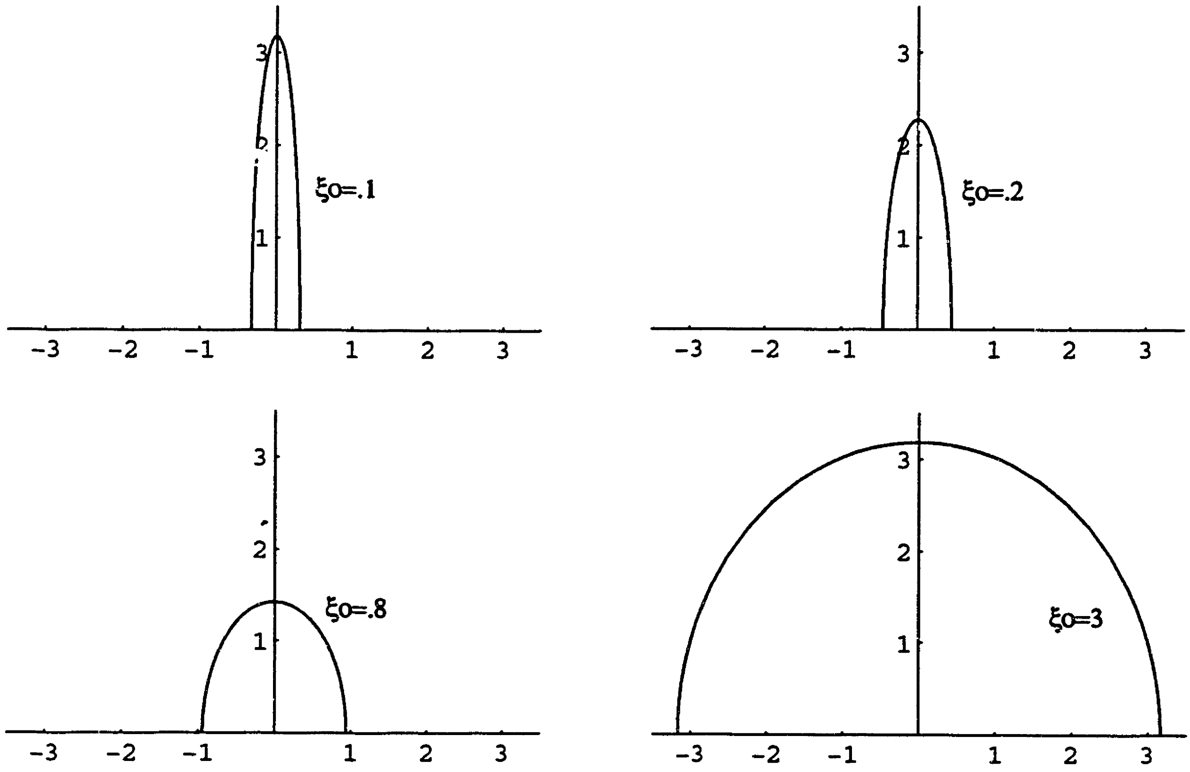

Figure 3-17: A cross-section of prolate hemispheroids with fixed $Lw = L^2 \sinh \xi_o$.

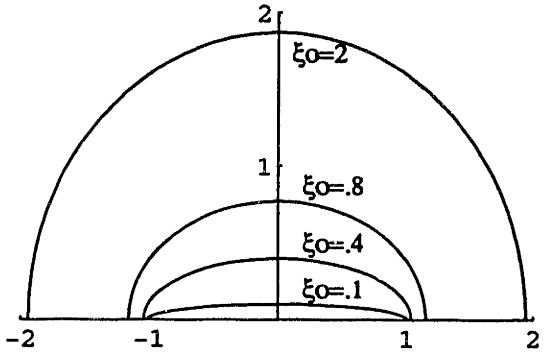

Figure 3-18: A cross-section of oblate hemispheroids of fixed $Lw = L^2 \cosh \xi_o$.

where **r** is the radial vector, and $L^2 \sinh \xi_o \sin \eta \sqrt{\sinh^2 \xi_o + \sin^2 \eta}\, d\eta dq$ describes an area element in prolate spheroidal coordinates. Because the fluid is modelled as inviscid there is no shearing force contributing to the torque.

Translational motion

The hydrodynamic torque for a prolate hemispheroid in translational motion is found by substituting Equation 3.2 and Equation 3.6 into Equation 3.3,

$$T_t = \frac{j\omega\rho L^4 U_b \cosh \xi_o \sinh \xi_o \pi Q_1^1(\cosh \xi_o)}{4C_1^1(\xi_o)}. \tag{3.26}$$

Equation 3.3 and Equation 3.26 are derived in this chapter's appendix. The hydrodynamic torque for an oblate hemispheroid in translational motion can be expressed as

$$T_t = \frac{j\omega\rho L^4 U_b \cosh \xi_o \sinh \xi_o \pi Q_1^1(j \sinh \xi_o)}{4D_1^1(\xi_o)}. \tag{3.27}$$

We see that the torque varies linearly with $L^4 \cosh \xi_o \sinh \xi_o$ or $L^2 hw$, the product of the focal length squared and the cross-sectional area. The focal length is an important factor in determining the hydrodynamic torque for the same reason that it was important in determining the hydrodynamic pressure for rotational motion— for rotational motion, fluid is only displaced by the normal component of the $\hat{\theta}$ component of surface velocity. For a hemisphere, for which $L = 0$, the normal component of $\hat{\theta}$ equals zero, so that the hydrodynamic torque induced by the hemisphere is zero. The more eccentric the shape, the more torque is obtained because the normal to the

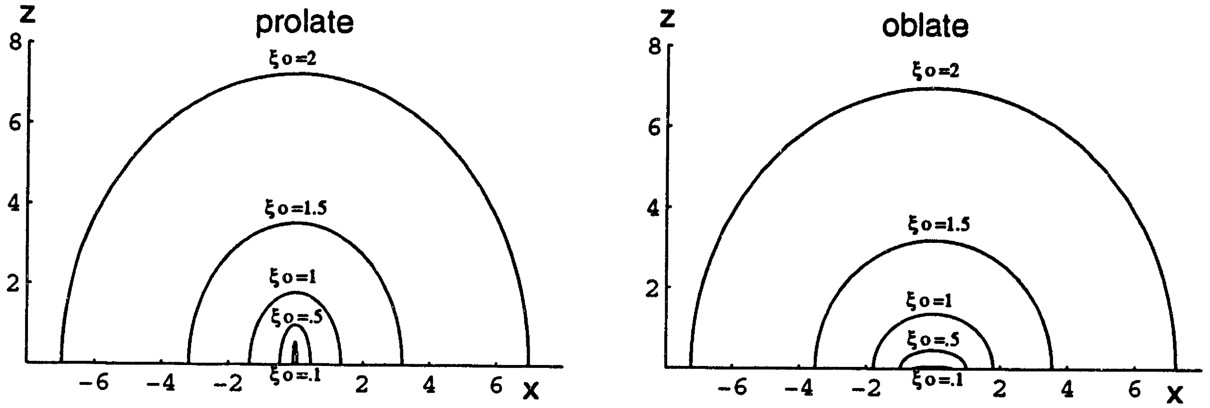

Figure 3-19: Cross-section of hemispheroids with fixed L^2hw.

surface has a larger component in the $\hat{\theta}$ direction. The cross-sectional area is also an important factor in determining the hydrodynamic torque because the larger the cross-sectional area, the more fluid is displaced. Figure 3-4, which illustrates normalized hydrodynamic pressure for hemispheroids for which h is fixed, also illustrates normalized hydrodynamic torque for translational motion for hemispheroids for which L^2hw is fixed (Figure 3-19).

The rotational torque for a prolate hemispheroid is described by

$$T_r = -\rho L^5 \sinh \xi_o \omega^2 \Theta K_2, \tag{3.28}$$

where

$$K_2 = \pi \int_0^{\pi/2} \sum_{l=0}^{\infty} \frac{Q_{2l+1}^1(\cosh \xi_o) I_{2l+1}(4l+3)}{(2l+1)(2l+2)C_{2l+1}(\xi_o)} P_{2l+1}^1(\cos \eta) \sin^2 \eta \cos \eta d\eta,$$

and for the oblate hemispheroid,

$$T_r = -\rho L^5 \cosh \xi_o \omega^2 \Theta K_3, \tag{3.29}$$

with

$$K_3 = \pi \int_0^{\pi/2} \sum_{l=0}^{\infty} \frac{Q_{2l+1}^1(j \sinh \xi_o) I_{2l+1}(4l+3)}{(2l+1)(2l+2)D_{2l+1}(\xi_o)} P_{2l+1}^1(\cos \eta) \sin^2 \eta \cos \eta d\eta.$$

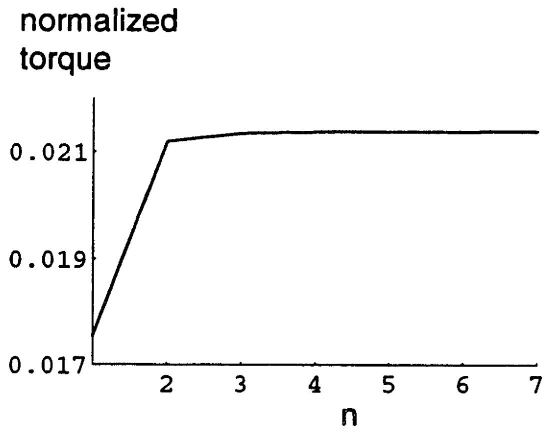

Figure 3-20: The truncated series approximation for the normalized torque, $(T_r)_n/(\rho L^5\omega^2\Theta)$, computed by truncating the series after the first n $(\xi_o = 1)$. The result is within .01% of its correct value for $n = 3$.

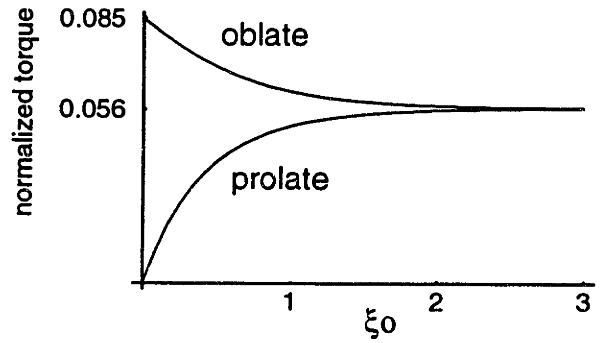

Figure 3-21: The normalized torque for rotational motion, $T_r/(\omega^2\rho\Theta L^4 w\pi)$ for the prolate and oblate hemispheroids.

These integrals may be evaluated term by term.

Figure 3-20 illustrates the truncated series approximation for the normalized torque, $(T_r)_n/(L^5\cosh^5\xi_o\rho\omega^2\Theta)$ as a function of the number of terms, n. The torque computed by the first three terms of the series is within .02% of its correct value.

The hydrodynamic torque for rotational motion varies linearly with L^4w. Here, height is of lesser importance and focal length is more important than in translational motion because height is of lesser importance and focal length is more important in determining the hydrodynamic pressure for rotational motion. Figure 3-21 illustrates the hydrodynamic torque for rotational motion for hemispheroids for which L^4w is fixed (Figure 3-22). These curves scale almost linearly with those of Figure 3-4 as well as those of Figure 3-7.

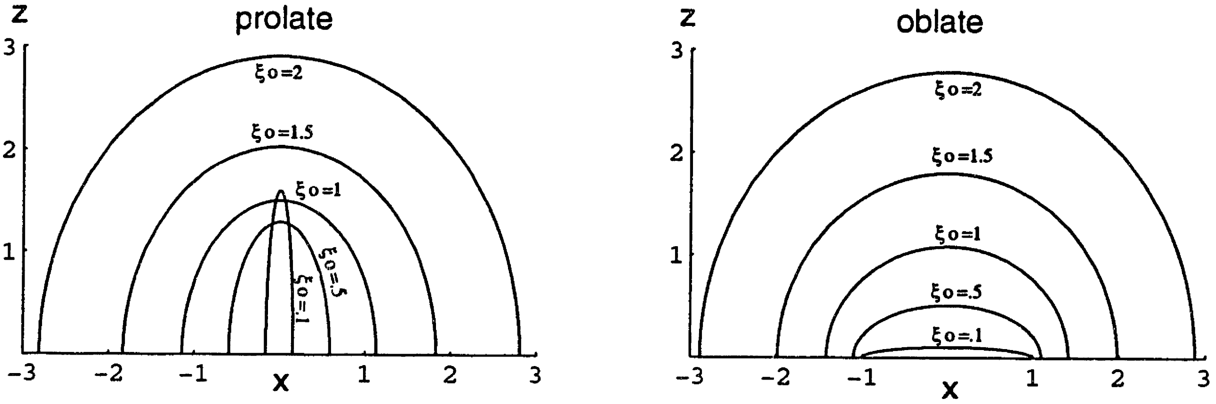

Figure 3-22: Cross-section of hemispheroids with fixed L^4w.

3.4 Conclusion

We have derived analytic solutions in the limit of high frequencies for the hydrodynamics of a hemispheroid hinged to an oscillating plate using spheroidal coordinates, and we have studied the effect of shape of the hemispheroid on the hydrodynamics. Shape has an important effect on the hydrodynamics. We studied the effect of shape by first determining which combination of size parameters such as focal length, height, width, or volume, had a large effect on the hydrodynamics. We then fixed the combination with the largest effect, and studied the hydrodynamics as a function of ξ_o, the shape parameter.

The pressure due to translation of the plate is largely affected by height. For nearly all hemispheroids of the same height, except for extremely thin prolate hemipsheroids with $\xi_o < .2$, the difference in pressure between all the shapes varies by less than a factor four. The change in pressure with ξ_o for hemispheroids of fixed height is greatest for thin prolate hemispheroids. For prolate hemispheroids, if ξ_o is increased from .2 to .6, then the pressure is increased by a factor of two.

The pressure due to rotation about the hinge is largely affected by focal length and is linearly proportional to its square. This implies that the more eccentric the hemispheroid, the larger is the pressure. For fixed focal length, the change in pressure with ξ_o is similar the change in pressure with ξ_o for translational motion for hemispheroids with fixed height.

The hydrodynamic torque is, largely determined by the product of L^2hw for translational motion and L^4w for rotational motion. This means that for translational motion, for hemispheroids of fixed cross-sectional area, the more eccentric the shape, the larger is the hydrodynamic torque. For rotational motion, for hemispheroids of the same width, the more eccentric the shape, the larger is the hydrodynamic torque.

The direction of fluid flow is affected by shape. Fluid tends to flow mainly around thin, prolate hemispheroids. For wider shapes, fluid flows over and around the hemispheroid.

Away from the hemispheroid, the volume of the hemispheroid mainly determines magnitude of the fluid velocity for translational motion. For rotational motion, it is the the product of focal length and width that mainly determines magnitude of the fluid velocity.

3.5 Appendix

Laplace's equation (Equation 2.24) is separable in prolate spheroidal coordinates so that the solution can be expressed as (Moon and Spencer, 1971)

$$\Phi(\mathrm{r}) = \sum_{\rho=0}^{\infty}\sum_{p=0}^{\infty} H_p^\rho(\xi)\Theta_p^\rho(\eta)Z_p^\rho(q),$$

where H, Θ, and Z satisfy the equations

$$\frac{d^2H(\xi)}{d\xi^2} + \coth\xi\frac{dH(\xi)}{d\xi} - \left(p(p+1) + \frac{\rho^2}{\sinh^2\xi}\right)H(\xi) = 0, \tag{3.30}$$

$$\frac{d^2\Theta(\eta)}{d\eta^2} + \cot\eta\frac{d\Theta(\eta)}{d\eta} + \left(p(p+1) - \frac{\rho^2}{\sin^2\eta}\right)\Theta(\eta) = 0, \tag{3.31}$$

$$\frac{d^2Z(q)}{dq^2} + \rho^2 Z(q) = 0. \tag{3.32}$$

The solution to Equation 3.30 is a linear combination of Legendre functions in $\cosh\xi$,

$$H(\xi) = A_p^\rho P_p^\rho(\cosh\xi) + B_p^\rho Q_p^\rho(\cosh\xi),$$

and the solution to Equation 3.31 is a linear combination of Legendre functions in $\cos\eta$,

$$\Theta(\eta) = C_p^\rho P_p^\rho(\cos\eta) + D_p^\rho Q_p^\rho(\cos\eta),$$

where A_p^ρ, B_p^ρ, C_p^ρ, and D_p^ρ are constants determined by boundary conditions. The solution to Equation 3.32 is a linear combination of sinusoidal functions in q,

$$Z(q) = E^\rho \cos\rho q + F^\rho \sin\rho q.$$

Since $\Phi(\mathrm{r})$ is finite at both $\eta = 0$ and $\xi = \infty$, and since $Q_p^\rho(\cos\eta)$ and $P_p^\rho(\cosh\xi)$ are infinite at $\eta = 0$ and $\xi = \infty$ respectively, we set the coefficients of these terms to zero. The general form of the solution is then

$$\Phi(\mathbf{r}) = \sum_{\rho=0}^{\infty}\sum_{p=0}^{\infty}\left(K_p^\rho \sin \rho q + M_p^\rho \cos \rho q\right) Q_p^\rho(\cosh\xi)P_p^\rho(\cos\eta), \tag{3.33}$$

where K_p^ρ and M_p^ρ are constants.

3.5.1 Translational motion

Applying Equation 3.5 we obtain

$$-\sum_{\rho=0}^{\infty}\sum_{p=0}^{\infty} K_p^\rho Q_p^\rho(\cosh\xi)\left.\frac{\partial P_p^\rho(\cos\eta)}{\partial\eta}\right|_{\eta=\pi/2} \sin\rho q + M_p^\rho Q_p^\rho(\cosh\xi)\left.\frac{\partial P_p^\rho(\cos\eta)}{\partial\eta}\right|_{\eta=\pi/2} \cos\rho q = 0.$$

Therefore we find that

$$\left.\frac{\partial P_p^\rho(\cos\eta)}{\partial\eta}\right|_{\eta=\pi/2} = 0.$$

Now

$$\left.\frac{\partial P_p^\rho(\cos\eta)}{\partial\eta}\right|_{\eta=\pi/2} = f(\Gamma)\sin(\frac{\pi}{2}(\rho+p)),$$

(Abramowitz and Stegun, 1964) where $f(\Gamma)$ is a function of Γ functions which has no zero. Therefore $p+\rho$ is an even number. Applying Equation 3.4 we obtain

$$\sum_{\rho=0}^{\infty}\sum_{p=0}^{\infty} K_p^\rho C_p^\rho(\xi_o)P_p^\rho(\cos\eta)\sin\rho q + M_p^\rho C_p^\rho(\xi_o)P_p^\rho(\cos\eta)\cos\rho q$$

$$= LU_b\cosh\xi_o\sin\eta\cos q$$

where

$$C_p^\rho(\xi_o) = \frac{\partial Q_p^\rho(\cosh\xi)}{\partial\xi}, \text{ for } \xi=\xi_o.$$

Therefore we have

$$\rho = 1, \quad K_p^\rho = 0, \quad \sum_{l=0}^{\infty} M_{2l+1}^1 C_{2l+1}^1(\xi_o)P_{2l+1}^1(\cos\eta) = LU_b\cosh\xi_o\sin\eta.$$

Since

$$P_1^1(\cos\eta) = \sin\eta,$$

all the terms are zero except for $l = 0$, so that $M_1^1 C_1^1(\xi_o) = LU_b \cosh\xi_o$. Therefore, the solution for $\Phi(\mathbf{r})$ is

$$\Phi(\mathbf{r}) = \frac{LU_b \cosh\xi_o}{C_1^1(\xi_o)} Q_1^1(\cosh\xi)\sin\eta\cos q.$$

Rotational motion

The boundary condition on the hemispheroid surface that results from hemispheroid rotation with the plate stationary can be written as

$$\nabla\Phi(\mathbf{r})\cdot\hat{\mathbf{n}} = -j\omega\Theta\sqrt{x^2+z^2}\hat{\theta}\cdot\hat{\mathbf{n}}, \text{ for } \xi = \xi_o,$$

which can be expressed as

$$\nabla\Phi(\mathbf{r})\cdot\hat{\xi} = -j\omega\Theta\sqrt{x^2+z^2}(\sqrt{x^2+z^2}\nabla\Theta\cdot\hat{\xi}).$$

Hence, after cancelling metric coefficients we obtain

$$\frac{\partial\Phi(\mathbf{r})}{\partial\xi} = -j\omega\Theta(x^2+z^2)\frac{\partial\Theta(x,y)}{\partial\xi}.$$

We use $\Theta = \tan^{-1}(z/x)$ and the chain rule for evaluation of $\partial\Theta(x,z)/\partial\xi$ to yield the boundary condition

$$\frac{\partial\Phi(\mathbf{r})}{\partial\xi} = L^2 j\omega\Theta\sin\eta\cos\eta\cos q, \text{ for } \xi = \xi_o.$$

The boundary conditions on the plate and at ∞ are the same as for translational motion. We obtain the same general solution as Equation 3.33 and we again have $p+\rho$ is even. However, now we have

$$\sum_{\rho=0}^{\infty}\sum_{p=0}^{\infty} A_p^\rho C_p^\rho(\xi_o)P_p^\rho(\cos\eta)\sin\rho q + B_p^\rho C_p^\rho(\xi_o)P_p^\rho(\cos\eta)\cos\rho q$$

$$= L^2 j\omega\Theta \sin\eta \cos\eta \cos q.$$

We still have

$$\rho = 1 \quad A_p^\rho = 0$$

so that p is odd. Now we have

$$\sum_{k=0}^{\infty} B_{2k+1}^1 C_{2k+1}^1(\xi_o) P_{2k+1}^1(\cos\eta) = L^2 j\omega\Theta \sin\eta \cos\eta. \tag{3.34}$$

We use the orthogonality property of Legendre functions to find the coefficients B_{2k+1}. We multiply Equation 3.34 by $\sin\eta P_{2l+1}^1(\cos\eta)$. With $x = \cos\eta$, $dx = -\sin\eta d\eta$, $\sqrt{1-x^2} = \sin\eta$, we integrate from 1 to 0 to obtain (Morse and Feshbach, 1953)

$$B_{2l+1} C_{2l+1}^1 \frac{(2l+1)(2l+2)}{4l+3} = L^2 j\omega\Theta \int_0^1 x\sqrt{1-x^2} P_{2l+1}^1(x) dx.$$

From (Prudnikov, 1986),

$$\int_0^1 x\sqrt{1-x^2} P_{2l+1}^1(x) dx = -\frac{\sqrt{\pi}(2l+1)(2l+2)}{8\Gamma(\frac{3}{2}-l)\Gamma(3+l)},$$

so that the solution for $\Phi(\mathbf{r})$ is

$$\Phi(\mathbf{r}) = j\omega\Theta L^2 \cos q \sum_{l=0}^{\infty} \frac{I_l}{C_{2l+1}^1(\xi_o)} P_{2l+1}^1(\cos\eta) Q_{2l+1}^1(\cosh\xi),$$

where $I_l = \sqrt{\pi}(4l+3)/(8\Gamma(\frac{3}{2}-l)\Gamma(3+l))$.

3.5.2 Hydrodynamic Torque

The torque on the hemispheroid is given by Equation 4.10. Since

$$\mathbf{r}(\eta, q) = |r|\nabla r = L\sqrt{\cos^2\eta + \sinh^2\xi_o}\nabla r,$$

∇r can be expressed as,

$$\nabla r = \frac{1}{L\sqrt{\sin^2\eta + \sinh^2\xi_o}}(\frac{\partial r}{\partial \xi}\hat{\xi} + \frac{\partial r}{\partial \eta}\hat{\eta}),$$

and $\partial r/\partial \eta$ is equal to

$$\frac{\partial r}{\partial \eta} = \frac{-L\cos\eta\sin\eta}{\sqrt{\cos^2\eta + \sinh^2\xi_o}},$$

$\mathbf{r} \times \hat{\xi}$ can be expressed as

$$\mathbf{r} \times \hat{\xi} = \frac{-L\cos\eta\sin\eta}{\sqrt{\sin^2\eta + \sinh^2\xi_o}}\hat{\mathbf{q}}.$$

With

$$\hat{\mathbf{q}} = (-\sin q\hat{\mathbf{x}} + \cos q\hat{\mathbf{y}}),$$

the torque on the hemispheroid is equal to

$$T = \int_0^{2\pi}\int_0^{\pi/2} P(\mathbf{r}) \cdot (-L^3\sinh\xi_o\sin^2\eta\cos\eta(-\sin q\hat{\mathbf{x}} + \cos q\hat{\mathbf{y}}))d\eta dq.$$

The pressure $P(\mathbf{r})$ can be obtained from Equation 3.2 and Equation 3.6, so that

$$T_t = j\omega\rho L^3 U_b \cosh\xi_o \sinh\xi_o \frac{\pi Q_1^1(\cosh\xi_o)}{4C_1^1(\xi_o)}.$$

For rotational motion, the pressure $P(\mathbf{r})$ can be obtained from Equation 3.2 and Equation 3.9. The result is given by Equation 3.28. This integral may be solved for each term of the associated Legendre series.

Chapter 4

Low frequency solution

4.1 Introduction

In this chapter we show that in the limit of low frequecies, the full linearized Navier-Stokes equation need not be solved, and the simpler Stokes equation can be used. Since an analytic solution to the resulting hydrodynamic equations is not known, an approximate solution is found using a method we call Boundary Element Method with Analytic techniques (BEMA). We start this chapter by describing the Boundary Element Method (BEM), and we subsequently discuss the BEMA, a method which takes advantage of the rotational symmetry of the spheroid and hemispheroid and partially solves the equations of motion analytically. We apply the BEMA to full spheroids with no plate present because exact solutions exist which can check the BEMA results, and because the methods for a full spheroid are the same in many ways as those of the hemispheroid with a plate, so that much of the computer code can be checked. Section 4.5 details the BEMA applied to a hemispheroid with a plate which uses an additional analytic method to solve the equations of motion exactly along the plate. Complex analytic expressions are needed and we apply checks at different stages in the method to verify that the equations of motion for the hemispheroid with a plate are satisfied throughout the fluid. Section 4.6 examines the convergence of the fluid velocities along the boundary surface as well as the hydrodynamic pressure along the surface and the torque induced by the motion of the hemispheroid with a plate.

The final section of this chapter analyzes the results of our numerical simulations and describes the effect of shape on the hydrodynamic pressure, velocity, and torque.

4.2 Boundary Element Methods

The BEM is a numerical approximation of the boundary integral or singularity method (BIM), which represents the solutions to a homogeneous linear differential equation with specified boundary conditions as a weighted integral of Green's functions. Let us begin our discussion of the BEM with a description of the BIM.

4.2.1 Boundary integral or singularity methods

Let

$$D(y(\mathbf{r})) = 0, \tag{4.1}$$

represent a homogeneous linear differential equation with conditions along the boundary surface,

$$y(\mathbf{r}') = g(\mathbf{r}'), \tag{4.2}$$

where $\mathbf{r}'$ represents a vector to a point on the boundary surface and $g(r)$ is some arbitrary function. The solution to Equation 4.1 can be expressed as,

$$y(\mathbf{r}) = \int_{S'} G(\mathbf{r}, \mathbf{r}') f_{fict}(\mathbf{r}') dS',$$

where $G(\mathbf{r})$ is the Green's function or impulse response of the Equation 4.1, i.e.,

$$D(G(\mathbf{r})) = \delta(\mathbf{r}).$$

f_{fict} are the weightings of the impulses located along the surface that are needed to satisfy the surface boundary conditions, Equation 4.2; S' represents the surface, and $\mathbf{r}'$ represents a vector to the surface (Figure 4-1). (If Neumann conditions are specified, then $dG(\mathbf{r})/dr$ is used.) Once the weightings are found, all other physical properties can be obtained by using the appropriate Green's function. There are three categories of BEM–indirect, semi-direct and direct (Becker, 1992). In the indirect BEM, the weightings have no physical significance, but can be integrated to find all the real physical quantities. In the semi-direct BEM, the weightings are not actual

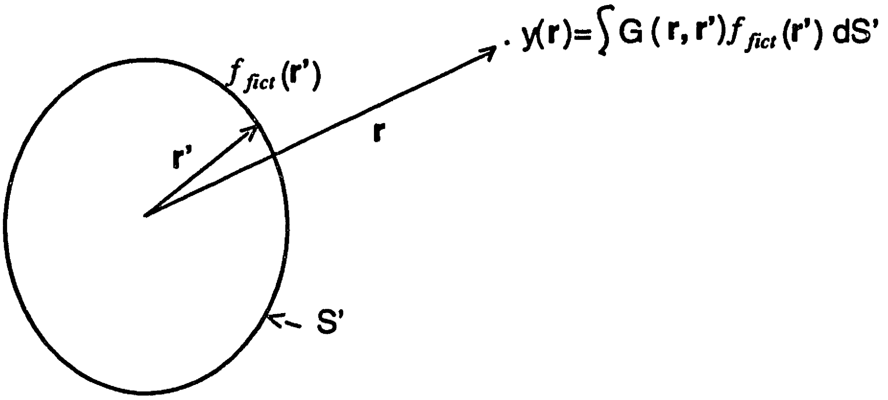

Figure 4-1: The boundary integral method- f_{fict} are the weightings of the Green's functions along the surface that are needed to match the surface boundary conditions, S' represents the boundary surface, and $\mathbf{r}'$ represents a vector to that surface.

physical properties but can be related to physical properties. In the direct method, the weightings represent actual physical properties. In this thesis, we will be using the indirect BEM which, for our applications, have simpler Green's functions and are easier to integrate.

4.2.2 Green's functions for Stokes' flow

For slow, viscous, incompressible fluid, conservation of momentum is described by Stokes' equation,

$$\mu\nabla^2\mathbf{U}(\mathbf{r}) - \nabla P(\mathbf{r}) = 0,$$

and conservation of mass is described by

$$\nabla \cdot \mathbf{U}(\mathbf{r}) = 0.$$

Therefore, the Green's functions for Stokes' flow satisfy

$$-\nabla G_{px}(\mathbf{r}) + \mu\nabla^2\mathbf{G}_{ux}(\mathbf{r}) = \hat{\mathbf{x}}\delta(\mathbf{r}),$$
$$\nabla \cdot \mathbf{G}_{ux}(\mathbf{r}) = 0,$$

$$-\nabla G_{py}(\mathbf{r}) + \mu\nabla^2\mathbf{G}_{uy}(\mathbf{r}) = \hat{\mathbf{y}}\delta(\mathbf{r}), \tag{4.3}$$
$$\nabla\cdot\mathbf{G}_{uy}(\mathbf{r}) = 0,$$

$$-\nabla G_{pz}(\mathbf{r}) + \mu\nabla^2\mathbf{G}_{uz}(\mathbf{r}) = \hat{\mathbf{z}}\delta(\mathbf{r}),$$
$$\nabla\cdot\mathbf{G}_{uz}(\mathbf{r}) = 0,$$

where $G_{pi}(\mathbf{r})$ and $\mathbf{G}_{ui}(\mathbf{r})$ represent the pressure and velocity Green's functions due to an impulse of force in the i^{th} direction.

The Green's functions of Equation 4.3 are called stokeslets (Pozrikidis, 1989). G_{ux}, the velocity due to the x component of an impulse can be expressed as

$$\mathbf{G}_{ux}(\mathbf{r}) = \frac{1}{8\pi\mu}\left(\frac{\hat{\mathbf{x}}}{r} + \frac{x^2\hat{\mathbf{x}} + xy\hat{\mathbf{y}} + xz\hat{\mathbf{z}}}{r^3}\right).$$

The velocities due to the other components have similar forms. The pressure stokeslet can be expressed as

$$\mathbf{G}_p(\mathbf{r}) = \frac{1}{4\pi}\left(\frac{x\hat{\mathbf{x}} + y\hat{\mathbf{y}} + z\hat{\mathbf{z}}}{r^3}\right). \tag{4.4}$$

For Stokes flow in the presence of boundary surfaces, the solution for the i^{th} component of the velocity can be expressed as

$$U_i(\mathbf{r}) = \int_{S'} \mathbf{G}_{ui}(\mathbf{r},\mathbf{r}')\cdot\mathbf{f}_{fict}(\mathbf{r}')dS',^1 \tag{4.5}$$

and the pressure as

$$P(\mathbf{r}) = \int_{S'} \mathbf{G}_p(\mathbf{r},\mathbf{r}')\cdot\mathbf{f}_{fict}(\mathbf{r}')dS'. \tag{4.6}$$

$\mathbf{f}_{fict}(\mathbf{r}')$ represents the weightings of the impulses along the surface. Since each impulse has a direction, $\mathbf{f}_{fict}(\mathbf{r}')$ is a vector. From Equation 2.3 and Equation 2.4, the torque exerted by the i^{th} component of an impulse on a surface S surrounding the impulse

---

[1] This is true since the i^{th} component of a velocity stokeslet due to an in impulse in the j^{th} direction is equal to the j^{th} component of a velocity stokeslet due to an in impulse in the i^{th} direction.

can be expressed as

$$\mathbf{G}_{Ti}(\mathbf{r}') = \int_S \hat{\mathbf{G}}_{Ti}(\mathbf{r}',\mathbf{r})dS, \tag{4.7}$$

where

$$\hat{\mathbf{G}}_{Ti}(\mathbf{r}) = \mathbf{r} \times (\hat{n}G_{pi}(\mathbf{r}) + \mu\nabla(\hat{n} \cdot \mathbf{G}_{ui}(\mathbf{r})) + \mu(\hat{n} \cdot \nabla)\mathbf{G}_{ui}(\mathbf{r})), \tag{4.8}$$

and can be considered a Green's function for torque per unit area. We can consider the Green's function given in Equation 4.7 and Equation 4.8 as the torque stokeslet, and we can therefore express the i^{th} component of torque as

$$T_i = \int_{S'} \mathbf{G}_{Ti}(\mathbf{r}') \cdot \mathbf{f}_{fict}(\mathbf{r}')dS'.$$

4.2.3 Boundary element methods

For most problems, $\mathbf{f}_{fict}$ cannot be obtained by analytic techniques, and a numerical approximation of the boundary integral method, the BEM, is used to obtain an approximation of $\mathbf{f}_{fict}$ (Pozrikidis, 1992). With the BEM, the surface boundaries are broken into N elements with an approximation of $\mathbf{f}_{fict}$ in each element. There are many ways to approximate the continuous BIM with a discrete representation. We use a constant approximation for $\mathbf{f}_{fict}$, so that the integrals of Equation 4.5 and Equation 4.6 become sums, i.e.,

$$U_i(\mathbf{r}) \approx \sum_{j=1}^{N} \int_{dS'_j} \mathbf{G}_{ui}(\mathbf{r},\mathbf{r}') \cdot \hat{\mathbf{f}}_{fici,j} dS'_j,$$

$$P(\mathbf{r}) \approx \sum_{j=1}^{N} \int_{dS'_j} \mathbf{G}_{p}(\mathbf{r},\mathbf{r}') \cdot \hat{\mathbf{f}}_{fict,j} dS'_j.$$

$\hat{\mathbf{f}}_{fict}(\mathbf{r}')$ is the piecewise constant approximation of $\mathbf{f}_{fict}(\mathbf{r}')$. We use a collocation method to obtain $\hat{\mathbf{f}}_{fict}$. We break the surface into N elements and approximate $U_i(\mathbf{r})$ as $\hat{U}_i^k$, a piecewise constant function with $\hat{U}_i^k = U_i(\mathbf{r}_k)$, the velocity at the midpoint of the k^{th} element. We set $\hat{U}_i^k$ to the known boundary conditions, $U_{surf,i}(\mathbf{r}_k)$ so that

$$U_{surf,i}(\mathbf{r}_k) = \hat{U}_i^k = \sum_{j=1}^{N} \int_{dS'_j} \mathbf{G}_{ui}(\mathbf{r}_k, \mathbf{r}') \cdot \hat{\mathbf{f}}_{fict,j} dS'_j. \tag{4.9}$$

The midpoint of each element is known as the collocation point. $\hat{\mathbf{f}}_{fict}$ is found by solving Equation 4.9, for each element, for each component of the velocity (Figure 4-2). Therefore, a $3N$ by $3N$ matrix must be inverted. The following summarizes the steps of the BEM:

- *Step 1:*

  Break surface S into N elements, the j^{th} element has area S_j.

- *Step 2:*

  Compute a $3N$ by $3N$ matrix of fluid velocities. Each entry is G_{uijkl}, the fluid velocity in the $\hat{\mathbf{x}}_i$ direction, at $\mathbf{r}_k$, due to a constant distribution of impulses along S_j, in the $\hat{\mathbf{x}}_l$ direction. Rows of the matrix specify the surface velocities that result for each fictitious source. Columns specify the contributions of all fictitious sources to each surface velocity.

- *Step 3:*

  Solve a system of $3N$ equations,

  $$U_{surf,i}(\mathbf{r}_k) = G_{uijkl}\hat{f}_{fict,jl},$$

  for the $3N$ unknowns, $\hat{f}_{fict,jl}$.

- *Step 4:*

  Compute entries for matrices $G_{uijl}(\mathbf{r})$, (a $3N$ by 3 matrix), $G_{pjl}(\mathbf{r})$, (a $3N$ by 1 matrix), and $G_{Tijl}(\mathbf{r})$ (a $3N$ by 3 matrix) to calculate velocity and pressure at a point $\mathbf{r}$, and the torque on the body, respectively. Since velocity and torque are vectors, the matrices for velocity and torque consist of three rows.

  Compute velocity, pressure, and torque using $\hat{f}_{fict,jl}$,

  $$\begin{aligned} U_i(\mathbf{r}) &= G_{uijl}(\mathbf{r})\hat{f}_{fict,jl} \\ P(\mathbf{r}) &= G_{pjl}(\mathbf{r})\hat{f}_{fict,jl} \\ T_i(\mathbf{r}) &= G_{Tijl}(\mathbf{r})\hat{f}_{fict,jl} \end{aligned}$$

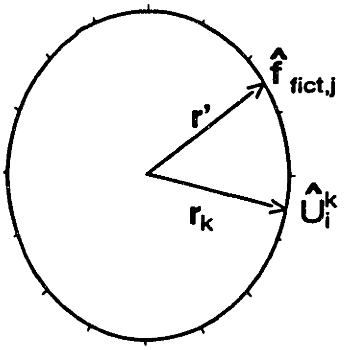

Figure 4-2: In the BEM, the surface is broken into N elements, and the weightings of the impulses are assumed to be constant in an element. The i^{th} component of velocity of the k^{th} element is given by $\hat{U}_i^k = \sum_{j=1}^{N} \int_{dS'} \mathbf{G}_{ui}(\mathbf{r}, \mathbf{r}') \cdot \hat{\mathbf{f}}_{fict,j} dS'$.

Note that the calculation of the torque is somewhat more complicated than that of velocity and pressure since an additional integration over the surface is required.

4.2.4 Non-integrable singularities in the pressure and torque stokeslets

The pressure and torque stokeslets have non-integrable singularities on the boundary surface. Therefore, in this thesis, we approximate the hydrodynamic pressure on the surface with the hydrodynamic pressure a small distance away from the surface. However, the torque on the body can still be calculated exactly despite the non-integrable singularity. This is because the integration over S need not be over the surface of the body– any surface that encloses the stokeslets will do because the torque induced by the fluid on a closed surface is zero, i.e.,

$$\mathbf{T} = \int_S \mathbf{r} \times (P\mathbf{n} - \bar{\tau}\mathbf{n}) = \int_V \mathbf{r} \times (\nabla P(\mathbf{r}) - \mu \nabla^2 U(\mathbf{r})) dV = 0, \tag{4.10}$$

where $\bar{\tau}$ is a tensor that represents the fluid shear. The appendix to this chapter contains a derivation of this result.

4.3 BEM with Analytic techniques—BEMA

In this section we will derive analytic expressions for the azimuthal dependence of the $\mathbf{f}_{fict}(\mathbf{r}')$ for structures with rotational symmetry about the z axis, and with motions only in the x-z plane. We will incorporate this dependence into the BEM, and we will call the BEM with the known azimuthal dependence of the weightings, BEMA—Boundary Integral methods with Analytic techniques.

4.3.1 Simplifications for structures with rotational symmetry about the z axis, with motions only in the x-z plane

Using Fourier analysis, we will derive the q' dependence of $\mathbf{f}_{fict}(\mathbf{r}')$ for the spheroidal structures we are considering in this thesis. It can be shown (Dean and O'Neill, 1963) that for structures that are symmetric about the z axis, and with motions only in the x-z plane, the hydrodynamic pressure and velocity can be expressed as

$$\begin{aligned} P(\xi,\eta,q) &= f_1(\xi,\eta)\cos q, && (4.11)\\ U_x(\xi,\eta,q) &= f_2(\xi,\eta)\cos^2 q + f_3(\xi,\eta), && (4.12)\\ U_y(\xi,\eta,q) &= f_4(\xi,\eta)\cos q \sin q, && (4.13)\\ U_z(\xi,\eta,q) &= f_5(\xi,\eta)\cos q. && (4.14) \end{aligned}$$

We will use the known q dependence of the pressure to derive the q' dependence of $\mathbf{f}_{fict}(\mathbf{r}')$. For this analysis, we will consider only boundary surfaces of spheroids, so that $\mathbf{f}_{fict}(\mathbf{r}')$ depends only on η' and q' and is independent of ξ'. We will check our results by checking that the resulting velocities induced by the stokeslets have the correct q dependence.

The following summarizes the steps of the method used to obtain the q' dependence:

- *Step 1:*

  Represent $\mathbf{f}_{fict}(\mathbf{r}')$ as a Fourier series in q',

$$\begin{aligned}\mathbf{f}_{fict}(\eta', q') &= \sum_{j=0}^{\infty}((\tilde{a}_{xj}(\eta')\cos(jq') + \tilde{b}_{xj}(\eta')\sin(jq'))\hat{\mathbf{x}} \\ &+ (\tilde{a}_{yj}(\eta')\cos(jq') + \tilde{b}_{yj}(\eta')\sin(jq'))\hat{\mathbf{y}} \\ &+ (\tilde{a}_{zj}(\eta')\cos(jq') + \tilde{b}_{zj}(\eta')\sin(jq'))\hat{\mathbf{z}}). \qquad (4.15)\end{aligned}$$

- *Step 2:*

  Express $G_p(\mathbf{r}, \mathbf{r}')$ in spheroidal coordinates.

- *Step 3:*

  Calculate $P(\mathbf{r}) = \int \mathbf{G}_p(\mathbf{r}, \mathbf{r}')\mathbf{f}_{fict}(\eta', q')d\eta' dq$. Let $q'' = q' + q$, and perform the integration in q'' instead of q'. This shift simplifies the integration and since the integral is over a full period, it does not affect the integration. The terms that are odd functions of q'' integrate to zero.

- *Step 4:*

  See which terms of the Fourier series of $\mathbf{f}_{fict}(\mathbf{r}')$ give the pressure terms with $\cos q$ dependence.

- *Step 5:*

  The result is

$$f_{fict,x}(\eta', q') = a_{x0}(\eta') + a_{x2}(\eta')\cos^2 q', \qquad (4.16)$$

$$f_{fict,y}(\eta', q') = a_{x2}(\eta')\sin q' \cos q', \qquad (4.17)$$

$$f_{fict,z}(\eta', q') = a_{z1}(\eta')\cos q', \qquad (4.18)$$

  where $a_{x0}(\eta') = \tilde{a}_{x0}(\eta') - \tilde{a}_{x2}(\eta')$, $a_{x2}(\eta') = 2\tilde{a}_{x2}(\eta')$, and $a_{z1}(\eta') = \tilde{a}_{z1}(\eta')$.

This method is discussed in more detail in the appendix to this chapter. Note that although there are four different q' dependencies, 1, $\cos q'$, $\cos q' \sin q'$, and $\cos^2 q'$, there are only three weighting functions, $a_{x0}(\eta')$, $a_{x2}(\eta')$, and $a_{z1}(\eta')$; the $\hat{\mathbf{x}} \cos^2 q'$ term must have the same weighting as the $\hat{\mathbf{y}} \sin q' \cos q'$ in order to obtain the $\cos q$ dependence of the pressure. Having determined the q' dependence of $\mathbf{f}_{fict}(\eta', q')$, we can integrate Equation 4.5 and Equation 4.6 analytically with respect to q'. To simplify the expressions for pressure and velocity, let $\tilde{f}_m(q')$ be the following functions of q',

$$\begin{aligned}
\tilde{f}_0(q') &= 1, \\
\tilde{f}_1(q') &= \cos q', \\
\tilde{f}_2(q') &= \cos^2 q', \\
\tilde{f}_3(q') &= \sin q' \cos q',
\end{aligned}$$

and let $\tilde{G}_{ijk}(\mathbf{r}, \xi', \eta')$ represent either the integrated velocity stokeslet in $\hat{\mathbf{x}}_i$, or the integrated pressure stokeslet if $i = p$, due to a source in $\hat{\mathbf{x}}_j$ with strength, $\tilde{f}_k(q')$, i.e.,

$$\tilde{G}_{ijk}(\mathbf{r}, \xi', \eta') = \int_0^{2\pi} h_2(\xi', \eta') \mathbf{G}_{ui}(\mathbf{r}, \mathbf{r}') \cdot \hat{\mathbf{x}}_j \tilde{f}_k(q') dq',$$

$$\tilde{G}_{pjk}(\mathbf{r}, \xi', \eta') = \int_0^{2\pi} h_2(\xi', \eta') \mathbf{G}_p(\mathbf{r}, \mathbf{r}') \cdot \hat{\mathbf{x}}_j \tilde{f}_k(q') dq'.$$

Equation 4.5 and Equation 4.6 can now be written as

$$\begin{aligned}
U_i(\mathbf{r}) &= \int_0^{\pi} d\eta' h_1(\xi', \eta') \times (\tilde{G}_{ix0}(\mathbf{r}, \xi', \eta') a_{x0}(\eta') \\
&+ \tilde{G}_{ix2}(\mathbf{r}, \xi', \eta') a_{x2}(\eta') + \tilde{G}_{iy3}(\mathbf{r}, \xi', \eta') a_{x2}(\eta') + \tilde{G}_{iz1}(\mathbf{r}, \xi', \eta') a_{z1}(\eta')),
\end{aligned}$$

$$\begin{aligned}
P(\mathbf{r}) &= \int_0^{\pi} d\eta' h_1(\xi', \eta') \times (\tilde{G}_{px0}(\mathbf{r}, \xi', \eta') a_{x0}(\eta') \\
&+ \tilde{G}_{px2}(\mathbf{r}, \xi', \eta') a_{x2}(\eta') + \tilde{G}_{py3}(\mathbf{r}, \xi', \eta') a_{x2}(\eta') + \tilde{G}_{pz1}(\mathbf{r}, \xi', \eta') a_{z1}(\eta')),
\end{aligned}$$

If we factor out from $\tilde{G}_{ijk}(\mathbf{r},\eta')$ the terms that only depend on q, we can express the components of the velocity as

$$
\begin{aligned}
U_x(\mathbf{r}) = \int_0^\pi & d\eta' h_1(\xi',\eta') \times \\
& ((\hat{G}^0_{xx}(\xi,\eta,\xi',\eta') + \hat{G}^2_{xx}(\xi,\eta,\xi',\eta')\cos^2 q)a_{x0}(\eta') \\
+ & (\hat{G}^0_{x(x+y)}(\xi,\eta,\xi',\eta') + \hat{G}^2_{x(x+y)}(\xi,\eta,\xi',\eta')\cos^2 q)a_{x2}(\eta') \\
+ & (\hat{G}^0_{xz}(\xi,\eta,\xi',\eta') + \hat{G}^2_{xz}(\xi,\eta,\xi',\eta')\cos^2 q)a_{z1}(\eta')),
\end{aligned}
$$

$$
\begin{aligned}
U_y(\mathbf{r}) = & \cos q \sin q \int_0^\pi d\eta' h_1(\xi',\eta') \times \\
& (\hat{G}^3_{yx}(\xi,\eta,\xi',\eta')a_{x0}(\eta') + \hat{G}^3_{y(x+y)}(\xi,\eta,\xi',\eta')a_{x2}(\eta') + \hat{G}^3_{yz}(\xi,\eta,\xi',\eta')a_{z1}(\eta')),
\end{aligned}
$$

$$
\begin{aligned}
U_z(\mathbf{r}) = & \cos q \int_0^\pi d\eta' h_1(\xi',\eta') \times \\
& (\hat{G}^1_{zx}(\xi,\eta,\xi',\eta')a_{x0}(\eta') + \hat{G}^1_{z(x+y)}(\xi,\eta,\xi',\eta')a_{x2}(\eta') + \hat{G}^1_{zz}(\xi,\eta,\xi',\eta')a_{z1}(\eta')),
\end{aligned}
$$

where $\hat{G}^i_{jk}$ represents combinations or portions of the integrated Green's functions without the q dependences, i denotes q dependence in the same way that i denotes q dependence of $\tilde{f}_i(q)$; j denotes $\hat{\mathbf{x}}_j$, the velocity direction; and k denotes $\hat{\mathbf{x}}_k$, the source directions. If $k = x + y$, then $\hat{G}^i_{jk}$ represents a sum of integrated Green's functions due to sources in $\hat{\mathbf{x}}$ with a $\cos^2 q'$ dependence and $\hat{\mathbf{y}}$ with a $\sin q' \cos q'$ dependence. The pressure can be expressed as

$$
\begin{aligned}
P(\mathbf{r}) = & \cos q \int_0^\pi d\eta' h_1(\xi',\eta') \times \\
& (\hat{G}^1_{px}(\xi,\eta,\xi',\eta')a_{x0}(\eta') + \hat{G}^1_{p(x+y)}(\xi,\eta,\xi',\eta')a_{x2}(\eta') + \hat{G}^1_{pz}(\xi,\eta,\xi',\eta')a_{z1}(\eta')).
\end{aligned}
$$

Using the known q dependencies of the hydrodynamic pressure for structures with rotational symmetry about the z axis, with motion solely in the x-z plane, we have derived the correct q' dependences of $f_{fict}(\mathbf{r}')$, and we have indicated that these dependencies lead to the correct q dependencies of the velocity components.

4.3.2 Numerical methods— the η' dependencies of $\mathbf{f}_{fict}$

Since we are unable to determine the η' dependencies of $\mathbf{f}_{fict}(\eta', q')$ exactly, we must now rely on numerical methods. To derive the η dependence of $\mathbf{f}_{fict}(\eta', q')$, that is, to solve for $a_{x0}(\eta')$, $a_{x2}(\eta')$ and $a_{z1}(\eta')$, we use the BEM discussed previously. Only an arc of the spheroid need be broken into elements, since we have solved for the q' dependence. Breaking up the surface into N elements along an arc of constant q', the fluid velocity and pressure can be represented as

$$\begin{aligned} U_x(\mathbf{r}) = & \sum_{j=1}^{N} \int_{\frac{\pi(j-1)}{N}}^{\frac{\pi j}{N}} d\eta' h_1(\xi', \eta') \times \\ & ((\hat{G}^0_{xx}(\xi, \eta, \xi', \eta') + \hat{G}^2_{xx}(\xi, \eta, \xi', \eta') \cos^2 q)\hat{a}_{x0,j} \\ + & (\hat{G}^0_{x(x+y)}(\xi, \eta, \xi', \eta') + \hat{G}^2_{x(x+y)}(\xi, \eta, \xi', \eta') \cos^2 q)\hat{a}_{x2,j} \\ + & (\hat{G}^0_{xz}(\xi, \eta, \xi', \eta') + \hat{G}^2_{xz}(\xi, \eta, \xi', \eta') \cos^2 q)\hat{a}_{z1,j}), \end{aligned} \tag{4.19}$$

$$\begin{aligned} U_y(\mathbf{r}) = & \cos q \sin q \sum_{j=1}^{N} \int_{\frac{\pi(j-1)}{N}}^{\frac{\pi j}{N}} d\eta' h_1(\xi', \eta') \times \\ & (\hat{G}^3_{yx}(\xi, \eta, \xi', \eta')\hat{a}_{x0,j} + \hat{G}^3_{y(x+y)}(\xi, \eta, \xi', \eta')\hat{a}_{x2,j} + \hat{G}^3_{yz}(\xi, \eta, \xi', \eta')\hat{a}_{z1,j}), \end{aligned} \tag{4.20}$$

$$\begin{aligned} U_z(\mathbf{r}) = & \cos q \sum_{j=1}^{N} \int_{\frac{\pi(j-1)}{N}}^{\frac{\pi j}{N}} d\eta' h_1(\xi', \eta') \times \\ & (\hat{G}^1_{zx}(\xi, \eta, \xi', \eta')\hat{a}_{x0,j} + \hat{G}^1_{z(x+y)}(\xi, \eta, \xi', \eta')\hat{a}_{x2,j} + \hat{G}^1_{zz}(\xi, \eta, \xi', \eta')\hat{a}_{z1,j}), \end{aligned} \tag{4.21}$$

$$\begin{aligned} P(\mathbf{r}) = & \cos q \sum_{j=1}^{N} \int_{\frac{\pi(j-1)}{N}}^{\frac{\pi j}{N}} d\eta' h_1(\xi', \eta') \times \\ & (\hat{G}^1_{zx}(\xi, \eta, \xi', \eta')\hat{a}_{x0,j} + \hat{G}^1_{z(x+y)}(\xi, \eta, \xi', \eta')\hat{a}_{x2,j} + \hat{G}^1_{zz}(\xi, \eta, \xi', \eta')\hat{a}_{z1,j}), \end{aligned} \tag{4.22}$$

where $\hat{a}_{x0}$, $\hat{a}_{x2}$, and $\hat{a}_{z1}$ represent piecewise constant approximations to $a_{x0}(\eta')$, $a_{x2}(\eta')$ and $a_{z1}(\eta')$.

To determine $\hat{a}_{x0}$, $\hat{a}_{x2}$, and $\hat{a}_{z1}$, boundary conditions are needed. However, because the dependence of $\mathbf{f}_{fict}(\eta', q')$ on q' has already been determined, only the velocities for an arc of constant q' need be set. The following summarizes the steps of the BEMA:

- *Step 1:*

  Using the known weightings in q', integrate the Green's functions with respect to q'.

- *Step 2:*

  Break contour of constant q' into N elements, the j^{th} element has area S_j.

- *Step 3:*

  Compute a $3N$ by $3N$ matrix of fluid velocities using the stokeslets and image stokeslets. Each entry is G_{uijkl}, the velocity in the $\hat{\mathbf{x}}_i$ direction, at $\mathbf{r}_k$, due to a constant distribution of impulses along S_j, in the $\hat{\mathbf{x}}_l$ direction.

- *Step 4:*

  Solve a system of $3N$ equations,

  $$U_{surf,i}(\mathbf{r}_k) = G_{uijkl}\hat{a}_{jl},$$

  for the N unknowns, $\hat{a}_{jl}$ with $\hat{a}_{j1} = \hat{a}_{x0,j}$, $\hat{a}_{j2} = \hat{a}_{x2,j} = \hat{a}_{y2,j}$, $\hat{a}_{j3} = \hat{a}_{z1,j}$.

- *Step 5:*

  Compute entries for matrices $G_{uijl}(\mathbf{r})$, (a $3N$ by 3 matrix), $G_{pjl}(\mathbf{r})$, (an $3N$ by 1 matrix), and $G_{Tyjl}(\mathbf{r})$ (an N by 1 matrix) using stokeslets and image stokeslets.

  Compute velocity, pressure, and torque using $\hat{a}_{jl}$,

  $$\begin{aligned} U_i(\mathbf{r}) &= G_{uijl}(\mathbf{r})\hat{a}_{jl} \\ P(\mathbf{r}) &= G_{pjl}(\mathbf{r})\hat{a}_{jl} \\ T_y(\mathbf{r}) &= G_{T2jl}(\mathbf{r})\hat{a}_{jl} \end{aligned}$$

4.3.3 Other analytic techniques

Other analytic techniques can be incorporated into BEMA to simplify the numerics; for full spheroids, which are symmetric about the x-y plane, we will take advantage of this symmetry and only discretize the upper half of the spheroid. For hemispheroids hinged to a plate, we will use a Green's function that gives the correct fluid velocities along the plate, so the plate needn't be discretized. These methods will be discussed in more detail in the next few sections.

4.4 Analysis of full spheroid in uniform and shear flows using BEMA and symmetry

In this section, we describe the results of the BEMA for a stationary full spheroid in uniform and shear steady flow. The numerics of the BEMA will be further simplified by using symmetry to predict the stokeslet weightings in the lower half of the spheroid. Since there are known exact solutions (see appendix of this chapter), we can check the BEMA results and gain understanding of the sources of error. This exercise also serves as a partial check on the BEMA applied to a hemispheroid with a plate since there is much overlap in the the numerical code used to solve the two problems.

4.4.1 Boundary conditions

For uniform flow, let the fluid velocity far from the spheroid be represented by $-U_b\hat{\mathbf{x}}$, and for shear flow, let the fluid velocity far from the spheroid be represented by $-\Omega z\hat{\mathbf{x}}$. If we shift reference frames to be such that the fluid is stationary at infinity, the fluid velocity along the surface of the spheroid, in the new reference frame is given by

$$\mathbf{U}(\xi = \xi_o, \eta, q) \;=\; U_b\hat{\mathbf{x}},$$

for uniform flow, and for shear flow, it is given by

$$\mathbf{U}(\xi = \xi_o, \eta, q) \;=\; \Omega z\hat{\mathbf{x}}.$$

Exact solutions to Stokes equation with these boundary conditions are found in the appendix. From symmetry it has been determined that for a full spheroid, $a_{x2}(\eta') = 0$, so that either $U_y(\xi = \xi_o, \eta, q)$ or $U_z(\xi = \xi_o, \eta, q)$ need be set to zero. We arbitrarily chose $U_z(\xi = \xi_o, \eta, q)$, and use the known surface velocity U_y to check our results.

4.4.2 Symmetry

Because the spheroid and boundary conditions are symmetric about the equatorial plane, where $\eta = \pi/2$, only the half contour, of constant q, above the equator, need be discretized by adding or subtracting to the stokeslet, its image stokeslet. The $\mathbf{x}$ and $\mathbf{y}$ components of stokeslets due to impulses in $\hat{\mathbf{x}}$ are symmetric about the equatorial plane as is the $\mathbf{z}$ component of stokeslets due to impulses in $\hat{\mathbf{z}}$. The other stokeslets are antisymmetric. Since the boundary conditions are symmetric in $\hat{\mathbf{x}}$ and $\hat{\mathbf{z}}$ for uniform flow and in $\hat{\mathbf{z}}$ for shear flow, but are antisymmetric in $\hat{\mathbf{x}}$ for shear flow, the sign of the image stokeslets in $\hat{\mathbf{x}}$ for shear flow are negative. Therefore, Equation 4.19-Equation 4.22 can be expressed as

$$
\begin{aligned}
U_x(\mathbf{r}) &= \sum_{j=1}^{N} \int_{\frac{\pi(j-1)}{N}}^{\frac{\pi j}{N}} d\eta' h_1(\xi', \eta') \times ((\hat{G}^0_{xx}(\xi, \eta, \xi', \eta') \\
&\pm (\hat{G}^0_{xx}(\xi, \eta, \xi', \pi - \eta') + (\hat{G}^2_{xx}(\xi, \eta, \xi', \eta') \pm \hat{G}^2_{xx}(\xi, \eta, \xi', \pi - \eta')) \cos^2 q) \hat{a}_{x0,j} \\
&+ (\hat{G}^0_{xz}(\xi, \eta, \xi', \eta') + \hat{G}^0_{xz}(\xi, \eta, \xi', \pi - \eta') \\
&+ (\hat{G}^2_{xz}(\xi, \eta, \xi', \eta') + \hat{G}^2_{xz}(\xi, \eta, \xi', \pi - \eta')) \cos^2 q) \hat{a}_{z1,j}),
\end{aligned}
$$

$$
\begin{aligned}
U_y(\mathbf{r}) &= \cos q \sin q \sum_{j=1}^{N} \int_{\frac{\pi(j-1)}{N}}^{\frac{\pi j}{N}} d\eta' h_1(\xi', \eta') \times ((\hat{G}^3_{yx}(\xi, \eta, \xi', \eta') \\
&\pm \hat{G}^3_{yx}(\xi, \eta, \xi', \pi - \eta')) \hat{a}_{x0,j} + (\hat{G}^3_{yz}(\xi, \eta, \xi', \eta') + \hat{G}^3_{yz}(\xi, \eta, \xi', \pi - \eta')) \hat{a}_{z1,j}),
\end{aligned}
$$

$$
\begin{aligned}
U_z(\mathbf{r}) &= \cos q \sum_{j=1}^{N} \int_{\frac{\pi(j-1)}{N}}^{\frac{\pi j}{N}} d\eta' h_1(\xi', \eta') \times ((\hat{G}^1_{zx}(\xi, \eta, \xi', \eta') \\
&\pm (\hat{G}^1_{zx}(\xi, \eta, \xi', \pi - \eta')) \hat{a}_{x0,j} + (\hat{G}^1_{zz}(\xi, \eta, \xi', \eta') + \hat{G}^1_{zz}(\xi, \eta, \xi', \pi - \eta')) \hat{a}_{z1,j}),
\end{aligned}
$$

$$
\begin{aligned}
P(\mathbf{r}) &= \cos q \int_{\frac{\pi(j-1)}{N}}^{\frac{\pi j}{N}} d\eta' h_1(\xi', \eta') \times ((\hat{G}^1_{zx}(\xi, \eta, \xi', \eta') \\
&\pm \hat{G}^1_{zx}(\xi, \eta, \xi', \pi - \eta')) \hat{a}_{x0,j} + (\hat{G}^1_{zz}(\xi, \eta, \xi', \eta') + \hat{G}^1_{zz}(\xi, \eta, \xi', \pi - \eta')) \hat{a}_{z1,j}),
\end{aligned}
$$

where $\hat{G}^i_{jk}(\xi, \eta, \xi', \pi - \eta')$ denotes the image stokeslet.The + sign is used for uniform flow, and the − sign, for shear flow.

4.4.3 The numerical integration of the Green's function with respect to η'

The Green's functions are integrated numerically with respect to η' using an iterative trapezoidal rule with a user specified relative accuracy set by a parameter, ϵ which is defined as the magnitude of the ratio between the difference in two successive estimates and the value of the latest estimate.

4.4.4 The matrix inversion

With $N/2$ contour elements, an N by N matrix is obtained. To determine $\hat{a}_{x0}$ and $\hat{a}_{z1}$, the matrix is inverted using Mathematica's Inverse subroutine which inverts this type of matrix by Gaussian elimination.

The following summarizes the steps of the BEMA applied to the full spheroid in uniform or shear steady flow:

- *Step 1:*

  Using the known weightings in q', integrate the Green's functions with respect to q'.

- *Step 2:*

  Break contour of constant q' into $N/2$ elements, the j^{th} element has length S_j.

- *Step 3:*

  Compute a N by N matrix of fluid velocities using the stokeslets and image stokeslets. Each entry is G_{uijkl}, the fluid velocity in the $\hat{\mathbf{x}}_i$ direction, at $\mathbf{r}_k$, due to a constant distribution of impulses along S_j, in the $\hat{\mathbf{x}}_l$ direction. For the full spheroid, the indices, i and l have two values, either 1 or 3 indicating $\hat{\mathbf{x}}$ or $\hat{\mathbf{z}}$.

- *Step 4:*

  Solve a system of N equations,

  $$U_{surf,i}(\mathbf{r}_k) = G_{uijkl}\hat{a}_{jl},$$

  for the N unknowns, $\hat{a}_{jl}$ with $\hat{a}_{j1} = \hat{a}_{x0,j}$, and $\hat{a}_{j3} = \hat{a}_{z1,j}$.

- *Step 5:*

  Compute entries for matrices $G_{uijkl}(\mathbf{r})$, (an N by 3 matrix), $G_{pjl}(\mathbf{r})$, (an N by 1 matrix), and $G_{Tyjl}(\mathbf{r})$ (an N by 1 matrix) using stokeslets and image stokeslets.

  Compute velocity, pressure, and torque using $\hat{a}_{jl}$,

  $$\begin{aligned} U_i(\mathbf{r}) &= G_{uijl}(\mathbf{r})\hat{a}_{jl} \\ p(\mathbf{r}) &= G_{pjl}(\mathbf{r})\hat{a}_{jl} \\ T_y(\mathbf{r}) &= G_{Tyjl}(\mathbf{r})\hat{a}_{jl} \end{aligned}$$

4.4.5 The torque calculation

The calculation of the torque is somewhat more complicated than that of velocity and pressure since an additional integration over the surface is required. Using Equation 4.7 and Equation 4.8, the torque, which, for the structures considered here, is completely in $\hat{\mathbf{y}}$, can be expressed as

$$T_y \approx \int_S dS \sum_{j=1}^{N} \int_{dS'_j} \hat{\mathbf{G}}_{ti}(\mathbf{r}, \mathbf{r}') \cdot \hat{\mathbf{x}}_{fict,j} dS'_j.$$

The torque can be found by first analytically integrating $\hat{\mathbf{G}}_{ti}(\mathbf{r}, \mathbf{r}')$ over q' and q, numerically integrating over $d\eta'$, summing the dot product of the result and the fictitious sources, integrating over $d\eta$, and then summing the result,

$$\begin{aligned} T_y &\approx \sum_{k=1}^{N} \int_{\frac{\pi(k-1)}{N}}^{\frac{\pi k}{N}} d\eta h_1(\eta, \xi) h_2(\eta, \xi) \\ &\times \sum_{j=1}^{N} \int_{\frac{\pi(j-1)}{N}}^{\frac{\pi j}{N}} d\eta' h_1(\eta', \xi') h_2(\eta', \xi') \int_q dq \int_{q'} dq' \hat{\mathbf{G}}_{ti}(\mathbf{r}_k, \mathbf{r}') \cdot \hat{\mathbf{x}}_{fict,j} \\ &= 2 \sum_{k=1}^{N/2} \int_{\frac{\pi(k-1)}{2N}}^{\frac{\pi k}{2N}} d\eta h_1(\eta, \xi) h_2(\eta, \xi) \hat{g}_{1,k}, \end{aligned}$$

with

$$\hat{g}_{1,k} = \sum_{j=1}^{N/2} \int_{\frac{\pi(j-1)}{2N}}^{\frac{\pi j}{2N}} d\eta' h_1(\eta', \xi') h_2(\eta', \xi') \int_q dq \int_{q'} dq' (\hat{\mathbf{G}}_{ti}(\mathbf{r}_k, \mathbf{r}') \pm \hat{\mathbf{G}}_{ti}(\mathbf{r}_k, \mathbf{r}'_{image})) \cdot \hat{\mathbf{x}}_{fict,j}$$

$\hat{g}_{1,k}$ is a piecewise constant function. The + is used for the stokeslets in $\hat{\mathbf{z}}$ and the − for stokeslets in $\hat{\mathbf{x}}$ (only shear flow produces a torque on the spheroid). To obtain a better approximation to the torque, a fitted polynomial approximation to $\hat{g}_{1,k}$ is used, i.e.,

$$T_y \approx 2 \int_0^{\pi/2} h_1(\eta, \xi) h_2(\eta, \xi) g_1(\eta) d\eta,$$

where $g_1(\eta)$ is the fitted polynomial to $\hat{g}_{1,k}$. The following summarizes the steps of the torque calculation:

- *Step 1:*

  Using the known weightings in q', and the known dependencies of the torque stokeslets in q, integrate the torque stokeslets with respect to q' and with respect to q.

- *Step 2:*

  Compute a N by 1 matrix of torques using the torque stokeslets and image torque stokeslets. Each entry is G_{Tyjkl}, the y component of torque/η, in S_k due to a constant distribution of impulses along S_j, in the $\hat{\mathbf{x}}_l$ direction.

- *Step 3:*

  Using the known weightings, calculate the torque/η,

  $$T_y^k = G_{Tyjkl}\hat{a}_{jl}$$

- *Step 4:*

  Fit a polynomial in η to T_y^k,

  $$T_y^k \rightarrow T_y^\eta$$

- *Step 5:*

  Integrate T_y^η with respect to η,

  $$T_y = \int_0^{\frac{\pi}{2}} h_1(\eta) T_y^\eta d\eta$$

4.4.6 Results

We will now compare results of the BEMA to the exact solution. There are two main sources of errors in the BEMA— the piecewise constant approximation to the weightings and the numerical integration in η'. We chose to study a nearly spherical spheroid in uniform flow, since, for this case, $a_{x0}(\eta')$ and $a_{z1}(\eta')$ are nearly constant and we can focus on the size of the error due to numerical integration. We also describe the results for a thin prolate spheroid in shear flow, for which $a_{x0}(\eta')$ varies. For both cases, we will study the convergence of $\hat{a}_{x0}$ and $\hat{a}_{z1}$, examine U_y on the surface to verify that it converges to zero (U_y was not used to compute the weightings), and compare the BEMA results for fluid velocities, pressures and torques to those of the exact solution.

Results for a nearly spherical spheroid in uniform flow (Figure 4-3) Figure 4-4 illustrates the normalized stokeslet weightings $\hat{a}_{x0,n} = \hat{a}_{x0}/(\mu U_b)$ and $\hat{a}_{z1,n} = \hat{a}_{z1}/(\mu U_b)$ for a nearly spherical spheroid in uniform flow, with $N/2 = 8$ and $\epsilon = .001$, along the arc $q = 0$. We see that $\hat{a}_{x0,n}$ and $\hat{a}_{z1,n}$ are very nearly constant— $\hat{a}_{z1,n}$ is close to zero ($\approx 10^{-6}$) and $\hat{a}_{x0,n} \sim .0597/R$, where R is the radius of the sphere. (Note that although we have an exact solution for the pressure, velocities, and torque, we do not have an exact solution for the stokeslet weightings.) As we mentioned before, because the stokeslet weightings are nearly constant, the errors in the solution are primarily due to numerically integrating the Green's function in η' and are not due to approximating the weightings as constant in an element. This is made evident in Figure 4-5 which illustrates the normalized y velocity $U_{ny} = U_y/U_b$ on the surface along the arc, $q = \pi/4$, for $N/2 = 8$, for two integration criteria, $\epsilon = .005$ ($\cdot$) and $\epsilon = .001$ (+). This velocity should be zero. We see that the error decreases for the tighter integration criterion, with $|U_{ny}| < 6 \cdot 10^{-5}$ for $\epsilon = .005$ and $|U_{ny}| < 2 \cdot 10^{-5}$ for $\epsilon = .001$. Using the tighter criterion result in 50% more computational time.

Our results are compared with those of the exact solution for fluid velocities along an arc, $\xi = 6$ (or $r = 2.7R$), $q = \pi/4$, in Figure 4-6. The solutions match to one part in ten thousand which is the same as the results for fluid velocities along the surface

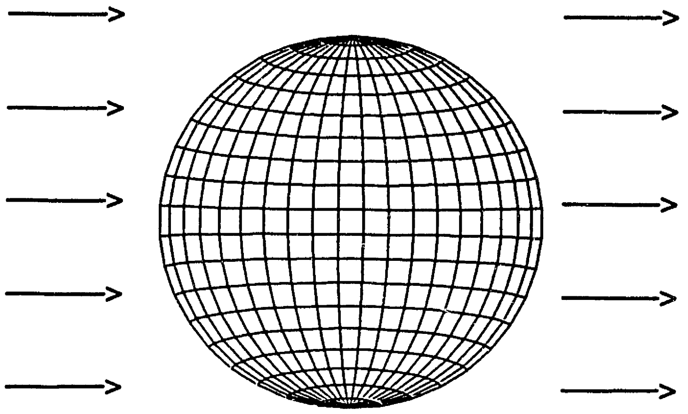

Figure 4-3: A nearly spherical spheroid ($\xi_o = 5$) in uniform flow. The arrows indicate the magnitude and direction of the flow.

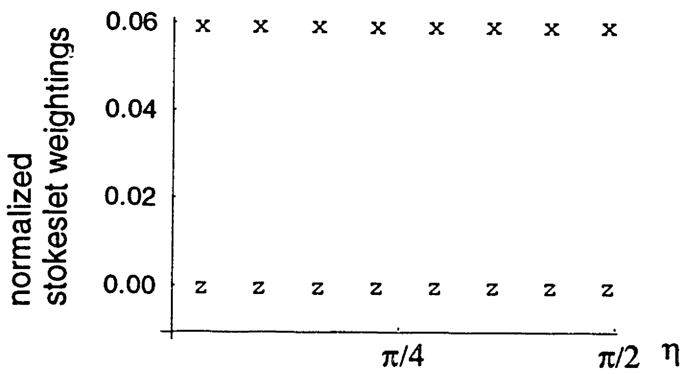

Figure 4-4: The normalized stokeslet weightings for $N/2 = 8$ with $\epsilon = .001$ for a nearly spherical spheroid ($\xi_o = 5$) in uniform flow, along the arc, $q = 0$. $\hat{a}_{x0,n}$ is denoted by x and $\hat{a}_{z1,n}$ is denoted by z.

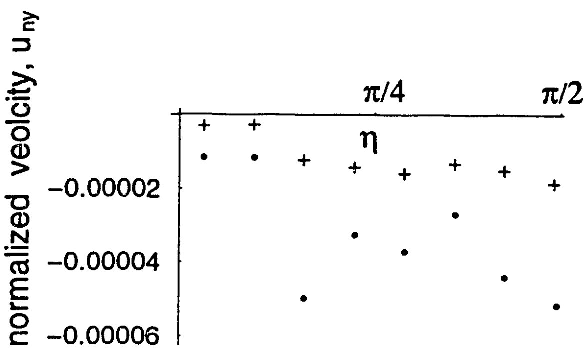

Figure 4-5: The normalized velocity, U_{ny} on the surface along the arc, $q = \pi/4$ for $\epsilon = .005$ $(\cdot)$ and $\epsilon = .001$ $(+)$ with $N/2 = 8$.

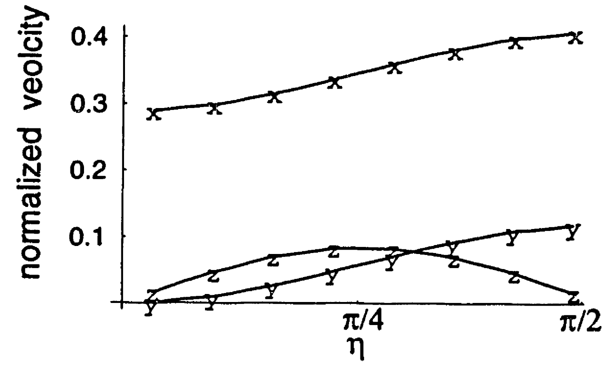

Figure 4-6: The fluid velocities along an arc in the fluid, $\xi = 6$ (or $r = 2.7R$), $q = \pi/4$ calculated with BEMA with $N/2 = 8$ and $\epsilon = .001$ (denoted by the symbols x for U_{nx}, y for U_{ny}, z for U_{nz}) and calculated with the analytic solution (solid line).

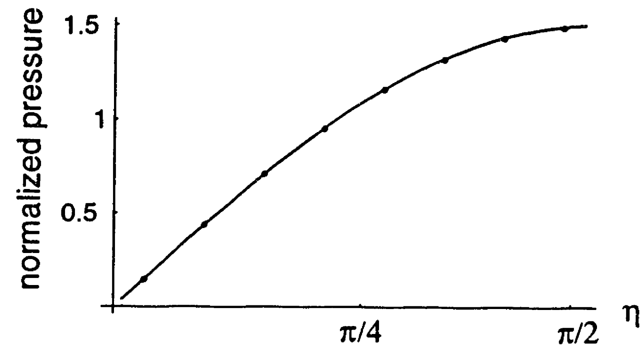

Figure 4-7: The normalized pressure, $P/(\mu U_b)$ on the surface ($\xi = 5.005$ or $r = 1.005R$) along the arc, $q = 0$ calculated with BEMA ($\cdot$) and with the analytic solution (solid line).

(Figure 4-5).

The Green's function for pressure contains a non-integrable singularity on the surface, and we use the pressure for points close to the surface, ($\xi = 5.005$ or $r = 1.005R$) to approximate the pressure on the surface. Figure 4-7 indicates the numerical results for normalized pressure, $P/(\mu U_b)$, next to the surface along the arc, $q = 0$.

Approximating the pressure of points on the surface with the pressure of points

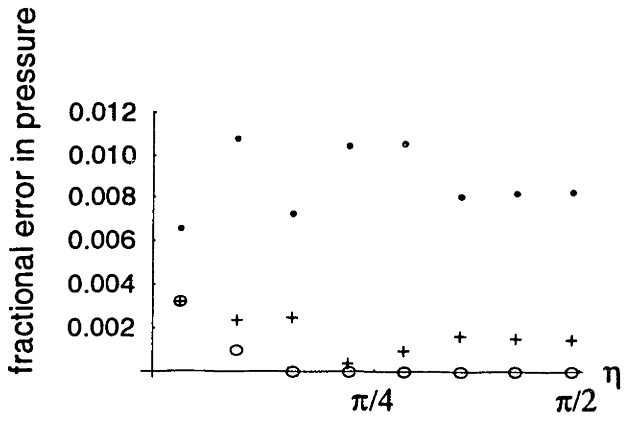

Figure 4-8: The fractional difference between the the numerical solution for pressure at $\xi = 5.005$ and the analytic solution at $\xi = \xi_o = 5$ with $\epsilon = .005$ ($\cdot$), and the difference between the the numerical solution and the analytic solution at $\xi = 5.005$ with $\epsilon = .005$ (+) and with $\epsilon = 10^{-5}$ (o).

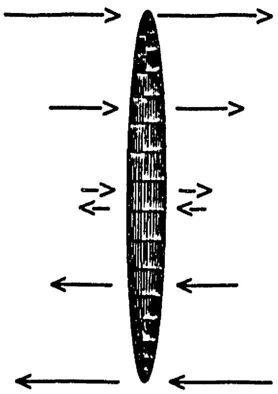

Figure 4-9: A thin, prolate spheroid ($\xi_o = .1$) in shear flow. The arrows indicate the magnitude and direction of the flow.

close to the surface is an additional source of error. To examine the magnitude of this error, we studied the difference between the numerical solution calculated along the contour, $\xi = 5.005$ and the exact solution calculated along two different contours:

1. the surface contour, $\xi = \xi_o = 5$,
2. the contour, $\xi = 5.005$.

We chose $\epsilon = .005$ for the the first case, and for the second case, we chose $\epsilon = .005$, and $\epsilon = 10^{-5}$ (Figure 4-8). By varying the contour, and by varying ϵ, we can see how the approximations contribute to the error. From Figure 4-8 we see that the error from approximating the pressure on the surface $\xi = \xi_o = 5$ with the pressure off the surface ($\xi = 5.005$) is much larger than the error due to numerical integration.

We cannot study torque for this example since, from symmetry, there is no torque in uniform flow.

Results for a thin, prolate spheroid in shear flow (Figure 4-9) The normalized stokeslet weightings $\hat{a}_{x0,n} = \hat{a}_{x0}/(\mu\Omega)$ and $\hat{a}_{z1,n} = \hat{a}_{z1}/(\mu\Omega)$ for a thin, prolate spheroid ($\xi_o = .1$) in shear flow are illustrated in Figure 4-10, with $N/2 = 16$ and $\epsilon = .005$. We see that $\hat{a}_{z1,n}$ is nearly zero for all η and $\hat{a}_{x0,n}$ monotonically decreases with η.

Figure 4-11 indicates U_{ny} on the surface contour $q = \pi/4$ for $N/2 = 8$ and $N/2 = 16$. We see that the error is two orders of magnitude larger than that of the translating, nearly spherical spheroid, with a nearly constant $\hat{a}_{x0,n}$. We also observe that the

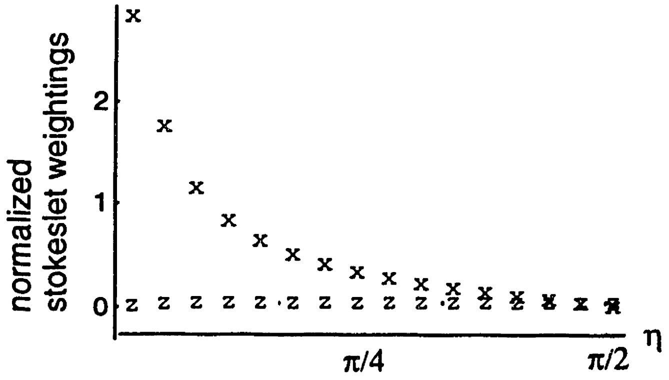

Figure 4-10: The normalized stokeslet weightings for a thin, prolate spheroid ($\xi_o = .1$) with $N/2 = 16$ and $\epsilon = .005$. $\hat{a}_{x0,n}$ is denoted by x and $\hat{a}_{z1,n}$ is denoted by z.

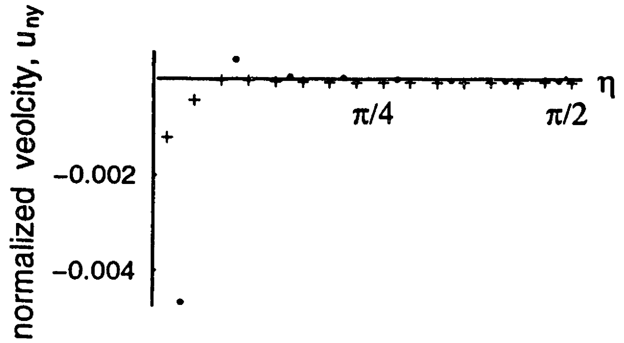

Figure 4-11: U_{ny} along the surface of thin prolate spheroid ($\xi_o = .1$) in shear flow with $q = \pi/4$ for $N/2 = 8$ ($\cdot$) and $N/2 = 16$ (+) with $\epsilon = .005$.

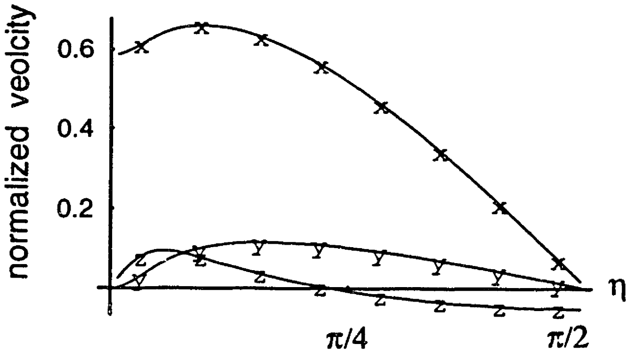

Figure 4-12: U_{nx}, U_{ny}, and U_{nz} for points in the fluid ($\xi = .2$, $q = \pi/4$), calculated with BEMA ($N/2 = 8$ and $\epsilon = .005$). The exact solution is indicated by the solid lines.

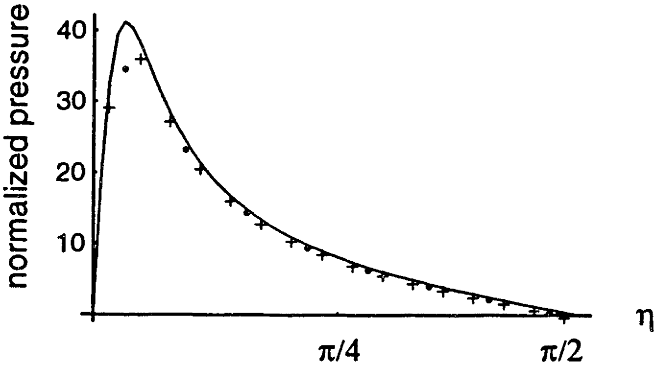

Figure 4-13: The normalized pressure next to the surface ($\xi_o = .1005$, $q = 0$) calculated with BEMA ($\epsilon = .005$, $N/2 = 8$ ($\cdot$), and $N/2 = 16$ (+)). The exact solution is indicated by the solid lines.

maximum error for $N/2 = 16$ is approximately half that for $N/2 = 8$. Therefore we conclude that the the piecewise constant approximation of the stokeslet weighting $\hat{a}_{x0}$ is the main source of error.

Figure 4-12 compares our results ($N/2 = 8$) with the exact solution for fluid velocities along the arc $\xi = .2$, $q = \pi/4$. The results match to one part in a thousand.

Figure 4-13 compares the pressure next to the surface ($\xi_o = .1005$) for $q = 0$, $N/2 = 8$ and $N/2 = 16$ with the exact solution on the surface. The largest errors occur where the pressure is rapidly varying with η and the piecewise constant approximation of the weightings with $N/2 = 8$ or $N/2 = 16$ cannot accurately sample the variation. Increasing $N/2$ to 16 results in a decrease in the largest error by a factor of three.

analytic	*numeric*	$N/2$	ξ	ξ_o
-12.57	-12.77	4	5.01	5
-12.57	-12.52	8	5.01	5
-12.57	-12.42	16	5.01	5
-12.57	-12.56	32	5.01	5
-12.57	-12.55	64	5.01	5
-12.57	-12.56	8	6.00	5
-10.18	-10.11	8	1.01	1
-10.18	-10.17	8	2.00	1
-7.18	-7.15	8	.60	.50
-7.18	-7.18	16	.60	.50
-7.18	-7.18	32	.60	.50
-3.33	-3.33	8	1.00	.1

Table 4.1: A table of results for the normalized torque, $T_{ny} = T_y/(\mu\Omega)$, calculated for spheroids with different ξ_o. The torque is calculated on different surfaces surrounding the spheroid (the surfaces are denoted by ξ), for different discretizations ($N/2$).

4.4.7 The torque for full spheroids in shear flow for different shapes

To understand the sources of error in our torque calculation, we computed the normalized torque $T_y/(\mu\Omega)$ for different shapes (Figure 4-14) and compared our results to those of the exact solution (Table 4.4.7). We also verified our code by checking that the torque on different surfaces surrounding the spheroid is the same — this implies that the torque induced by the fluid is zero and that Stokes equation is satisfied. The spheroid is denoted by a surface of constant ξ_o, and the different surrounding surfaces are denoted by ξ.

Three features are evident— the error is small (maximum error is 1.6% for $N/2 = 4$), the error decreases with the distance between the surrounding surface and the spheroidal surface, and the error decreases (although not monotonically) with increasing N. The decrease with N is to be expected—the piecewise constant approximation improves with increasing N; that the decrease is not monotonic may be because there is an additional source of error in the torque calculation coming from the polynomial fit approximation. The decrease in error with distance can be

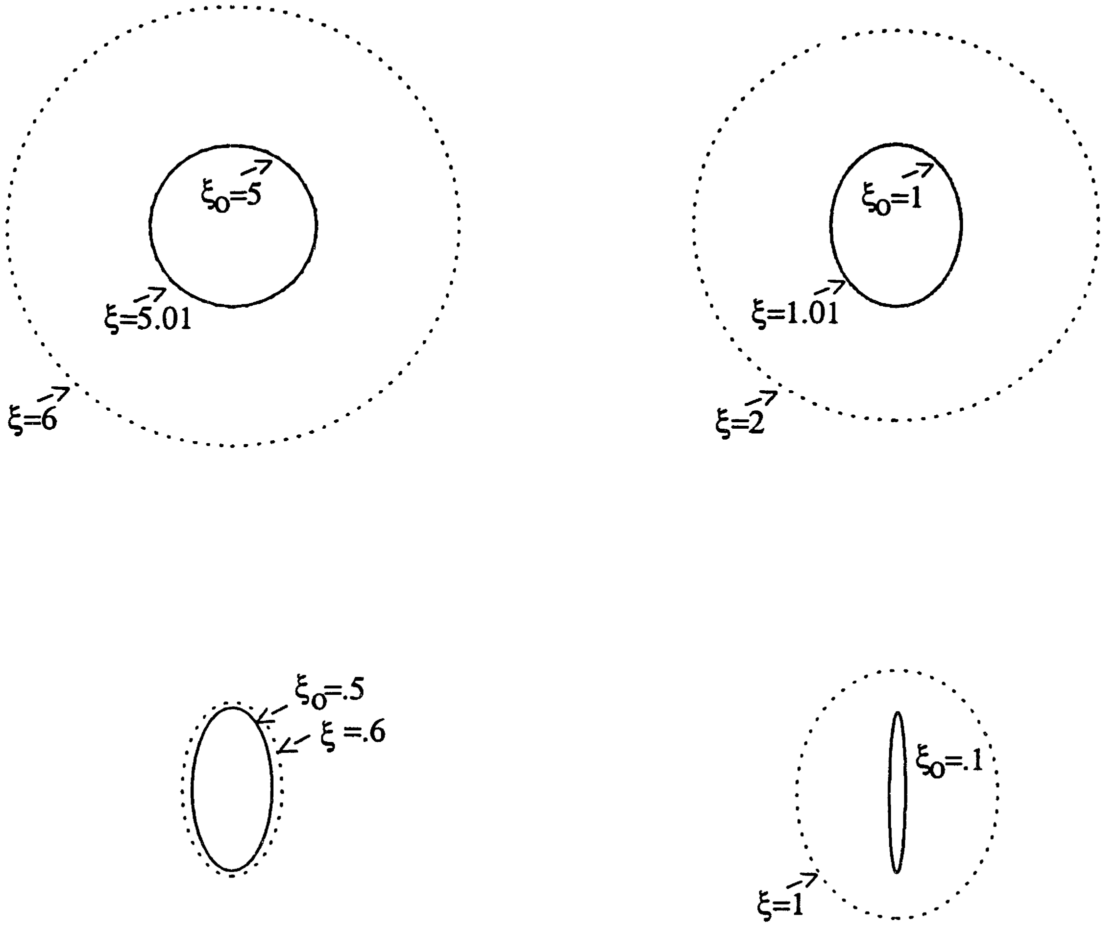

Figure 4-14: The spheroids for which the torque was calculated (solid lines) along with the enclosing surfaces (dashed lines) used in the calculation.

understood—as the distance from the surface of the spheroid increases, the distance from the non-integrable singularities increase, and the numerical integration can be performed more accurately.

4.4.8 Conclusion

We have shown that our results for full spheroids appear to converge to the exact results as $N \to \infty$ and as $\epsilon \to 0$, and that the primary source of error, when the weightings of the stokeslets vary, is the piecewise constant approximation. For the thin, prolate spheroid, if we double the number of elements, we halve the magnitude of the error. When the stokeslet weightings are nearly constant, if we tighten the numerical integration criterion by a factor of five, we reduce the error by about a factor of three.

In the next section, we will describe the BEMA applied to the model of the hair bundle structure, the hemispheroid with a plate, in the limit of low frequencies. We will see that the methods are similar, and that this exercise in using BEMA to calculate the hydrodynamics for full spheroids has checked much of the method for the hemispheroid with a plate.

4.5 Low-frequency solution for hemispheroid with a plate

We now discuss the method to compute the low-frequency solution for the hemispheroid hinged to a plate for both translational motion and rotational motion. We will first describe the equations of motion and the boundary conditions in the limit of low frequencies. Next, we will describe the method used to solve the equations of motion. We will then discuss results obtained for three hemispheroidal shapes that represent extrema of the shapes considered in this study—a very thin prolate hemispheroid ($\xi_o = .1$), a wide, flat oblate hemispheroid ($\xi_o = .1$), and a nearly hemispherical hemispheroid ($\xi_o = 5$).

4.5.1 Low frequency analysis

In Section 2.1.5 we showed for low frequencies instead of solving the Navier-Stokes equation, we can solve the simpler Stokes equation. We simplified the Navier-Stokes equation by expanding the hydrodynamic variables and the boundary conditions in terms of powers of $j\omega$. By equating like powers of $j\omega$, we showed that steady equations of motion can be solved which are independent of $j\omega$. We determined that only the first order terms were significant to motion of the hemispheroid. The equations of motion and boundary conditions are given in Equations 2.10-2.13 for translational motion and in Equations 2.16-2.19 for rotational motion.

Frame of reference for translational motion

For translational motion, the distant boundary condition is non-zero. To simplify the analysis, we will choose a frame of reference for which the distant boundary condition is zero. The advantage of this frame of reference is that a stokeslet, whose velocity approaches zero as $\xi \to \infty$, can be used in the BEMA. Let $\mathbf{U}_{1t}(\mathbf{r})$ represent the velocity in this frame of reference,

$$\mathbf{U}_{1t}(\mathbf{r}) = \mathbf{U}_1(\mathbf{r}) + zU_b\hat{\mathbf{x}}.$$

For this frame of reference, the equations of motion remain the same while the boundary conditions can be expressed as,

$$\mathbf{U_{1t}}(\xi = \xi_\mathbf{o}, \eta, \mathbf{q}) = zU_b\hat{\mathbf{x}}, \tag{4.23}$$

$$\mathbf{U_{1t}}(\xi, \eta = \pi/\mathbf{2}, \mathbf{q}) = 0, \tag{4.24}$$

$$\mathbf{U_{1t}}(\xi \to \infty, \eta, \mathbf{q}) = 0. \tag{4.25}$$

Since

$$\mu\nabla^2(zU_b\hat{\mathbf{x}}) = 0,$$

the pressure is the same in either frame of reference, i. e.,

$$P_{1t}(\mathbf{r}) = P_1(\mathbf{r}).$$

Since

$$\mathbf{T} = \int_S (\mathbf{r} \times (\mu\nabla(\hat{n} \cdot zU_b\hat{\mathbf{x}})) + \mu(\hat{n} \cdot \nabla)zU_b\hat{\mathbf{x}}))dS = 0, \tag{4.26}$$

the torque remains the same. (See appendix of this chapter for the derivation of Equation 4.26.)

4.5.2 Boundary condition at plate

The problem of a hemispheroid with a plate is similar in many ways to the problem of a full spheroid. It has the same rotational symmetry, and the motion of the body is solely in the x-z plane. We therefore know the q dependence of the stokeslet weightings (see Section 4.3.1). The main difference in applying the BEMA to a hemispheroid with a plate is satisfying the boundary condition along the infinite plate. We could discretize a contour along the plate in addition to the contour along the hemispheroid, and find the stokeslet weightings that would satisfy the boundary conditions, but the computational domain must be finite. Therefore we would need to introduce artificial boundaries in the fluid at some distance away from the hemispheroid, but the use of artificial boundaries would introduce errors. An alternate method, and what we chose to do, is to use a Green's function that has the correct boundary conditions along the plate.

4.5.3 The Green's function for a stokeslet with a plate

The j^{th} component of the Green's function for velocity due to a stokeslet in the k^{th} direction in the presence of a plate can be expressed as (Blake, 1971)

$$G^k_{u,plate,j}(\mathbf{r},\mathbf{r}') = G^k_{u,j}(\mathbf{r},\mathbf{r}') - G^k_{u,j}(\mathbf{r},\mathbf{r}'_{image}) + G^k_{uw,j}(\mathbf{r},\mathbf{r}'_{image}), \tag{4.27}$$

where $G^k_{u,j}(\mathbf{r})$ is the j^{th} component of velocity due to a stokeslet in the k^{th} direction with no plate present, $r'_{image} = x'\hat{\mathbf{x}} + y'\hat{\mathbf{y}} - z'\hat{\mathbf{z}}$, and $G^k_{uw,j}(\mathbf{r},\mathbf{r}'_{image})$ satisfies Stokes equation, and has the necessary velocity along the plate to ensure that $G^k_{u,plate,j}(\mathbf{r},\mathbf{r}')$ equals zero along the plate. $G^k_{uw,j}(\mathbf{r},\mathbf{r}'_{image})$ can be expressed as

$$\begin{aligned} G^k_{uw,j}(\mathbf{r},\mathbf{r}'_{image}) &= \frac{1}{4\pi\mu} z'(\delta_{k\alpha}\delta_{\alpha l} - \delta_{k3}\delta_{3l}) \frac{\partial}{\partial(x_l - x'_{l,image})} \\ &\quad \left[\frac{z'(x_j - x'_{j,image})}{|\mathbf{r} - \mathbf{r}'_{image}|^3} - \left(\frac{\delta_{j3}}{|\mathbf{r} - \mathbf{r}'_{image}|} + \frac{(x_j - x'_{j,image})(z+z')}{|\mathbf{r} - \mathbf{r}'_{image}|^3}\right)\right]. \end{aligned}$$

The Green's function for pressure due to a stokeslet in the k^{th} direction in the presence of a plate can be expressed as

$$G^k_{p,plate}(\mathbf{r},\mathbf{r}') = G^k_p(\mathbf{r},\mathbf{r}') - G^k_p(\mathbf{r},\mathbf{r}'_{image}) + G^k_{pw}(\mathbf{r},\mathbf{r}'_{image}), \tag{4.28}$$

where $G^k_p(\mathbf{r})$ is the pressure due to a stokeslet in the k^{th} direction with no plate present, and, $G^k_{pw}(\mathbf{r},\mathbf{r}'_{image})$ accounts for the presence of the plate,

$$G^k_{pw}(\mathbf{r},\mathbf{r}'_{image}) = \frac{-z'}{2\pi}(\delta_{k\alpha}\delta_{\alpha l} - \delta_{k3}\delta_{3l}) \frac{\partial}{\partial(x_l - x'_{l,image})} \frac{z+z'}{|\mathbf{r} - \mathbf{r}'_{image}|^3}.$$

These Green's functions are mathematically equivalent to a stokes doublet and source doublet in the image plane (Blake, 1971) and for simplicity we will label these Green's functions as the "w" sources.

4.5.4 BEMA for hemispheroid with a plate

For the full spheroid, we represented the hydrodynamics as a weighted integral of stokeslets. For the hemispheroid with a plate, we will represent the hydrodynamics as a weighted integral of the vector sum of a stokeslet, an image stokeslet and a "w" source. We will refer to this sum of a stokeslet, an image stokeslet and a "w" source as the "source" for the hemispheroid with a plate.

As we mentioned, the q dependence of the weightings are already known. To obtain the source weightings in η, a similar procedure to the one outlined for the full spheroid is used except that

1. We have "w" sources in addition to the stokeslet and image stokeslet.
2. Instead of using two of the three boundary conditions to obtain the weightings, three are needed because $a_{x2}(\eta)$ is no longer zero.

Since the procedure for the hemispheroid is similar to that of the full spheriod, we will continue using the same notation so that $N/2$ is the total number of discretization elements.

The following summarizes the steps of the BEMA applied to the hemispheroid with a plate:

- *Step 1:*

  Using the known weightings in q', integrate the Green's functions with respect to q'.

- *Step 2:*

  Break contour of constant q' into $N/2$ elements, the j^{th} element has length S_j.

- *Step 3:*

  Compute a $3N/2$ by $3N/2$ matrix of fluid velocities using the stokeslets, image stokeslets and "w" sources. Each entry is G_{uijkl}, the fluid velocity in the $\hat{\mathbf{x}}_i$ direction, at $\mathbf{r}_k$, due to a constant distribution of sources along S_j, in the $\hat{\mathbf{x}}_l$ direction.

- *Step 4:*

  Solve a system of $3N/2$ equations,

$$U_{surf,i}(\mathbf{r}_k) = G_{uijkl}\hat{a}_{jl},$$

  for the $3N/2$ unknowns, $\hat{a}_{jl}$ with $\hat{a}_{j1} = \hat{a}_{x0,j}$, $\hat{a}_{j2} = \hat{a}_{x2,j} = \hat{a}_{y2,j}$, $\hat{a}_{j3} = \hat{a}_{z1,j}$.

- *Step 5:*

  Compute entries for matrices $G_{uijl}(\mathbf{r})$, (a $3N/2$ by 3 matrix), $G_{pjl}(\mathbf{r})$, (a $3N/2$ by 1 matrix), and $G_{Tyjl}(\mathbf{r})$ (an $3N/2$ by 1 matrix) using stokeslets, image stokeslets and "w" sources.

  Compute velocity, pressure, and torque using $\hat{a}_{jl}$,

$$\begin{aligned}
U_i(\mathbf{r}) &= G_{uijl}(\mathbf{r})\hat{a}_{jl} \\
P(\mathbf{r}) &= G_{pjl}(\mathbf{r})\hat{a}_{jl} \\
T_y &= G_{Tyjl}\hat{a}_{jl}
\end{aligned}$$

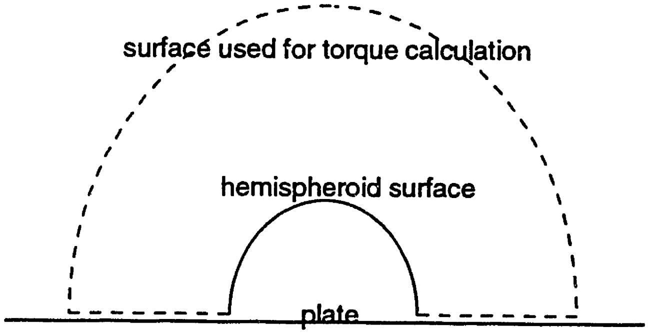

Figure 4-15: The torque on the surface indicated by the dashed lines is equal to the negative of the torque on the hemispheroid. The solid line indicates the hemispheroid.

4.5.5 The torque calculation for a hemispheroid with a plate

Because of the presence of the infinite plate, we can not use a surface surrounding the sources to calculate the torque. However, we can calculate the torque by integrating over the surface indicated by the dashed lines in Figure 4-15 because the torque induced by the fluid on the surface described by the hemispheroid and the dashed lines is equal to zero. Therefore, the torque along the dashed lines is equal to the negative of the torque induced by the fluid on the hemispheroid.

4.5.6 Method checks

When we applied the BEMA to a full spheroid, we were able to check our method by comparing the results to those of the known solution. Since there is no known solution for the hemispheroid on a plate (if there were, then there would be no need to use BEMA) we performed tests of the method at different steps. The following lists the tests used:

1. We check that the Green's functions, after integrating with respect to q', satisfy Stokes' equation and conservation of mass.

2. We check that the Green's functions, after integrating with respect to η', satisfy Stokes equation.

3. We check that the torque on an enclosed surface in the fluid is equal to zero. This is true if Stokes equation is satisfied.

Assuming the fluid velocities satisfy the boundary conditions, our results are only valid if Stokes' equation and the conservation of mass equation are also satisfied. If the Green's functions satisfy these equations, then we can be sure that our results of the BEMA for fluid velocity and pressure are correct since our results are simply weighted sums of these Green's functions.

Check Green's function after q' integration

The integrals of the Green's functions for velocity and pressure with respect to q' were substituted into the conservation of mass equation and Stokes equation to check that the integrals were done correctly and that equations are still satisfied. This was done with Mathematica which can easily do vector Laplacians and gradients in spheroidal coordinates. Unfortunately, the resulting equations were too complicated to simplify, so we substituted numerical values for a few randomly chosen positions of sources points and field points for two different hemispheroidal shapes. We found for conservation of mass,

$$|\nabla \cdot \tilde{\mathbf{G}}_{u,i}| < 10^{-14} |\tilde{\mathbf{G}}_{u,i}|,$$

and for Stokes equation,

$$|\nabla \tilde{G}_{p,i} - \mu \nabla^2 \tilde{\mathbf{G}}_{u,i}| < 10^{-12} |\nabla \tilde{G}_{p,i}|,$$

for each point tested. $\tilde{G}_{p,i}$ and $\tilde{\mathbf{G}}_{u,i}$ represent the integrated Greens function for pressure and velocity due to a source in the $\hat{\imath}$ direction. Since the error is at the level of the machine precision, we conclude that the integration with respect to q' was performed correctly.

Check Green's function after η' integration

To check that the numerical integration in η' was done correctly, we substituted into a numerical approximation of Stokes equation, the results of the numerical integration of the Green's functions with respect to $d\eta'$ for the eight segments (N/2=8) illustrated in Figure 4-16. The field point chosen is $\xi = 5.015$, $\eta = .937\pi/2$, $q = \pi/4$ and the shape

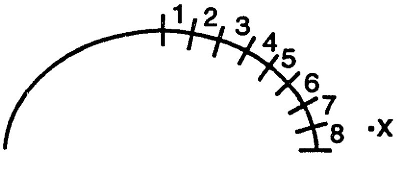

Figure 4-16: The eight segments along the surface over which the integration with respect to η' was performed. The "x" delineates the field point.

of hemispheroid is nearly hemispherical with $\xi_o = 5$. Centered difference equations were used to approximate the derivatives in Stokes equation. The segments are labeled 1-8, with 1 representing the segment at the tip of the hemispheroid and 8 representing the segment closest to the plate. The field point is marked with an "x". For segments 1-7, the integrated Green's functions come close (within 5%) to satisfying Stokes equation. For the eighth segment, we cannot determine whether Stokes equation is satisfied because we cannot accurately estimate the derivative with the difference approximations— there is a large change in the Laplacian and the gradient when the spacing used in the difference calculations is changed. Since Stokes equation is fairly well satisfied (the derivatives were approximated by finite differences—a somewhat crude approximation that was not used anywhere in the BEMA) for the segments where fairly accurate estimates of the derivatives are obtained, we conclude that the numerical integrations with respect to η' are correct.

4.5.7 Check that the torque on a surface that encloses only fluid is zero

If Stokes equation is satisfied, then the torque on a surface that encloses only fluid must be zero. To test that this was so, we performed the following calculation. We computed the torque along three different surfaces indicated by the dashed curves in Figure 4-17. The indicated surfaces, along with the surface of the hemispheroid, encloses only fluid. Therefore the total torque computed along the surfaces is zero. This implies that the torque calculated for the surfaces indicated by the dashed curves must be equal to the negative of the torque calculated along the surface of the hemispheroid. We checked that the torque computed for several different surfaces in the fluid remains the same. Figure 4-17 illustrates the enclosing surfaces as well as the

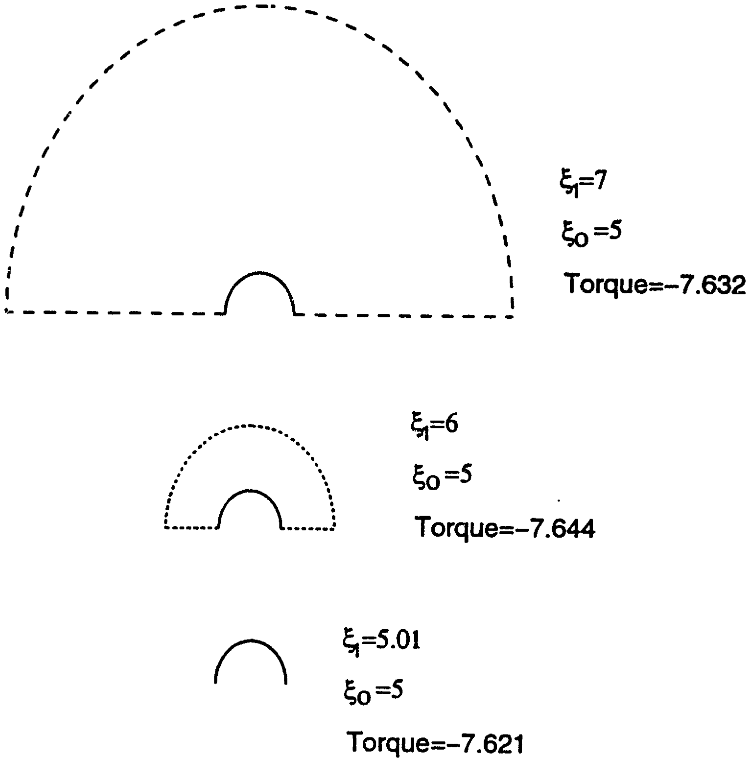

Figure 4-17: The dashed lines indicate $\xi = \xi_1$, the surfaces for which the torque was computed. The solid line indicates the surface of the hemispheroid, $\xi = \xi_o = 5$. The sum of the torques computed for surfaces indicated by solid and dashed lines is zero since the surfaces enclose fluid. Three different surfaces in the fluid were chosen. The torque for the three dashed surfaces must be the same and must be equal to the negative of the torque for the hemispheroidal surface.

torques for a nearly hemispherical shape. We see that the difference in torque is less than .3%. The errors derive from the discretization and the polynomial fit used in the torque calulation (see Section 4.4.5).

Table 4.5.7 illustrates the results for Figure 4-17 as well as the results for a thin, prolate hemispheroid, $\xi_o = .5$. For the thin, prolate hemispheroid, the differences were less than .1%.

torque	$N_1/2$	$N_2/2$	ξ	ξ_o
-7.621	8	8	5.01	5
-7.644	8	100	6.00	5
-7.626	8	100	7.00	5
-7.632	8	200	7.00	5
-4.050	16	8	.501	.5
-4.053	16	25	.60	.5
-4.053	16	50	.70	.5

Table 4.2: The torque computed along surfaces for different hemispheroid shapes. $N_1/2$ denotes the number of elements along the hemispheroidal contour. $N_2/2$ are the number of elements used along the plate. A polynomial fit of the torque/η was used to perform the integration along the contours.

4.6 Validation of low frequency solution for hemispheroid on a plate

In this section, we will describe the results—the source weightings, the error in surface velocity, the pressure along the surface, and the torque for hemispheroids of three different shapes that represent the extremum of hemispheroidal shapes—a nearly hemispherical hemispheroid (top panel of Figure 4-18), a thin, prolate hemispheroid (middle panel of Figure 4-18), and a wide, flat, oblate hemispheroid (lower panel of Figure 4-18).

4.6.1 Translational motion—a nearly hemispherical hemispheroid

The results for a nearly hemispherical hemispheroid (top panel of Figure 4-18) in translational motion are illustrated in the top panels of Figure 4-19–Figure 4-22. The normalized source weightings, $\hat{a}_{x0,n} = \hat{a}_{x0}/(\mu U_b)$, $\hat{a}_{z1,n} = \hat{a}_{z1}/(\mu U_b)$, and $\hat{a}_{x2,n} = \hat{a}_{x2}/(\mu U_b)$, are illustrated in the top panels of Figure 4-19. We see that the weightings appear to converge to their final values for small $N/2$— the weightings for $N/2 = 4$ are within 5% of the weightings for $N/2 = 32$.

We looked at normalized fluid velocity, $\mathbf{U}_{1tn}(\mathbf{r}) = \mathbf{U}_{1t}(\mathbf{r})/U_b$, at field points off the collocation points along the surface and compared these velocities to the boundary velocities. The field points were located at $\eta = \eta_{bc} + \pi/(4N)$, and $q = \pi/4$ where η_{bc} represents collocation points (Figure 4-20). The errors in fluid velocity as a function of η are shown in the top panels of Figure 4-21. The smallest error occurs where variations of the weightings with η are smallest. This makes sense — when the source weightings aren't changing rapidly with η, the approximation of a piecewise constant source weightings is better. The error decreases as a function of N and even for $N/2 = 4$, the error is small ($< .009$). The top left panel of Figure 4-22 indicates the error as a function of N for $\eta = \pi/4$. Evidently, the error decreases as $1/N^a$ where $2 < a < 3$.

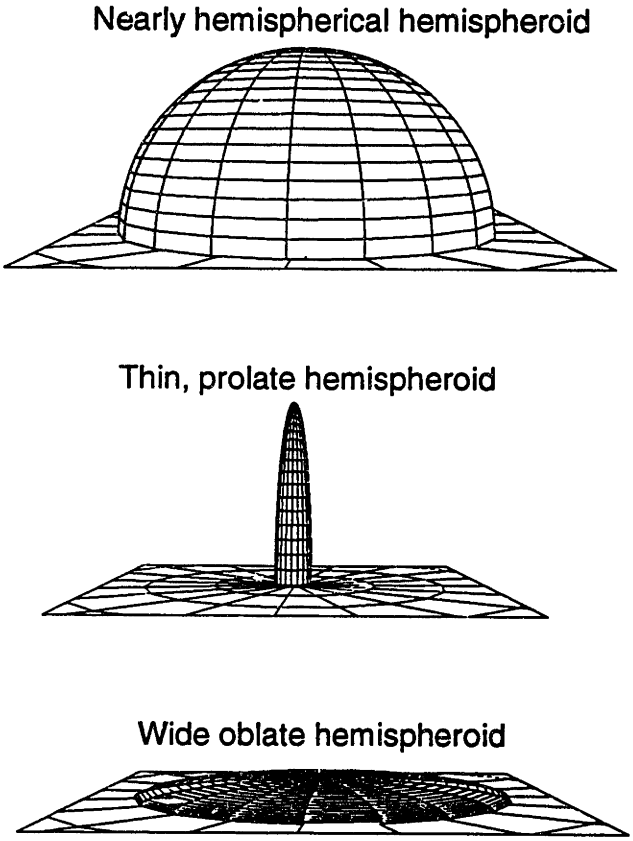

Nearly hemispherical hemispheroid

Thin, prolate hemispheroid

Wide oblate hemispheroid

Figure 4-18: Top: A nearly hemispherical hemispheroid with $\xi_o = 5$. Middle: A thin, prolate hemispheroid with $\xi_o = .1$. Lower: A wide, oblate hemispheroid with $\xi_o = .1$.

The normalized pressure, $P_n(\mathbf{r}) = P(\mathbf{r})/(\mu U_b)$ is illustrated in the top middle panel of Figure 4-22. Also shown is the exact solution for the pressure along the surface of a full spheroid with no plate present. For most of the points indicated, except for the few that are close to the plate, the pressures are nearly identical. Close to the plate, the pressure for the hemispheroid with a plate is larger than that of a corresponding point on the full spheroid. Farther away from the surface, the difference in pressure becomes even greater (not shown). This makes sense. First of all, the symmetry of the geometry of the full spheroid about the equatorial plane, and the antisymmetry of the surface velocities about this plane, force the pressure in this plane to be zero. For the hemispheroid with a plate, these conditions do not exist, and the pressure is not zero at $\eta = \pi/2$. Secondly, for points close to the surface and far from the plate, the conditions of the two problems are similar. Close to the plate, the problems are no longer similar. The plate restricts the motion of the fluid, and causes the pressure to be larger than the corresponding points in the fluid for a full spheroid without a plate. Similarly, farther from the hemispheroid, the plate's influence is larger and therefore the pressure is larger than that of the full spheroid.

The normalized torque, $T_{y,n} = T_y/(\mu U_b)$ as a function of N is illustrated in the top right panel of Figure 4-22. The torque calculation has nearly converged to its final result for $N/2 = 4$—the difference in the torque calculated for $N/2 = 4$ and the torque calculated for $N/2 = 32$ is less than 1%.

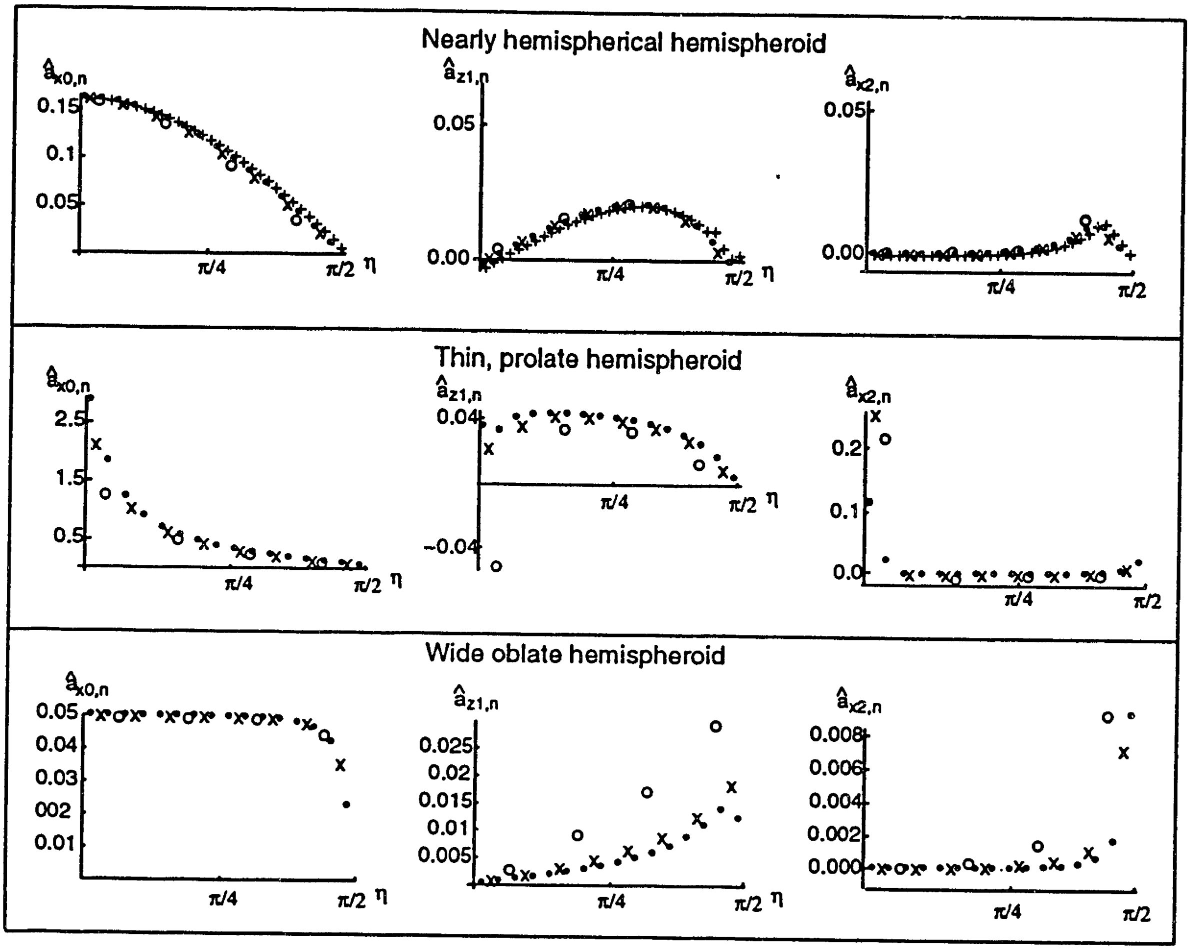

Figure 4-19: The normalized source weightings, $\hat{a}_{x0,n} = \hat{a}_{x0}/(\mu U_b)$, $\hat{a}_{z1,n} = \hat{a}_{z1}/(\mu U_b)$ and $\hat{a}_{x2,n} = \hat{a}_{x2}/(\mu U_b)$, for a nearly hemispherical hemispheroid, $\xi_o = 5$ (top), a thin prolate hemispheroid, $\xi_o = .1$ (middle), and a wide, oblate hemispheroid, $\xi_o = .1$ (bottom) for translational motion. The data are represented by the following symbols: o for $N/2 = 4$; x for $N/2 = 8$; • for $N/2 = 16$; and + for $N/2 = 32$. Note the change in scales for each plot.

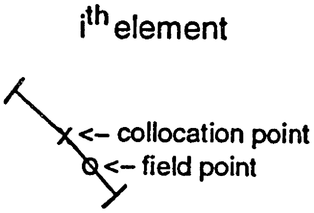

Figure 4-20: The collocation point, and the field point used to check the fluid velocities, of an element. The field point is $\pi/(4N)$ away from the collocation point.

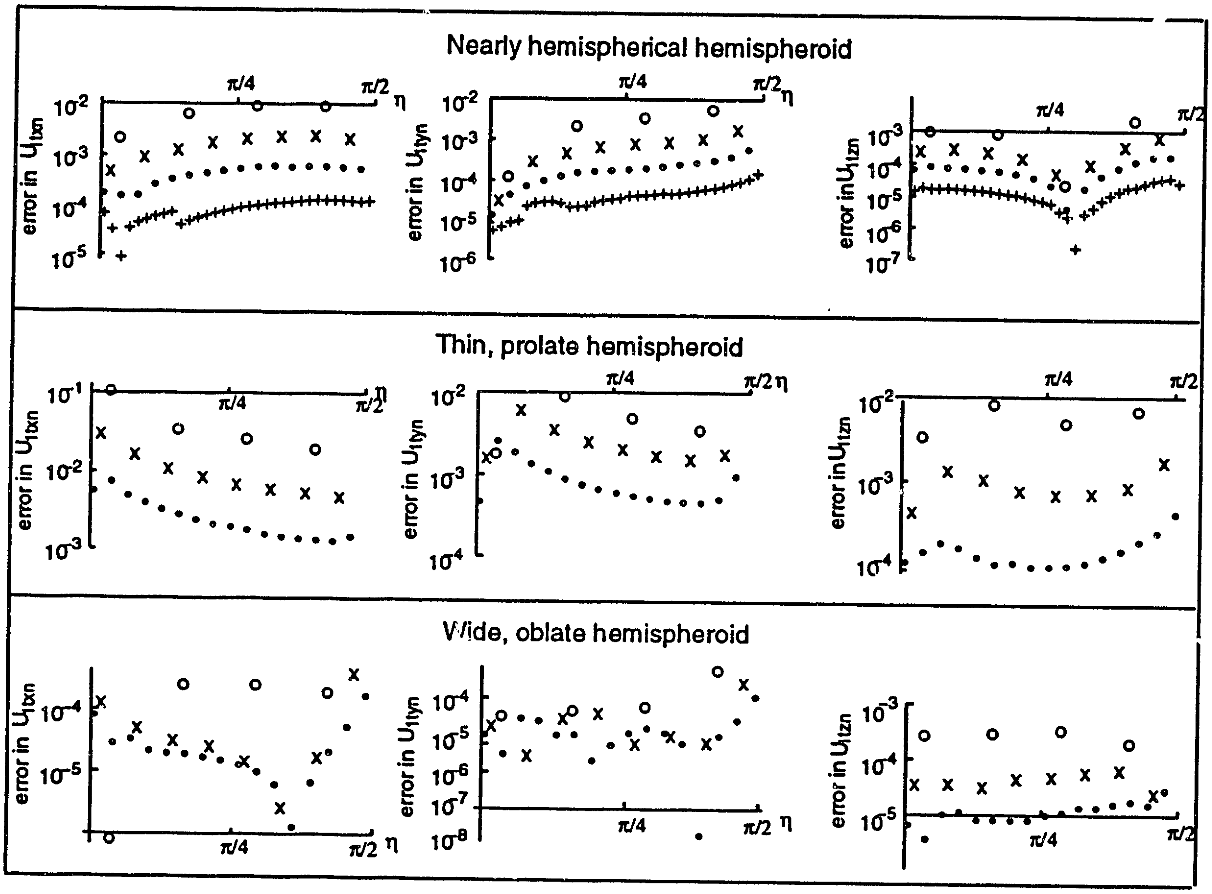

Nearly hemispherical hemispheroid

Thin, prolate hemispheroid

Wide, oblate hemispheroid

Figure 4-21: The magnitude of the difference between the normalized velocity at a field point (Figure 4-20) and the normalized velocity at a collocation point along the arc $q = \pi/4$ for a nearly hemispherical hemispheroid, $\xi_o = 5$ (top), a thin prolate hemispheroid, $\xi_o = .1$ (middle), and a wide, oblate hemispheroid, $\xi_o = .1$ (bottom) for translational motion. The data are represented by the following symbols: o for $N/2 = 4$;x for $N/2 = 8$; • for $N/2 = 16$; + for $N/2 = 32$; – for $N/2 = 64$; and = for $N/2 = 128$. Note the change in scales for each plot.

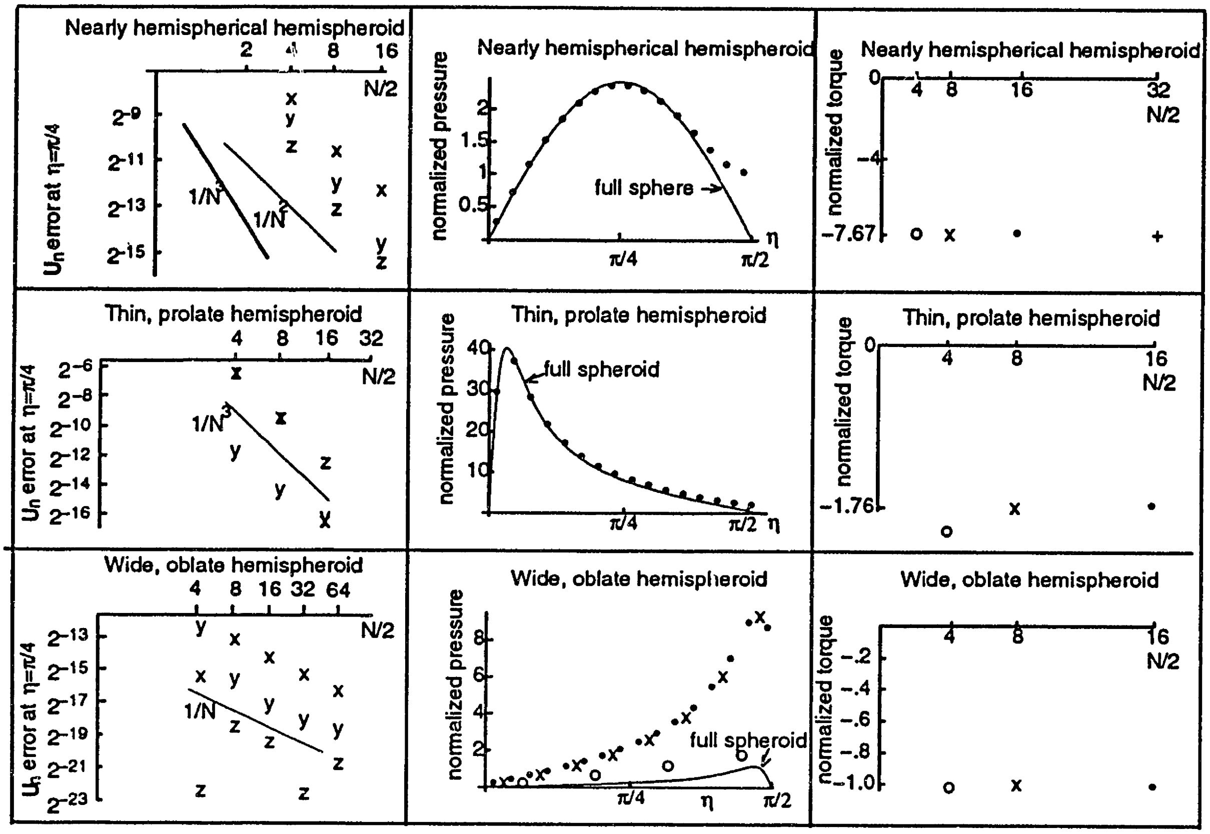

Figure 4-22: Left panels: The error as a function of N for a nearly hemispherical hemispheroid, $\xi_o = 5$ a thin prolate hemispheroid, $\xi_o = .1$, and a wide, oblate hemispheroid, $\xi_o = .1$ for translational motion, at $\eta = \pi/4$. x indicates the error for $U_{x,n}$, y indicates the error for $U_{y,n}$, z indicates the error for $U_{z,n}$.
Middle panels: The normalized pressure for a nearly hemispherical hemispheroid, $\xi_o = 5$, a thin prolate hemispheroid, $\xi_o = .1$, and a wide, oblate hemispheroid, $\xi_o = .1$ for translational motion, on the surface at $q = 0$. For the nearly hemispherical hemispheroid, the pressure was calculated at $\xi = 5.01$. For the thin prolate hemispheroid, the pressure was calculated at $\xi = .101$. For the wide, oblate hemispheroid, the pressure was calculated at $\xi = .101$. The normalized pressure on the surface for a full spheroid (solid line) in translational motion is also indicated.
Right panels: The normalized torque induced by the hemispheroid on the fluid in translational motion for a nearly hemispherical hemispheroid, $\xi_o = 5$, a thin prolate hemispheroid, $\xi_o = .1$, and a wide, oblate hemispheroid, $\xi_o = .1$.
The data are represented by the following symbols: o for $N/2 = 4$;x for $N/2 = 8$; • for $N/2 = 16$; + for $N/2 = 32$; – for $N/2 = 64$; and = for $N/2 = 128$. Note the change in scales for each plot.

4.6.2 Translational motion—a thin, prolate hemispheroid

The results for a thin, prolate hemispheroid (Figure 4-18 middle) in translational motion are illustrated in the middle panels of Figure 4-19-Figure 4-22. The middle panels of Figure 4-19 illustrate the normalized source weightings. For this structure, for small η, $\hat{a}_{x0,n}$, and $\hat{a}_{x2,n}$, vary more rapidly with η than the corresponding source weightings for the nearly hemispherical hemisphere. Therefore, for small η, for a given $N/2$, the errors in $\hat{a}_{x0,n}$, and $\hat{a}_{x2,n}$ are larger than those of the nearly hemispherical hemisphere. By comparing the middle panels and the top panels of Figure 4-21, we see that the errors in surface velocities are generally larger for $N/2 = 4$ than those of of the top panels. This is understandable— the source weightings vary more rapidly with η for the thin prolate hemispheroid than for the nearly hemispherical hemispheroid, so the piecewise constant approximations are not as good. As a function of N, the error at $\eta = \pi/4$ decreases as approximately as $1/N^3$. The pressure on the surface of the thin, prolate hemispheroid (center panel of Figure 4-22) more closely approximates that of the full prolate spheroid than the surface pressure of the nearly hemispherical hemispheroid approximates that of the nearly spherical spheroid. This makes sense— the thin, prolate hemispheroid has less surface area along the plate than the nearly hemispherical hemispheroid, and hence the effects of the plate are less pronounced. The torque (right, middle panel of Figure 4-22) for $N/2 = 4$ differs from the torque for $N/2 = 16$ by about 17%, however, the difference in torque for $N/2 = 8$ and $N/2 = 16$ is less than .6%.

4.6.3 Translational motion—a wide, flat, oblate hemispheroid

The lower panels of Figure 4-19-Figure 4-22 illustrate the results for a wide, flat, oblate hemispheroid (Figure 4-18 lower). The largest source term, $\hat{a}_{x0,n}$, shown in the lower panel of Figure 4-19, varies less with η than the corresponding $\hat{a}_{x0,n}$ for both the nearly hemispherical hemispheroid (top panel), and the thin, prolate hemispheroid (middle panel), and hence the errors in the surface velocities, for a given $N/2$ (lower panels of Figure 4-21 and lower left panel of Figure 4-22), are less than those of the other shapes shown in the top and middle panels. The errors decrease as $1/N$, a smaller power of N than the errors of the previous two shapes. Since the sources are relatively constant with η, the error due to discretization is less significant to the total error than in the other two examples and that is probably why the errors decrease more slowly with N. The pressure along the surface least resembles that for a full oblate spheroid because the surface area of the hemispheroid along the plate is largest for the most oblate hemispheroid.

4.6.4 Rotational motion

Discontinuity in the boundary conditions

For rotational motion, there is a discontinuity in the $\hat{\mathbf{z}}$ component of the surface velocity along the hemispheroid-plate interface, i.e., at $\eta = \pi/2$, $\xi = \xi_o$ the surface velocity for the hemispheroid is given by,

$$U_z = -\Theta x,$$

and for the plate

$$U_z = 0.$$

The discontinuity in the boundary conditions results from the relative motion between two rigid structures: the hemispheroid and plate. The discontinuity in surface velocity causes the pressure as well as components of the source weightings to be infinite at the interface. However, we will show that we can accurately calculate fluid velocity and hydrodynamic torque despite the discontinuity.

Singularity in pressure and source weightings

Figure 4-23 and Figure 4-24 illustrate the normalized pressure and normalized source weightings, as a function of radial distance from the singularity, for a wide, oblate hemispheroid. The same issues arise for the prolate case, but the discontinuity is larger for the oblate case. Therefore, we chose to examine these results for the wide, oblate hemispheroid. The pressure approaches infinity at the points, $r = r_o$, which are the set of points where $\xi = \xi_o$, $\eta = \pi/2$. These set the points define the circle where the hemispheroid and plate meet. We see that both the pressure and source weightings decrease more slowly than $1/r$, so that the singularity is integrable. Therefore the results for the fluid velocities and the results for torque are valid.

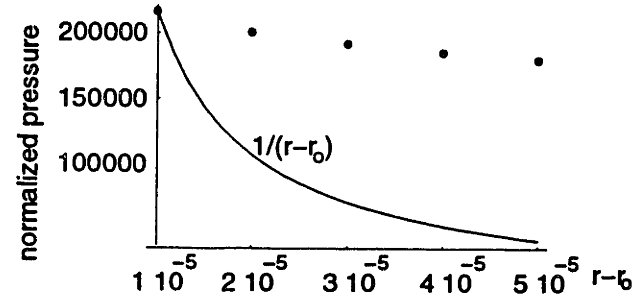

Figure 4-23: The normalized pressure as a function of r for $N/2 = 16$, with $\eta = \pi/2$, $q = 0$, for a wide, oblate hemispheroid. The line indicates $1/(r - r_o)$ where $r_o = (\xi = \xi_o, \eta = \pi/2, q = 0)$.

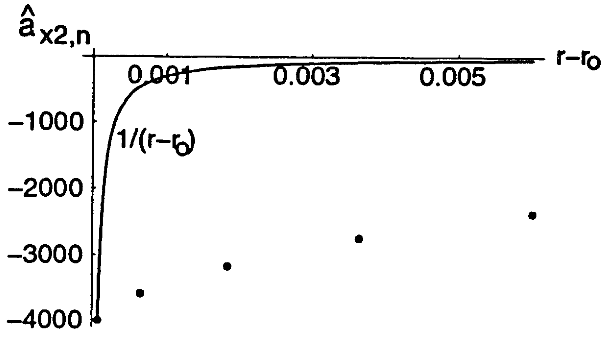

Figure 4-24: The normalized source weighting, $\hat{a}_{x2,n}$ as a function of r, along the surface of a wide, oblate hemispheroid ($N/2 = 256$). The line indicates $1/(r - r_o)$ where $r_o = (\xi = \xi_o, \eta = \pi/2, q = 0)$.

The torque calculation without the singularity present

No discontinuity would result if the structures were deformable. We simulated the case in which the bottom portion of the hemispheriod deformed uniformly by having the boundary velocity U_z linearly decay to zero from some arbitrary point, $\eta = \eta_r$, to $\eta = \pi/2$ at the plate. Figure 4-25 indicates U_z along the surface. We studied the normalized torque for velocity profiles with different η_r (Figure 4-26). To adequately sample the portion of the surface where the velocity ramps to zero, we discretized the surface nonuniformly— the spacing between the points for $0 < \eta < 31\pi/64$ was equal to $\pi/64$. The spacing between the points for $31\pi/64 < \eta < \pi/2$ was equal to $\pi/6144$. As $\eta_r \to \pi/2$, the solution converges to that of the case where the discontinuity is present, indicating that the discontinuity is not affecting the torque calculation.

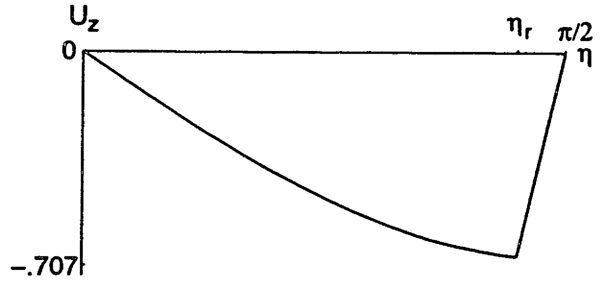

Figure 4-25: $U_z/(\Theta)$ for the wide, oblate hemispheroid along the contour $q = \pi/4$ with no discontinuity.

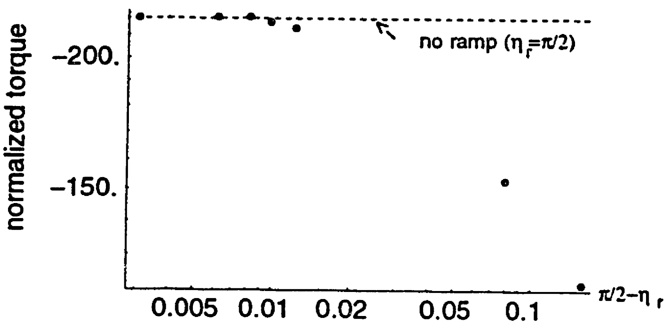

Figure 4-26: The torque for a wide, oblate hemispheroid as a function of η_r, the point along the surface where the velocity starts to decay to zero.

4.6.5 Rotational motion—a nearly hemispherical hemispheroid

The results for rotational motion are shown in Figure 4-27-Figure 4-29. For the nearly hemispherical hemispheroid, the normalized weightings, $\hat{a}_{z1,n}$ (top middle panel of Figure 4-27) and $\hat{a}_{x2,n}$ (top right panel of Figure 4-27) approach infinity near the bottom of the hemispheroid, $\eta = \pi/2$. As N increases, the errors in velocity decrease (top panels of Figure 4-28). The errors in $U_{z,n}$ (Figure 4-28 top right panel) are largest and increase dramatically as $\eta \rightarrow \pi/2$. Near the plate, the errors decrease more slowly with N.

For a full sphere, the pressure on the surface due to rotational motion is zero. For the nearly hemispherical hemispheroid with a plate, the pressure along the surface away from the plate is negative and small in magnitude (top middle panel of Figure 4-29). It decreases until $\eta \approx 2\pi/5$, and then starts to increase. Because of the discontinuity in the surface velocities at the plate, the pressure approaches infinity as $\eta \rightarrow \pi/2$. The torque (top right panel Figure 4-29) converges more slowly than the torque for translational motion (top right panel Figure 4-22). For rotational motion, the torque is within 1% of its final result for $N/2 = 32$ while for translational motion, the torque is within 1% of its final result for $N/2 = 4$. The normalized torque for rotational motion is nearly five times that of translational motion, because, for rotational motion, more fluid is being forced in a direction perpendicular to the plate. We see that for oblate hemispheroids (Figure 4-29 and Figure 4-22 bottom right panels) this effect is much more pronounced since over most of the surface the rotational motion for a wide, oblate hemispheroid is mainly in the $\hat{\mathbf{z}}$ direction. For the thin prolate hemispheroid the normalized torque for rotational motion (Figure 4-29 middle right panel) is nearly the same as that of translation motion (Figure 4-22 middle right panel), because, over most of the surface, the rotational motion is mainly in the $\hat{\mathbf{x}}$ direction.

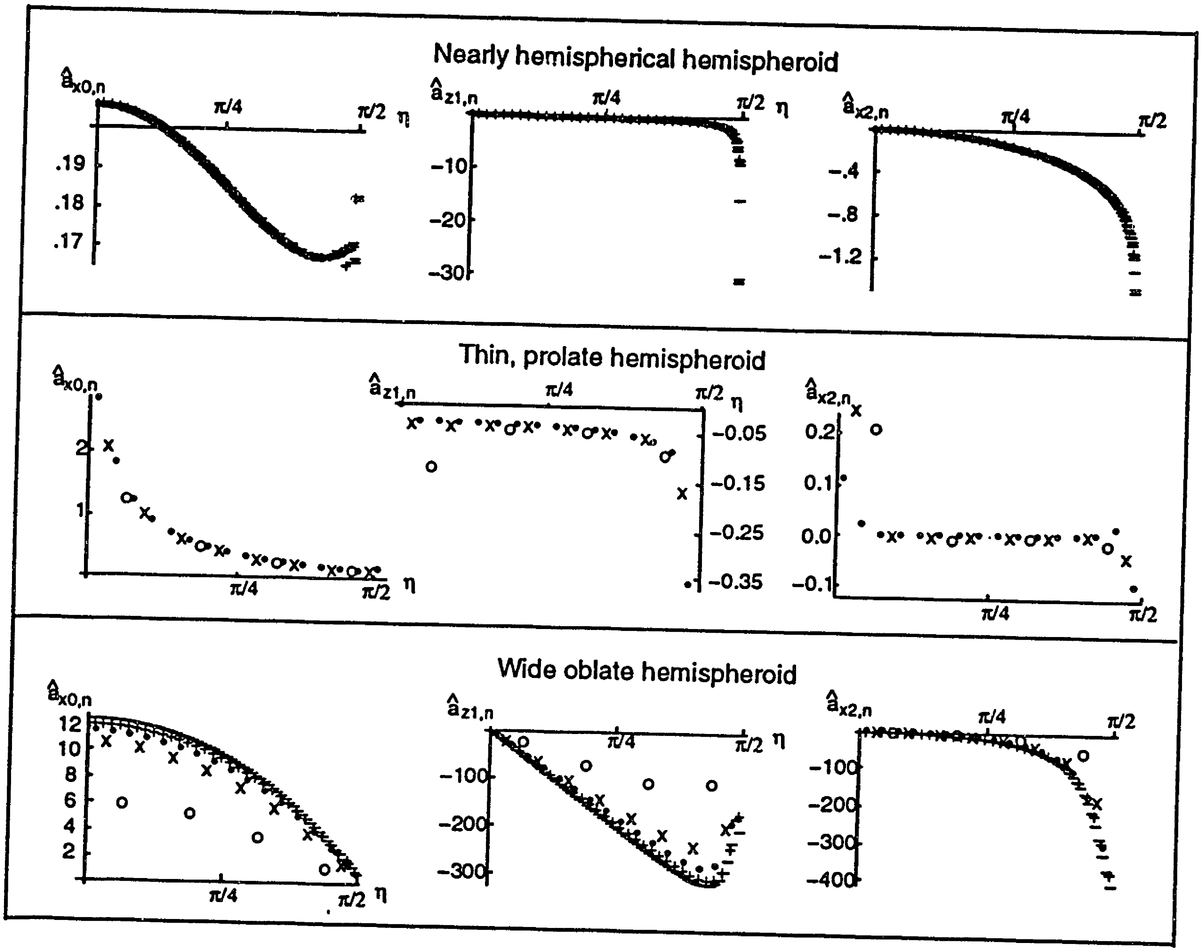

Figure 4-27: The normalized source weightings, $\hat{a}_{x0,n} = \hat{a}_{x0}/(\mu\Theta)$, $\hat{a}_{z1,n} = \hat{a}_{z1}/(\mu\Theta)$ and $\hat{a}_{x2,n} = \hat{a}_{x2}/(\mu\Theta)$ for a nearly hemispherical hemispheroid $\xi_o = 5$, (top), a thin prolate hemispheroid, $\xi_o = .1$ (middle), and a wide, oblate hemispheroid, $\xi_o = .1$ (bottom) for rotational motion. The data are represented by the following symbols: o for $N/2 = 4$;x for $N/2 = 8$; • for $N/2 = 16$; + for $N/2 = 32$; − for $N/2 = 64$; and = for $N/2 = 128$. Note the change in scales for each plot.

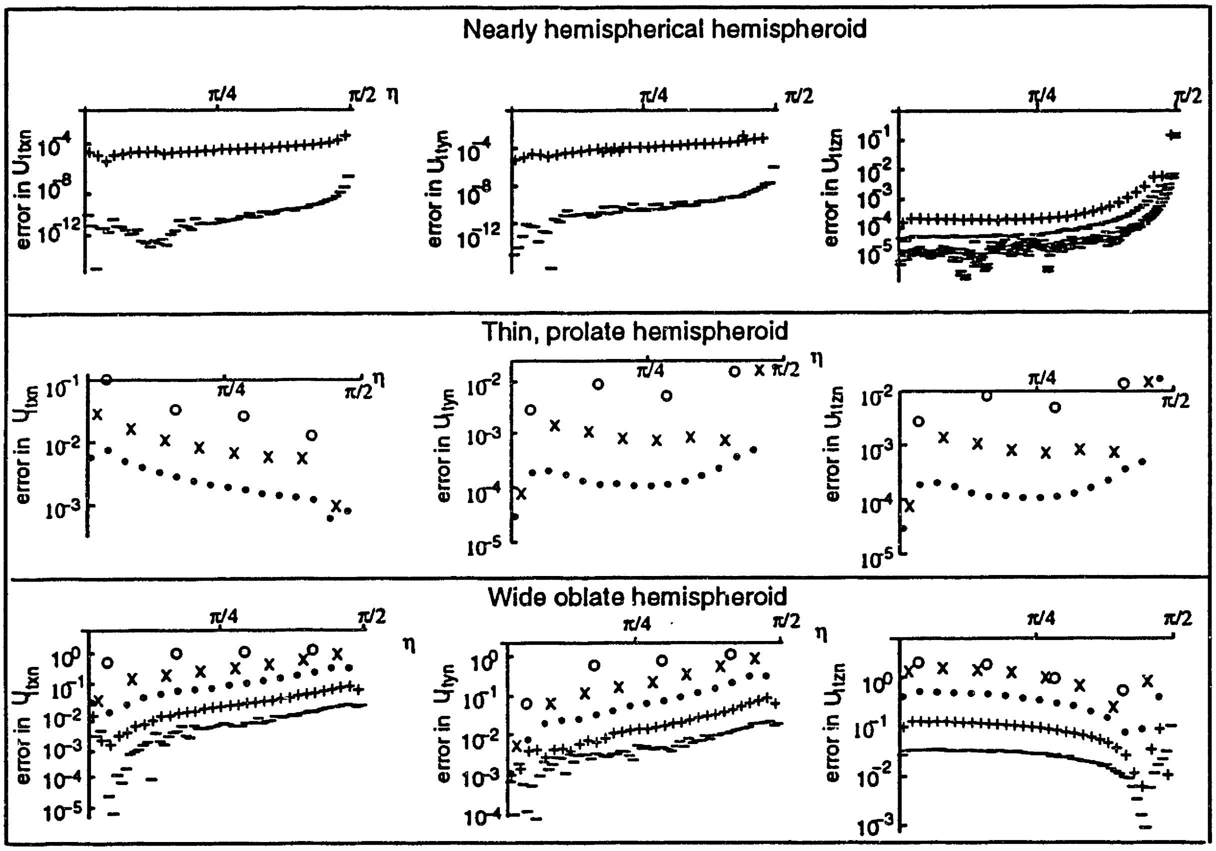

Figure 4-28: The error for each velocity component, i.e., the magnitude of the difference between the normalized results and the normalized boundary conditions along the arc, $q = \pi/4$ for a nearly hemispherical hemispheroid, $\xi_o = 5$ (top), a thin prolate hemispheroid, $\xi_o = .1$ (middle), and a wide, oblate hemispheroid, $\xi_o = .1$ (bottom) for rotational motion. The data are represented by the following symbols: o for $N/2 = 4$;x for $N/2 = 8$; • for $N/2 = 16$; $+$ for $N/2 = 32$; $-$ for $N/2 = 64$; and $=$ for $N/2 = 128$. Note the change in scales for each plot.

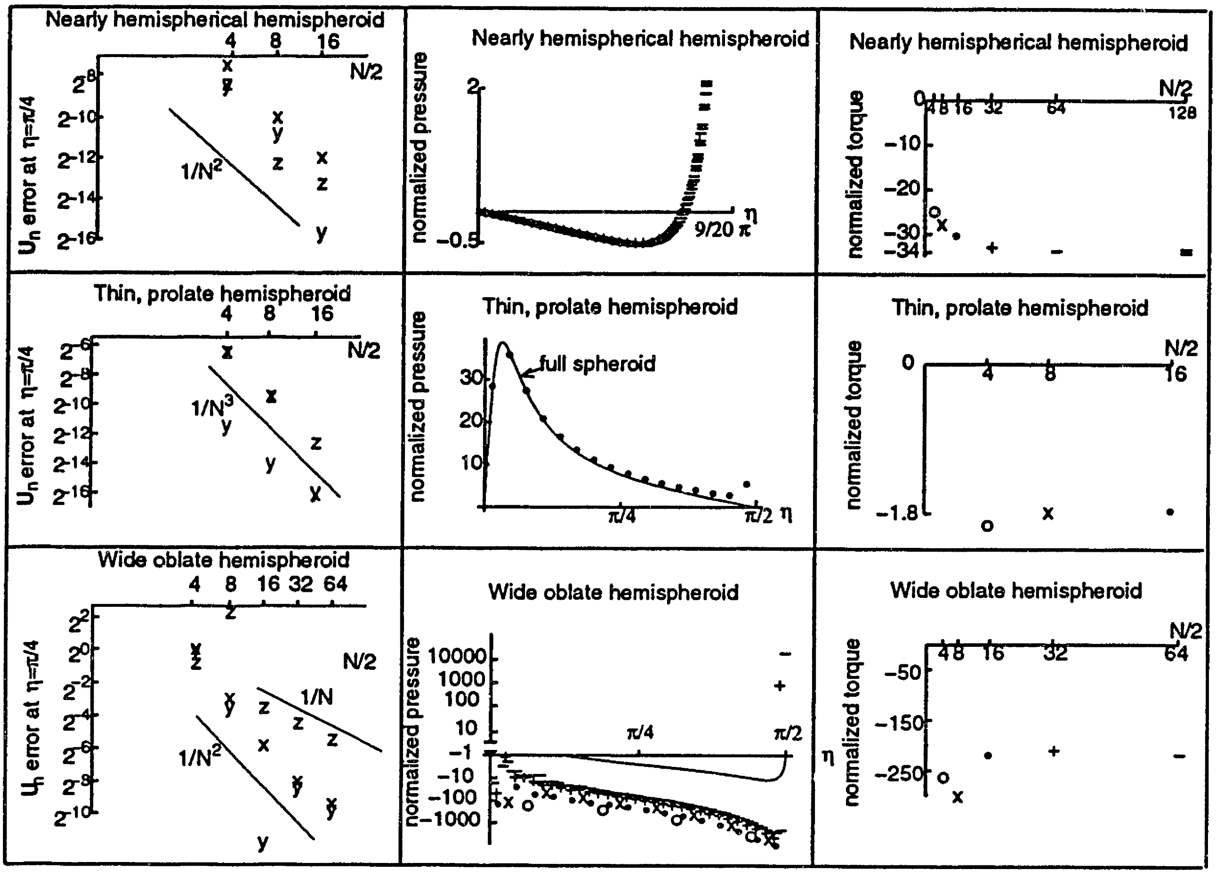

Figure 4-29: Left panels: The error as a function of N for a nearly hemispherical hemispheroid, $\xi_o = 5$, a thin prolate hemispheroid, $\xi_o = .1$, and a wide, oblate hemispheroid, $\xi_o = .1$ for rotational motion, at $\eta = \pi/4$. x indicates the error for $U_{x,n}$, y indicates the error for $U_{y,n}$, z indicates the error for $U_{z,n}$.
Middle panels: The normalized pressure for a nearly hemispherical hemispheroid, $\xi_o = 5$, a thin prolate hemispheroid, $\xi_o = .1$, and a wide, oblate hemispheroid, $\xi_o = .1$ for rotational motion, on the surface at $q = 0$. For the nearly hemispherical hemispheroid, the pressure was calculated at $\xi = 5.01$. For the thin prolate hemispheroid, the pressure was calculated at $\xi = .101$. For the wide, oblate hemispheroid, the pressure was calculated at $\xi = .101$.
Right panels: The normalized torque induced by the hemispheroid on the fluid in rotational motion for a nearly hemispherical hemispheroid, $\xi_o = 5$, a thin prolate hemispheroid, $\xi_o = .1$, and a wide, oblate hemispheroid, $\xi_o = .1$.
The data are represented by the following symbols: o for $N/2 = 4$;x for $N/2 = 8$; $\bullet$ for $N/2 = 16$; $+$ for $N/2 = 32$; $-$ for $N/2 = 64$; and $=$ for $N/2 = 128$. Note the change in scales for each plot.

4.6.6 Rotational motion—a thin, prolate hemispheroid, and a wide, oblate hemispheroid

The results for the prolate hemispheroid for rotational motion are the most similar to those of translational motion because for a thin, prolate hemispheroid, over most of the surface, the rotational motion is translational, that is, in the $\hat{\mathbf{x}}$ direction. As we would expect, since the discontinuity is smallest for the thin, prolate hemispheroid, the increase in source weightings (Figure 4-27 middle panels) and pressure (Figure 4-29 center panel) as $\eta \rightarrow \pi/2$ are the least pronounced of all the shapes. In contrast, for the wide, oblate hemispheroid, the increase source weightings (Figure 4-27 bottom panels) and pressure (Figure 4-29 bottom center panel) as $\eta \rightarrow \pi/2$ are the largest. The errors for a given N for the wide, oblate hemispheroid (Figure 4-29 bottom left panel) are larger than those of other shapes because the discontinuity in surface velocity is the largest. The errors in velocity at $\eta = \pi/4$ decrease as $1/N^3$ for the thin prolate shape (Figure 4-29 middle left panel) but decrease as $1/N$ for the wide oblate shape (Figure 4-29 bottom left panel) probably because of the difficulty in representing the large discontinuity in surface velocity. The torque for the wide oblate hemispheroid (Figure 4-29 bottom right panel) also requires a large N to converge to its final value. The magnitude of this torque is also largest because the wide, oblate hemispheroid is forcing the most fluid into the stationary plate.

As in translational motion, the pressure along the surface of the wide, oblate hemispheroid (Figure 4-29 bottom center panel) is the least like that of the wide, oblate spheroid, while the pressure along the surface of the thin prolate hemispheroid is close to that of the thin, prolate spheroid (Figure 4-29 center panel) . For all shapes, the pressures for translational motion for hemispheroids with a plate are closer to those of full spheroids than those of rotational motion indicating that the plate has a greater effect for rotational motion than for translational motion.

4.6.7 Conclusion

We have studied the results for three extrema of hemispheroidal shapes for translational and rotational motion. We found that as N increases, the errors in surface velocity decrease, and the errors for rotational motion are larger than those of translational motion for the same shape. This is due to the discontinuity in the surface velocity for rotational motion, which results in source weightings and pressure that approach infinity at the discontinuity. However, we demonstrated that the pressures and source weightings approach infinity as $1/(r^{\alpha})$ with $\alpha < 1$, so that the singularities are integrable and valid results for the fluid velocity, pressure (away from the discontinuity), and torque were obtained. We also compare the pressures along the surface to those of full spheroids of the same shape. We found that the pressures for the thin, prolate hemispheroids are closer to those of the full spheroids than the pressures for the other shapes because the surface area of the hemispheroid-plate interface is the smallest. The differences in pressures between the hemispheroids and the full spheroids were greater for rotational motion than for translational motion because the effect of the plate is more pronounced for rotational motion.

We also studied the hydrodynamic torque induced by the motion of the hemispheroid. The torque for rotational motion required a larger N to converge to its final value due to the discontinuity in the surface velocities. We found that for all shapes the torque converges to within 3% of its value for $N/2 = 32$.

4.7 The effect of shape in the limit of low frequencies

Since we have checked our numerical results, we are now ready to determine the effect of shape on the hydrodynamic pressure, velocity and torque in the limit of low frequencies for the hemispheroid model. Dimensional analysis and the exact solutions for full spheroids will allow us to understand the important shape quantities that affect the hydrodynamics.

4.7.1 Dimensional Analysis

Even without solving the equations of motion for the hemispheroid on a plate, we can gain understanding of the effect of size of the hemispheroid on the hydrodynamics by using dimensional analysis. To use dimensional analysis we need to understand how the dimensions of the problem are determined. In Section 2.1.5, we found that Stokes equation can be used to describe conservation of momentum. The only parameter in Stokes equation is μ, with dimensions, mass/(length-time). From the geometry of the problem, the only parameter with dimensions is L, the focal length of the hemispheroid, with dimensions of length. Although the shape depends on ξ_o, this factor is dimensionless and so we cannot use it in our dimensional analysis. For translational motion, we determined that, in the limit of low frequencies, the variables that determine the hydrodynamics are proportional to $\sqrt{j\omega\rho/\mu}$. This quantity has dimensions, 1/length. The boundary conditions for translational motion are given by Equations 4.23-4.25. In these equations the only quantity with dimensions is U_b, with dimensions, length/time. From Equation 2.8, U_b always is multiplied by $\sqrt{j\omega\rho/\mu}$, and the dimensions of the product is 1/time. Since μ, $\sqrt{j\omega\rho/\mu}U_b$, and L, are the parameters that determine the dimensions, we can express the fluid velocity, pressure and torque for translational motion as

$$\mathbf{U}(\mathbf{r},\xi_o) = \mathbf{U}'(\mathbf{r},\xi_o)\sqrt{\frac{j\omega\rho}{\mu}}U_bL,$$

$$\begin{aligned} P(\mathbf{r},\xi_o) &= P'(\mathbf{r},\xi_o)\mu\sqrt{\frac{j\omega\rho}{\mu}}U_b, \\ T_y(\xi_o) &= T'_y(\xi_o)\mu\sqrt{\frac{j\omega\rho}{\mu}}U_bL^3, \end{aligned}$$

where $\mathbf{U}'(\mathbf{r},\xi_o)$, $p'(\mathbf{r},\xi_o)$, and $T'_y(\xi_o)$ represent dimensionless variables.[2] Note that these combinations of the parameters are unique—no other combination will give the correct dimensions for velocity, pressure, and torque.

For rotational motion, the hydrodynamic variables are proportional to $j\omega$ with dimensions 1/time. The only quantity with dimensions in the boundary conditions (Equations 2.18-2.19) is Θ which has dimensions of radians. Therefore, for rotational motion, the hydodynamic variables can be expressed as

$$\begin{aligned} \mathbf{U}(\mathbf{r},\xi_o) &= \mathbf{U}'(\mathbf{r},\xi_o)j\omega\Theta L, \\ P(\mathbf{r},\xi_o) &= P'(\mathbf{r},\xi_o)\mu j\omega\Theta, \\ T_y(\xi_o) &= T'_y(\xi_o)\mu j\omega\Theta L^3. \end{aligned}$$

From this analysis, for both translation and rotation, we see that the velocity is proportional to L, the pressure is independent of L, and the torque is proportional to L^3. To determine the correct ξ_o dependence, we will have to study the results of the BEMA. However, dimensional analysis also tells us that the hydrodynamics for a hemispheroid whose surface is described by $\xi = \xi_o$ for any L can be determined from the results for a hemispheroid with the same aspect ratio and a particular L, by simply scaling by the appropriate power of L. So we see, dimensional analysis not only gave us information about the effects of shape, but also simplified the analysis, by reducing the number of numerical simulations that need to be performed.

---

[2] Note that $\mathbf{U}(\mathbf{r},\xi_o)$ is only a portion of the fluid velocity, but it is only this portion that determines pressure and torque (See Section 4.5.1).

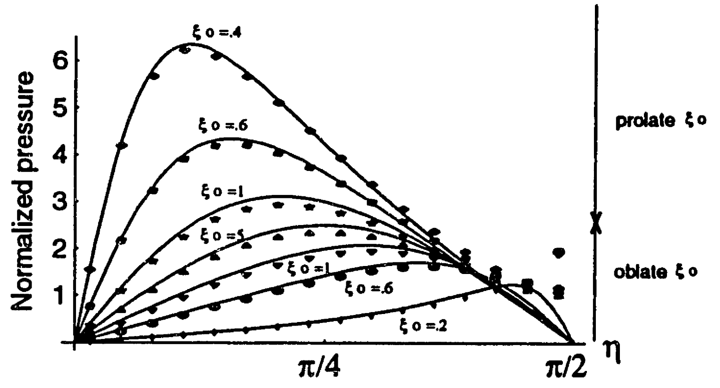

Figure 4-30: The pressure on the surface for translational motion, with $q = 0$ for $N/2 = 16$. The symbols represent the results for a hemispheroid, and the solid lines represent the results for a full spheroid.

4.7.2 Hydrodynamic pressure

With dimensional analysis, we found that the pressure is independent of L and so we know that the pressure on the surface of a hemispheroid is independent of size. We also know that the pressure must have a $\cos q$ dependence. However, we have yet to determine the dependence of the pressure on η, and ξ_o; we will determine this dependence in this section.

Translational motion

The normalized pressure on the surface for translational motion is illustrated in Figure 4-30. Results for a full spheroid are almost the same for points away from the plate ($\eta < 3\pi/8$) but are different near the plate. From symmetry, the pressure at $\eta = \pi/2$ for a full spheroid must be zero. For a hemispheroid, the pressure is non-zero along the plate.

For most shapes the pressure increases and then decreases as η increases from zero to $\pi/2$. The increase is sharpest for the most prolate shapes, because the prolate shapes have large surface gradients near the tip. For shapes that are very oblate, the pressure is largest away from the tip and close to $\eta = \pi/2$ where the surface gradient is largest. At $\eta = \pi/2$, where the pressure for full spheroids is zero, the oblate shapes of the hemispheroid have the largest pressures. This indicates that the plate has a more profound effect as the shape becomes more oblate.

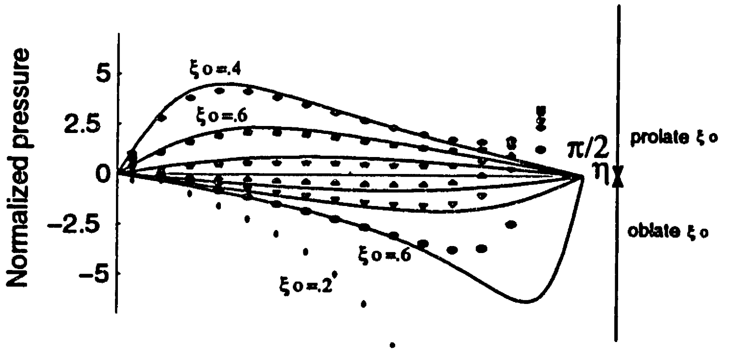

Figure 4-31: The pressure on the surface for rotational motion, with $q = 0$. The symbols represent the results for a hemispheroid, and the solid lines represent the results for a full spheroid.

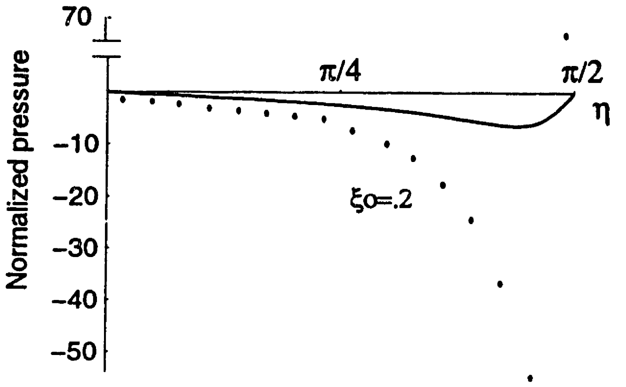

Figure 4-32: The pressure on the surface for an oblate shape, $\xi_o = .2$, for rotational motion, with $q = 0$. The "." represent the results for a hemispheroid, and the solid line represents the results for a full spheroid.

Rotational motion

For rotational motion, the pressure on the surface is shown in Figure 4-31. For prolate shapes, the normalized pressure resembles that of translational motion. The reason for this is clear. Recall that for translational motion, the velocity of the surface is proportional to $z\hat{\mathbf{x}}$. For rotational motion, the surface velocity is proportional to $z\hat{\mathbf{x}} - x\hat{\mathbf{z}}$. For prolate shapes, the velocity $-x\hat{\mathbf{z}}$ is small, so that the large motions are in $\hat{\mathbf{x}}$ only. For oblate shapes, $z\hat{\mathbf{x}}$ is small, so that the velocity is dominated by $-x\hat{\mathbf{z}}$, and the pressure on the surface, at $q = 0$, is negative.

The effect of the plate is more pronounced in rotational motion than in translational motion, especially for more oblate shapes. This is because the plate directly obstructs the flow in $-\hat{\mathbf{z}}$, which results in an increase in the hydrodynamic pressure. Figure 4-32 illustrates the surface pressure for a wide, oblate hemispheroid, ($\xi_o = .2$).

In Figure 4-32, the pressure next to the plate is large and positive. This is true of all shapes, and is a consequence of the discontinuity in the surface velocity at the plate as was discussed in Section 4.6.4.

Hydrodynamic pressure far from the surface

To understand how the pressure decays far from the surface, we will first study how the Green's functions for pressure decay far from the surface. Let us represent the Green's functions for pressure as a Taylor series in r, the radial distance,

$$G_{pi}(r) = \sum_{n=1}^{\infty} a_n r^{-n}.$$

$G_{pi}(r)$ expresses a series representation of the Green's function for the hemispheroid on a plate, Equation 4.28. Since the pressure is a weighted sum of the Green's functions for pressure, the decay in pressure with r can not have any terms that are not present in the Green's function. However, the weightings of the Green's functions can be such that there are cancellations of some terms so that not all the terms present in the Green's functions need be present in the actual pressure.

Each term of the stokeslet, given by Equation 4.4, decays as $1/r^2$ for large r. However, if we expand the Green's functions of the hemispheroid with a plate (Equation 4.28) in a Taylor series in r as $r \to \infty$, we find, for sources in $\hat{\mathbf{x}}$ and $\hat{\mathbf{y}}$, the lowest order term of the series is $1/r^3$. There is no $1/r^2$ term because each component of the vector Green's function contains a stokeslet minus an image stokeslet, and the $1/r^2$ term was cancelled. For the sources in $\hat{\mathbf{z}}$ the lowest order term is $1/r^4$. Since the $\hat{\mathbf{z}}$ sources are weighted by $\cos q'$, a cancellation of the $1/r^3$ term occurs by the sum of the sources at $q' = q_1$ and $q' = q_1 + \pi$, where q_1 represents an angle between 0 and π.

The pressure as a function of r for different hemispheroidal shapes is illustrated in Figure 4-33 and Figure 4-34. We see that the pressure decays at least as fast as $1/r^3$ as predicted by the Green's functions. For translational motion, the pressure is actually decaying close to $1/r^4$, and it might be that the weightings cancel the $1/r^3$ term. For a full spheroid (not shown), the pressure decays as $1/r^3$, as can be seen by expanding the exact solution as $r \to \infty$.

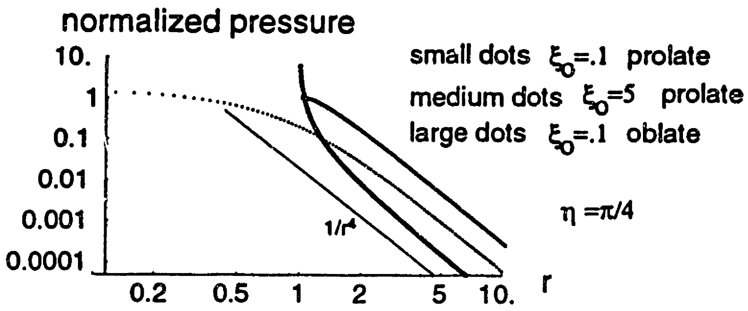

Figure 4-33: The pressure for translational motion as a function of r for $q = 0$, and $\eta = \pi/4$. The results are illustrated for three shapes, prolate, $\xi_o = .1$ (small dots), nearly hemispherical (middle-size dots), and oblate, $\xi_o = .1$ (large dots).

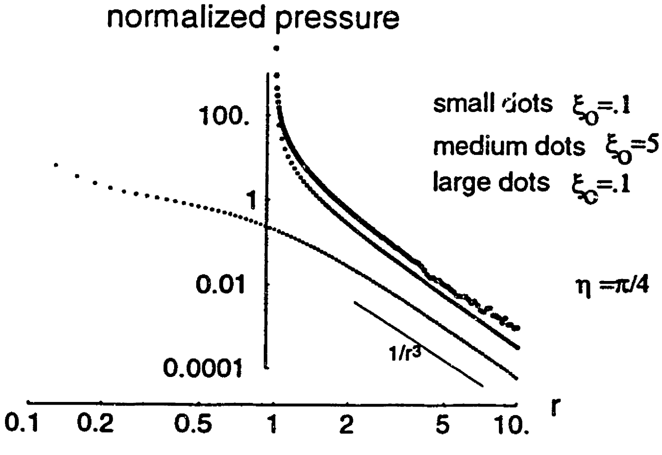

Figure 4-34: The pressure for rotational motion as a function of r for $q = 0$, and $\eta = \pi/4$. The results are illustrated for three shapes, prolate, $\xi_o = .1$ (small dots), nearly hemispherical (middle-size dots), and oblate, $\xi_o = .1$ (large dots).

4.7.3 Fluid velocity

Translational motion

We demonstrated in Section 2.2.5, that the fluid velocity for translational motion can be expressed as the sum of three terms,

$$\mathbf{U}(\mathbf{r}) = U_b\hat{\mathbf{x}} + \sqrt{\frac{j\omega\rho}{\mu}}\mathbf{U}_{1t}(\mathbf{r}) + U_b\sqrt{\frac{j\omega\rho}{\mu}}z\hat{\mathbf{x}}.$$

The first two terms derive from the series expansion in $\sqrt{j\omega\rho/\mu}$, and the third term is due to a translation of the coordinate system. Since only the $\sqrt{\frac{j\omega\rho}{\mu}}\mathbf{U}_{1t}(\mathbf{r})$ contributes to the pressure and torque, we will examine this component more closely to explore the effect of shape on the hydrodynamics.

As in Chapter 3, let us examine the ratio of $U_{1t,\eta}(\mathbf{r})/U_{1t,q}(\mathbf{r})$ on the surface as a function of ξ_o for oblate and prolate hemispheroids. Recall that $U_{1t,\eta}(\mathbf{r})$ represents the component of the fluid velocity in the direction that goes over the hemispheroid, and $U_{1t,q}(\mathbf{r})$ represents the component of the fluid velocity in the direction that goes around the hemispheroid. A plot of $U_{1t,\eta}(\mathbf{r})/U_{1t,q}(\mathbf{r})$ for different shapes is illustrated in Figure 4-35. Two features are evident– the magnitude of the ratio decreases from tip to base, and the magnitude of the ratio increases as the shapes change from prolate to oblate. These features match with our intuition and our results in the high frequency limit. Fluid is more likely to go over the hemispheroid near the tip because the distance the fluid must travel to go over the hemispheroid increases from tip to base. As the shape of the hemispheroid widens, more fluid goes over the hemispheroid since the distance the fluid must travel to go around increases.

Rotational motion

The velocity for rotational motion is given by

$$\mathbf{U}(\mathbf{r}) = j\omega\mathbf{U}_1(\mathbf{r}),$$

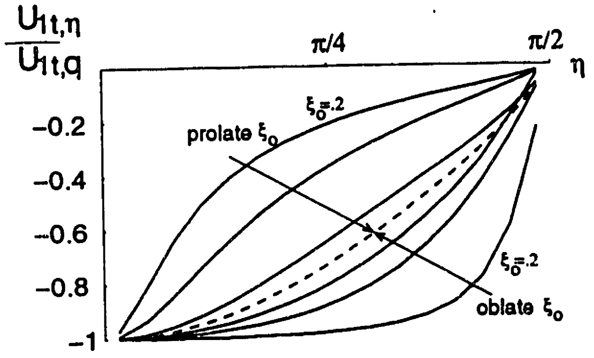

Figure 4-35: The ratio $U_{1t,\eta}(\mathbf{r})/U_{1t,q}(\mathbf{r})$, with $q = \pi/4$ for translational motion. The dashed line indicates the ratio for a hemisphere.

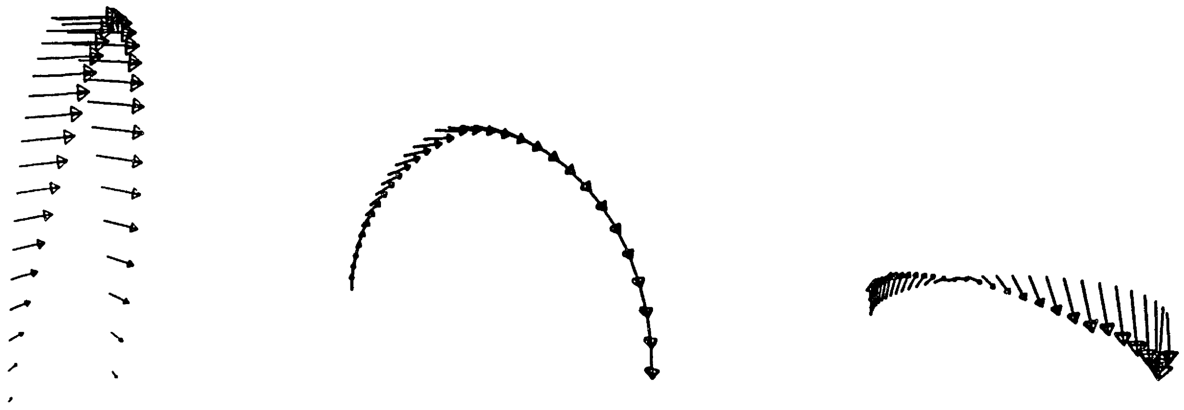

ξ_0=.2 prolate ξ_0=5 prolate or oblate ξ_0=.2 oblate

Figure 4-36: The velocity field next to the surface for $q = 3\pi/4$ and $q = 7\pi/4$ for three different shapes. The hemispheroids are not shown.

where $\mathbf{U}_1(\mathbf{r})$ is described in Section 2.2.5. The effect of shape on the velocity field near the surface can easily be seen in Figure 4-36 which shows part of the velocity field for three shapes- thin prolate, hemispherical, and wide oblate. For the thin, prolate hemispheroid, fluid flows mainly in $\hat{\mathbf{x}}$. For the wide oblate hemispheroid, fluid flows mainly in $\hat{\mathbf{z}}$. The fluid flow pattern of the hemisphere is on between that of the other two shapes so we see that more fluid goes over the hemispheroid as the shape widens. A plot of $U_{1,\eta}(\mathbf{r})/U_{1,q}(\mathbf{r})$ for rotational motion is illustrated in Figure 4-37, and the feature we observed in Figure 4-36 is obvious here too— the magnitude of the ratio, $U_{1,\eta}(\mathbf{r})/U_{1,q}(\mathbf{r})$ increases as the shape widens. This is because the component of surface velocity in $\hat{\eta}$ direction increases as the shape widens.

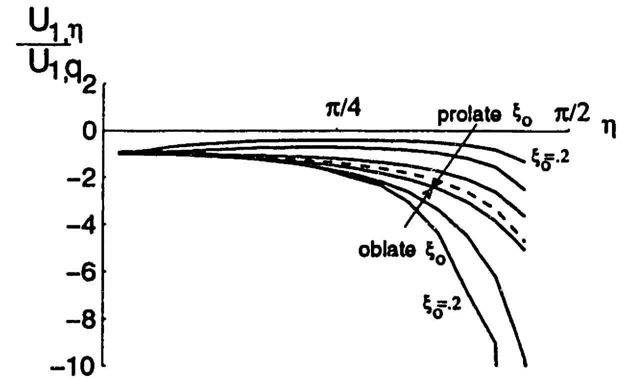

Figure 4-37: The ratio $U_{1,\eta}(\mathbf{r})/U_{1,q}(\mathbf{r})$, with $q = \pi/4$ for rotational motion. The dashed line indicates the ratio for a hemisphere.

Magnitude of the fluid velocity far from the surface

We obtain the dependence of the magnitude of the fluid velocity on r, far from the surface from the Green's functions for velocity just as we did for pressure in Section 4.7.2. The Green's functions are given by Equation 4.27. If these Green's functions are expanded in a Taylor series as $r \longrightarrow \infty$ we find that the fluid velocity due to sources in $\hat{x}$ and $\hat{y}$ have a $1/r^2$ dependence and that fluid velocity due to sources in $\hat{z}$ have a $1/r^3$ dependence, so that the velocity decays at least as fast as $1/r^2$. Figure 4-38 for translational motion and Figure 4-39 for rotational motion illustrates the fluid velocity as a function of r, and we see that the velocity decays almost as $1/r^2$, except for the case of the wide oblate hemispheroid in rotational motion, where, far from the hemispheroid, we have relatively small velocities and there are significant numerical errors in the velocity calculations.

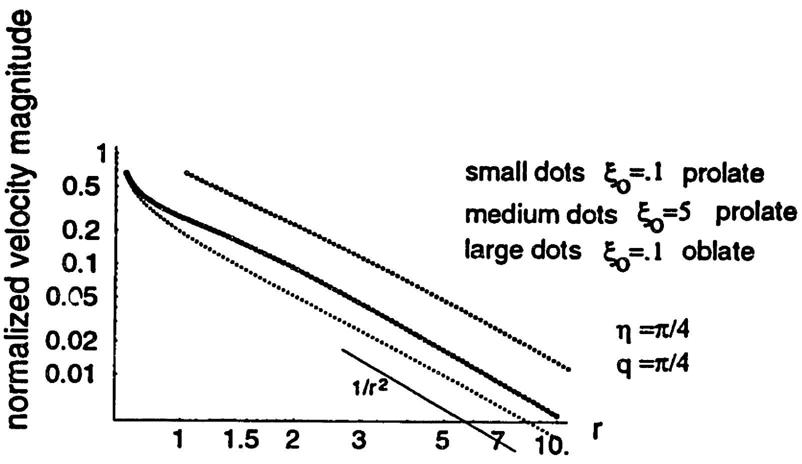

Figure 4-38: The pressure for translational motion as a function of r for $q = \pi/4$, and $\eta = \pi/4$. The results are illustrated for three shapes, prolate, $\xi_o = .1$ (small dots) , nearly hemispherical (middle-size dots), and oblate, $\xi_o = .1$ (large dots).

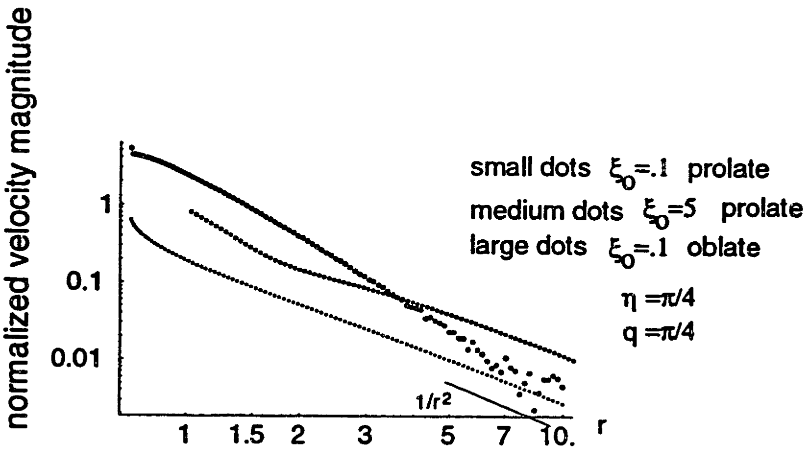

Figure 4-39: The pressure for rotational motion as a function of r for $q = \pi/4$, and $\eta = \pi/4$. The results are illustrated for three shapes, prolate, $\xi_o = .1$ (small dots), nearly hemispherical (middle-size dots), and oblate, $\xi_o = .1$ (large dots).

4.7.4 Hydrodynamic torque

From dimensional analysis, we see that the torque for either translational or rotational motion varies as L^3 (Section 4.7.1). Since both height and width are proportional to L, this implies that the torque becomes infinitely large as the dimensions of the hemispheroid become infinitely large. However, we see that if we factor out from the torque expressions terms that are proportional to L^3, the resulting expression for hydrodynamic torque remains fairly constant over most of the range of hemispheroidal shapes (Figure 4-40). For translational motion, we find that it we divide the torque expression by height cubed, then, except for the extrema in shapes, the resulting torque varies by less than an order of magnitude (right panel of Figure 4-40), This is equivalent to saying that the torque for hemispheroids of the same height varies by less than an order of magnitude for all but the extrema in shapes. The range of hemispheroidal shapes with constant h are seen in Figure 3-3.

For rotational motion, to keep the range of values of the resulting torque expression minimal we divided the torque by h^3 for prolate hemispheroids,and we divided by hw^2 for oblate hemispheroids. The normalized torque for rotational motion is illustrated in the right panel of Figure 4-40. The corresponding range of shapes is depicted in Figure 4-41. Even with these normalizations, the range of normalized torque is larger than that of translational motion, and larger than that of full spheroids, because the plate affects wider hemispheroids more than thinner hemispheroids.

For translational motion, for thin prolate hemispheroids, the torque for the hemispheroid with a plate is half that of a full spheroid because for the plate has little effect on the hydrodynamics for thin prolate hemispheroids, and the surface area of a hemispheriod is half that of a full spheriod. As the shape becomes wider, the plate has more influence on the hydrodynamics along the surface of the hemispheroid, and the torque becomes larger than half that of a full spheriod, and exceeds that of a full spheriod for oblate shapes. For rotational motion, we see the same trends, but the effect of the plate is more pronounced. Since the difference in torque for a full spheroid and a hemispheroid with the same shape factor is less than a factor of two, the analytic solutions for a full spheroid found in the appendix to this chapter can be

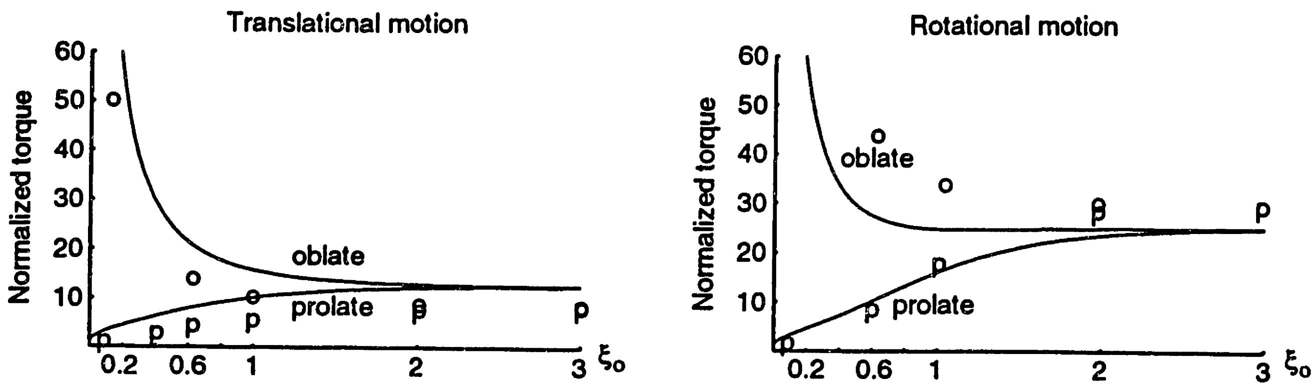

Figure 4-40: Left panel: The normalized, hydrodynamic torque for translational motion, $T_{tyn} = T_{ty}/(\sqrt{j\omega\rho\mu}U_b h^3)$. Right panel: The normalized, hydrodynamic torque for rotational motion, $T_{ryn} = T_{ry}/(j\omega\Theta\mu Q)$, where $Q = h^3$ for prolate shapes and $Q = hw^2$ for oblate shapes. For both panels, p indicates prolate hemispheroids, o indicates oblate hemispheroids, and the solid lines indicate full spheroids, both oblate and prolate.

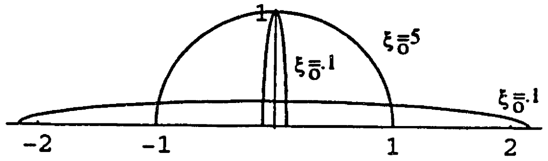

Figure 4-41: The range of shapes for which the torque is calculated in the left panel of Figure 4-40. The prolate hemispheroids have the same height and the oblate hemispheroids have the same volume.

used as approximations to the torque for the hemispheroid on a plate.

4.7.5 Conclusion

From dimensional analysis, we found that the hydrodynamic pressure was independent of the size of the hemispheroid. For translational motion, for most points along the surface, the pressure for thin hemispheroids was larger than the pressure for wider hemispheroids. The effect of the plate on the surface pressure was small except for points near the plate, and for most points on the surface, the exact solution for a full spheroid was a very good approximation for the pressure for the hemispheroid on a plate. Near $\eta = \pi/2$, the plate had more influence, and had a larger effect on the surface pressure for wider shapes. For rotational motion, for most points along the surface, the pressure is positve for prolate hemispheroids, and negative for oblate hemispheroids. The magnitude of the pressure increases as the shape becomes more eccentric. The effect of the plate was larger than in translational motion, especially for wider hemispheroids and the solution for a full spheroid was a poor approximation for wide hemispheroids. Far from the surface, the pressure decreased at least as fast as $1/r^3$.

We found that shape influences fluid velocity at low frequencies. As in high frequencies, more fluid flowed over the hemispheroid and less around the hemispheroid as the shape widened. This was true for both translational and rotational motion. Far from the surface, the magnitude of the velocity decreased as $1/r^2$.

We determined from dimensional analysis that the torque is proportional to the cube of the focal length. We found for translational motion that if we normalize torque by the cube of the height, the torque for nearly the full range of shapes varied by less than an order of magnitude. For prolate hemispheroids, the change in normalized torque with ξ_o was small–less than a factor of two when the ξ_o increases from .1 to .6. For rotational motion, we normalized by h^3 for prolate hemispheroids and by hw^2 for oblate hemispheroids. The resulting normalized torque varied more with ξ_o than that of translational motion, because the influence of the plate increased more as the width increased. Nonetheless, for nearly all shapes, for either mode of motion, the torque for a full spheroid differs from the torque of a hemispheroid with a plate by less than a factor of two, and can be used as an approximation for the torque of a hemispheroid on a plate.

4.8 Appendix

4.8.1 Analytic solutions

The analytic solutions are derived from (Chwang and Wu, 1975). For a full spheroid moving with a constant velocity, U_b, in the $\hat{\mathbf{x}}$ direction the fluid velocity can be expressed as

$$\mathbf{U}(\mathbf{r}) = -\frac{1}{2}(-\alpha\hat{\mathbf{x}}B_{1,0} - \alpha x\hat{\mathbf{z}}(\frac{1}{R_2} - \frac{1}{R_1}) - \alpha x(x\hat{\mathbf{x}} + y\hat{\mathbf{y}})B_{3,0} + \nabla(\beta x(\frac{z-L}{r^2}R_1 - \frac{z+L}{r^2}R_2 + B_{1,0}))),$$

with

$$r = \sqrt{x^2+y^2},\ R_1 = \sqrt{(z+L)^2+r^2},\ R_2 = \sqrt{(z-L)^2+r^2},$$

with the function $B_{m,n}(x, y, z)$ defined as

$$B_{1,0} = \log\tfrac{R_2-(z-L)}{R_1-(z+L)},\ B_{1,1} = R_2 - R_1 + zB_{1,0},$$

$$B_{3,0} = \tfrac{1}{r^2}(\tfrac{z+L}{R_1} - \tfrac{z-L}{R_2}),\ B_{3,1} = (\tfrac{1}{R_1} - \tfrac{1}{R_2}) + zB_{3,0},$$

$$B_{m,n} = -\tfrac{L^{n-1}}{m-2}(\tfrac{1}{R_2^{m-2}}, +\tfrac{(-1)^n}{R_1^{m-2}}) + \tfrac{n-1}{m-2}B_{m-2,n-2} + zB_{m,n-1} \text{ for } n \geq 2,$$

With $e = 1/\cosh\xi_o$ and $L_e = \log(\frac{1+e}{1-e})$, the constants α and β are defined as

$$\alpha = 2\beta\tfrac{e^2}{1-e^2} = 2U_b e^2[2e + (3e^2-1)L_e]^{-1}.$$

The pressure is expressed as

$$P(\mathbf{r}) = -\mu\alpha\frac{x}{r^2}(\frac{z-L}{R_2} - \frac{z+L}{R_1}).$$

For the full spheroid with surface velocity equal to $\Omega z\hat{\mathbf{x}}$, the velocity is expressed as

$$\mathbf{U}(\mathbf{r}) = \alpha_2 x[(2A_1+A_3)\hat{\mathbf{z}}+2(x\hat{\mathbf{x}}+y\hat{\mathbf{y}})B_{3,1}]+\gamma_2[2\hat{\mathbf{x}}B_{1,1}-\hat{\mathbf{z}}xA_3]+4\beta_2\nabla[x(L^2B_{3,1}-B_{3,3})],$$

with

$$A_1 = zB_{3,1} - B_{3,2}, A_3 = L^2B_{3,0} - B_{3,2}$$

$$\gamma_2 = \Omega[-2e + (1+e^2)L_e]^{-1}$$

$$\alpha_2 = e^2\gamma_2[-2e + (1-e^2)L_e][2e(2e^2-3) + 3(1-e^2)L_e]^{-1}$$

$$\beta_2 = \alpha_2(1-e^2)/(4e^2)$$

The pressure is expressed as

$$P(\mathbf{r}) = \alpha_2 \int_{-L}^{L} \frac{2(L^2 - z'^2)3x(z-z')}{\sqrt{x^2+y^2+(z-z')^2}^{5}} dz'.$$

The torque for this case is described by

$$T = \frac{-32}{3}\pi\mu \mathrm{L}^3\gamma_2\hat{\mathbf{y}}.$$

For the full spheroid with surface velocity equal to $-\Omega x\hat{\mathbf{z}}$, the velocity is expressed as

$$\mathbf{U}(\mathbf{r}) = \alpha_3 x[(2A_1+A_3)\hat{\mathbf{z}}+2(x\hat{\mathbf{x}}+y\hat{\mathbf{y}})B_{3,1}]+\gamma_3[2\hat{\mathbf{x}}B_{1,1}-\hat{\mathbf{z}}xA_3]+4\beta_3\nabla[x(L^2B_{3,1}-B_{3,3})],$$

with

$$\gamma_3 = \Omega(1-e^2)[-2e + (1+e^2)L_e]^{-1}$$

$$\alpha_3 = 2e^2\gamma_3[-2e + L_e][2e(2e^2-3) + 3(1-e^2)L_e]^{-1}$$

$$\beta_3 = \alpha_3(1-e^2)/(4e^2)$$

The pressure is expressed as

$$P(\mathbf{r}) = \alpha_3 \int_{-L}^{L} \frac{2(L^2 - z'^2)3x(z - z')}{\sqrt{x^2 + y^2 + (z - z')^2}^5} dz'.$$

The torque for this case is described by

$$T = \frac{-32}{3}\pi\mu \mathrm{L}^3\gamma_3\hat{\mathbf{y}}.$$

The exact solutions for oblate spheroids can be derived from the solutions for prolate spheroids by letting $\cosh\xi_o \rightarrow j\sinh\xi_o$, and $L \rightarrow -jL$.

4.8.2 Proof that the torque exerted by fluid on a surrounding surface is zero

We can represent the equation for Stokes flow in tensor form, i.e.,

$$\frac{\partial T_{ij}}{\partial x_j} = 0, \tag{4.29}$$

where

$$T_{ij} = -p\delta_{ij} + \mu(\frac{\partial u_j}{\partial x_i} + \frac{\partial u_i}{\partial x_j}).$$

Using the divergence theorem and Equation 4.29, we can show that the force exerted by the fluid on a surrounding surface is zero, i.e.,

$$F = \int_S T_{ij} n_j dS = \int_V \frac{\partial T_{ij}}{\partial x_j} dV = 0.$$

The torque exerted by the fluid on a surrounding surface can be represented as

$$T = \int_S \epsilon_{ijk} x_j T_{kl} n_l dS, \tag{4.30}$$

where ϵ_{ijk} is the well known "completely antisymmetric tensor",

$$\epsilon_{ijk} = \begin{cases} 1 & \text{if } ijk = 123,\ 312,\ 231 \\ -1 & \text{if } ijk = 213,\ 132,\ 321 \\ 0 & \text{otherwise.} \end{cases}$$

The divergence theorem can be applied to Equation 4.30 so that

$$T = \int_S \epsilon_{ijk} x_j T_{kl} n_l dS = \int_V \epsilon_{ijk} \frac{\partial}{\partial x_l}(x_j T_{kl}) dV.$$

Since

$$\epsilon_{ijk} \frac{\partial}{\partial x_l}(x_j T_{kl}) = \epsilon_{ijk} x_j \frac{\partial T_{kl}}{\partial x_l} + \epsilon_{ijk} T_{kl} \frac{\partial x_j}{\partial x_l},$$

and

$$\epsilon_{ijk} T_{kl} \frac{\partial x_j}{\partial x_l} = 0,$$

using Equation 4.29, we see that the torque exerted by the fluid on a surrounding surface is zero, i.e.,

$$T = \int_V \epsilon_{ijk} \frac{x_j \partial T_{kl}}{\partial x_l} dV = 0.$$

4.8.3 The use of Fourier analysis to derive the q' dependence of $\mathbf{f}_{fict}(\mathbf{r}')$

We express $\mathbf{f}_{fict}(\mathbf{r}')$ in a Fourier series given by 4.15. Equation 4.4, the pressure stokeslet, can be expressed in prolate spheroidal coordinates as

$$G_{px}(\xi,\eta,q,\xi',\eta',q') = \frac{(c_1(\xi,\eta)\cos q - c_1(\xi',\eta')(\cos q'' \cos q - \sin q'' \sin q))}{\sqrt{a(\xi,\eta,\xi',\eta') - b(\xi,\eta,\xi',\eta')\cos q''}^3}, \quad (4.31)$$

$$G_{py}(\xi,\eta,q,\xi',\eta',q') = \frac{(c_1(\xi,\eta)\sin q - c_1(\xi',\eta')(\cos q'' \sin q + \sin q'' \cos q))}{\sqrt{a(\xi,\eta,\xi',\eta') - b(\xi,\eta,\xi',\eta')\cos q''}^3}, \quad (4.32)$$

$$G_{pz}(\xi,\eta,q,\xi',\eta',q') = \frac{d(\xi,\eta,\xi',\eta')}{\sqrt{a(\xi,\eta,\xi',\eta') - b(\xi,\eta,\xi',\eta')\cos q''}^3}, \quad (4.33)$$

where

$$\begin{aligned}
q'' &= q' - q, \\
a(\xi,\eta,\xi',\eta') &= L^2(\cos^2\eta + \sinh^2\xi) + L'^2(\cos^2\eta' + \sinh^2\xi') - \\
&\quad 2LL'\cos\eta\cos\eta'\cosh\xi\cosh\xi', \\
b(\xi,\eta,\xi',\eta') &= 2LL'\sin\eta\sin\eta'\sinh\xi\sinh\xi', \\
c_1(\xi,\eta) &= L\sinh\xi\sin\eta, \\
d(\xi,\eta,\xi',\eta') &= L\cosh\xi\cos\eta - L'\cosh\xi'\cos\eta'.
\end{aligned}$$

By substituting Equation 4.15 into Equation 4.6, the expressions for the pressure due to impulses in the x, y and z directions can be written as,

$$\begin{aligned}
P_x(\mathbf{r}) = \int_0^{\pi} h_1(\xi',\eta')d\eta' \int_0^{2\pi} h_2(\xi',\eta')dq' G_{px}(\xi,\eta,q,\xi',\eta',q') \times \\
\sum_{j=0}^{\infty}(\tilde{a}_{xj}(\eta')\cos(jq') + \tilde{b}_{xj}(\eta')\sin(jq')),
\end{aligned} \tag{4.34}$$

$$\begin{aligned}
P_y(\mathbf{r}) = \int_0^{\pi} h_1(\xi',\eta')d\eta' \int_0^{2\pi} h_2(\xi',\eta')dq' G_{py}(\xi,\eta,q,\xi',\eta',q') \times \\
\sum_{j=0}^{\infty}(\tilde{a}_{yj}(\eta')\cos(jq') + \tilde{b}_{yj}(\eta')\sin(jq')),
\end{aligned} \tag{4.35}$$

$$\begin{aligned}
P_z(\mathbf{r}) = \int_0^{\pi} h_1(\xi',\eta')d\eta' \int_0^{2\pi} h_2(\xi',\eta')dq' G_{pz}(\xi,\eta,q,\xi',\eta',q') \times \\
\sum_{j=0}^{\infty}(\tilde{a}_{zj}(\eta')\cos(jq') + \tilde{b}_{zj}(\eta')\sin(jq')),
\end{aligned} \tag{4.36}$$

with $G_{px}(\xi,\eta,q,\xi',\eta',q')$, $G_{py}(\xi,\eta,q,\xi',\eta',q')$, and $G_{pz}(\xi,\eta,q,\xi',\eta',q')$ given by Equations 4.31-4.33, and $h_1(\xi',\eta')$ and $h_2(\xi',\eta')$, the metric coefficients for prolate spheroidal coordinates,

$$h_1(\xi',\eta') = L'\sqrt{\sin^2\eta' + \sinh^2\xi'},$$

$$h_2(\xi', \eta') = L' \sin\eta' \sinh\xi'.$$

With $q' = q'' + q$, $\cos q' = \cos q'' \cos q - \sin q'' \sin q$, and $\sin q' = \sin q'' \cos q + \cos q'' \sin q$, Equations 4.34-4.36 can be expressed as,

$$P_x(\mathbf{r}) = \int_0^\pi h_1(\xi', \eta') d\eta' \int_0^{2\pi} h_2(\xi', \eta') dq'' G_{px}(\xi, \eta, q, \xi', \eta', q') \times$$
$$\sum_{j=0}^{\infty} (\tilde{a}_{xj}(\eta')(\cos jq'' \cos jq - \sin jq'' \sin jq) + \tilde{b}_{xj}(\eta')(\sin jq'' \cos jq + \cos jq'' \sin jq)),$$

$$P_y(\mathbf{r}) = \int_0^\pi h_1(\xi', \eta') d\eta' \int_0^{2\pi} h_2(\xi', \eta') dq'' G_{py}(\xi, \eta, q, \xi', \eta', q') \times$$
$$\sum_{j=0}^{\infty} (\tilde{a}_{yj}(\eta')(\cos jq'' \cos jq - \sin jq'' \sin jq) + \tilde{b}_{yj}(\eta')(\sin jq'' \cos jq + \cos jq'' \sin jq)),$$

$$P_z(\mathbf{r}) = \int_0^\pi h_1(\xi', \eta') d\eta' \int_0^{2\pi} h_2(\xi', \eta') dq'' G_{pz}(\xi, \eta, q, \xi', \eta', q') \times$$
$$\sum_{j=0}^{\infty} (\tilde{a}_{zj}(\eta')(\cos jq'' \cos jq - \sin jq'' \sin jq) + \tilde{b}_{zj}(\eta')(\sin jq'' \cos jq + \cos jq'' \sin jq)),$$

Since q' is integrated over a full period of 2π, the integration can equally be performed over a full period in q''.

By substituting Equations 4.31-4.33 into the above expressions for $P_x(\mathbf{r})$, $P_y(\mathbf{r})$, and $P_z(\mathbf{r})$ and performing the integrations over a full period of q'', we can determine which terms will give only a $\cos q$ dependence. Note that odd functions of q'' integrate to zero. One possible term is the $\tilde{a}_{x0}(\eta')$ term. Two other possible terms are $\tilde{a}_{x2}(\eta') \cos 2q'$ and $\tilde{b}_{y2}(\eta') \sin 2q'$ if $\tilde{a}_{x2}(\eta') = \tilde{b}_{y2}(\eta')$. The only other term possible is $\tilde{a}_{z1}(\eta') \cos q'$. Therefore, $\mathbf{f}_{fict}(\eta', q')$ can be expressed as,

$$f_{fict,x}(\eta', q') = \tilde{a}_{x0}(\eta') + \tilde{a}_{x2}(\eta') \cos 2q', \tag{4.37}$$

$$f_{fict,y}(\eta', q') = \tilde{a}_{x2}(\eta') \sin 2q', \tag{4.38}$$

$$f_{fict,z}(\eta', q') = \tilde{a}_{z1}(\eta') \cos q'. \tag{4.39}$$

Equations 4.37-4.39 are consistent with those found elsewhere (Haber, 1995), and also give the correct q dependence of the velocities expressed in Equations 4.12-4.14.

To facilitate the analytic integration in q', we will use equivalent representions of Equations 4.37-4.39, given in Equation 4.16-Equation 4.18.

4.8.4 Torque due to fluid velocity, $z\hat{\mathbf{x}}$

The torque due to shear on the hemispheroid can be expressed as

$$T_y = \int_S (zF_x - xF_z)dS,$$

with F_{x_i} as

$$F_{x_i} = \mu(\frac{\partial U_{x_i}}{\partial x_j} + \frac{\partial U_{x_j}}{\partial x_i})n_j.$$

For $U = z\hat{\mathbf{x}}$, $F_x = \mu n_z$ and $F_z = \mu n_x$. In prolate spheroidal coordinates, $n_z = \sinh\xi \cos\eta / \sqrt{\sinh^2\xi + \sin^2\eta}$, and $n_x = \cosh\xi \sin\eta \cos q / \sqrt{\sinh^2\xi + \sin^2\eta}$, and integrating around the hemispheroidal surface,

$$\begin{aligned} T_y &= \int_0^{\frac{\pi}{2}} \int_0^{2\pi} d\eta dq \mu L^3 \sinh^2\xi_o \sin\eta \cosh\xi_o (\cos^2\eta - \sin^2\eta\cos^2 q) \\ &= 0. \end{aligned}$$

Chapter 5

Conclusions

5.1 Introduction

In this section, we will first study the frequency response of the hair bundle sensitivity transfer function $H_\mu(f) = \Theta/U_b$ as a function of shape and size. We will also compare our results to those obtained in a previous 2-D study (Freeman and Weiss, 1990a). We will see that the 2-D flap best represents the hydrodynamics of an infinitesmally thin prolate hemispheroid although, for low frequencies, the 2-D flap model can not predict the spacing between sensitivity curves for hair bundles with different heights. We will discuss differences in the sizes of hair bundles of vestibular organs and auditory organs, and how these differences can be qualitatively predicted by our results. Lastly, we will use our hair bundle model in a broader model of ear physiology that includes the effects of the middle ear and quantitatively compare our predictions of the low frequency and high frequency regions of sensitivity curves to experimental measurements.

5.2 Comparison of low and high frequency solution

5.2.1 The sensitivity transfer function $H_\mu(f) = \Theta/U_b$

A linear network that represents both mechanical and hydrodynamic torques on the body is illustrated in Figure 2-3. We will assume the mass of the hair bundle is zero—for asymptotically low frequencies this assumption makes sense since the terms in the transfer function due to the inertia approach zero as $f \rightarrow 0$. We will discuss the effects of the inertia of the hemispheroid at high frequencies in the next section, but we will see that for the anatomically relevant shapes, the effects of inertia are small. With this approximation, the transfer function $H_\mu(f) = \Theta/U_b$ given by Equation 2.7 is equal to

$$H_\mu(f) = \Theta/U_b = \frac{H_b}{1/C + j(2\pi f)Z_r}, \tag{5.1}$$

where

$$H_b = \frac{T_t}{U_b},$$

$$Z_r = \frac{T_r}{j(2\pi f)\Theta},$$

and C is the hinge compliance. In the limit of low frequencies, Equation 5.1 can be expressed as

$$H_\mu(f) = \Theta/U_b = C\sqrt{j(2\pi f)\rho\mu}h^3 T_{tn}(\xi_o), \tag{5.2}$$

where $T_{tn}(\xi_o)$ is illustrated in Figure 4-40. In the limit of high frequencies, Equation 5.1 is given by

$$H_\mu(f) = \Theta/U_b = \frac{T_t}{U_b} / \frac{T_r}{j(2\pi f)\Theta}. \tag{5.3}$$

From Equation 3.26, Equation 3.27, Equation 3.28, Equation 3.29, we can approximate Equation 5.3 for all shapes as

$$H_\mu(f) = \Theta/U_b = \frac{2.3h}{L^2 j(2\pi f)}. \tag{5.4}$$

$H_\mu(f)$ for both low and high frequencies is illustrated in the top panels of Figure 5-1 for prolate, oblate, and hemispherical shapes for a fixed height. We see that as the shape changes from prolate to hemispherical the frequency at which the asymptotes cross first slightly decreases and then greatly increases. As the shape changes from oblate to hemispherical, the frequency at which the asymptotes cross increases greatly. This large increase in crossover frequency as the shape approaches hemispherical results from the large increase in $H_\mu(f)$ for high frequencies; as the shape approaches hemispherical, for fixed height, L approaches zero so that the high frequency $H_\mu(f)$ approaches infinity (Equation 5.4). Figure 5-2 illustrates, for a prolate hemispheroid, the high-frequency and low-frequency $H_\mu(f)$ for three different heights. We see that as the height increases, the cross-over frequency decreases because the low-frequency $H_\mu(f)$ increases while the high-frequency $H_\mu(f)$ decreases. We also observe that height has a much larger effect on $H_\mu(f)$ for low frequencies than high frequencies.

5.3 Effects of inertia at high frequencies

For high frequencies, the effects of the inertia of the hemispheroid can be important. If the mass of the hemispheroid is assumed to be nonzero, we can express $H_\mu(f)$ for high frequencies as

$$H_\mu(f) = \frac{\frac{T_{t,hf}}{U_h} + j(2\pi f)\frac{3}{8}hM}{\frac{T_{r,hf}}{\Theta} - (2\pi f)^2\frac{L^2}{5}(\sinh^2\xi_o + \cosh^2\xi_o)M},$$

where M is the mass of the hemispheroid. The term $(2\pi f)^2L^2/5(\sinh^2\xi_o + \cosh^2\xi_o)M$ represents the moment of inertia of the hemispheroid, i.e.,

$$j(2\pi f)\Theta\rho\int_S r^2 dV = j(2\pi f)\Theta\frac{L^2}{5}(\sinh^2\xi_o + \cosh^2\xi_o)M.$$

The term $(j(2\pi f)3h/8)M$ represents the effects of the accelerating reference frame; the angular momentum due to the accelerating reference frame is equal to the product of the center of mass ($3h/8$ for hemispheroids) and the linear momentum.

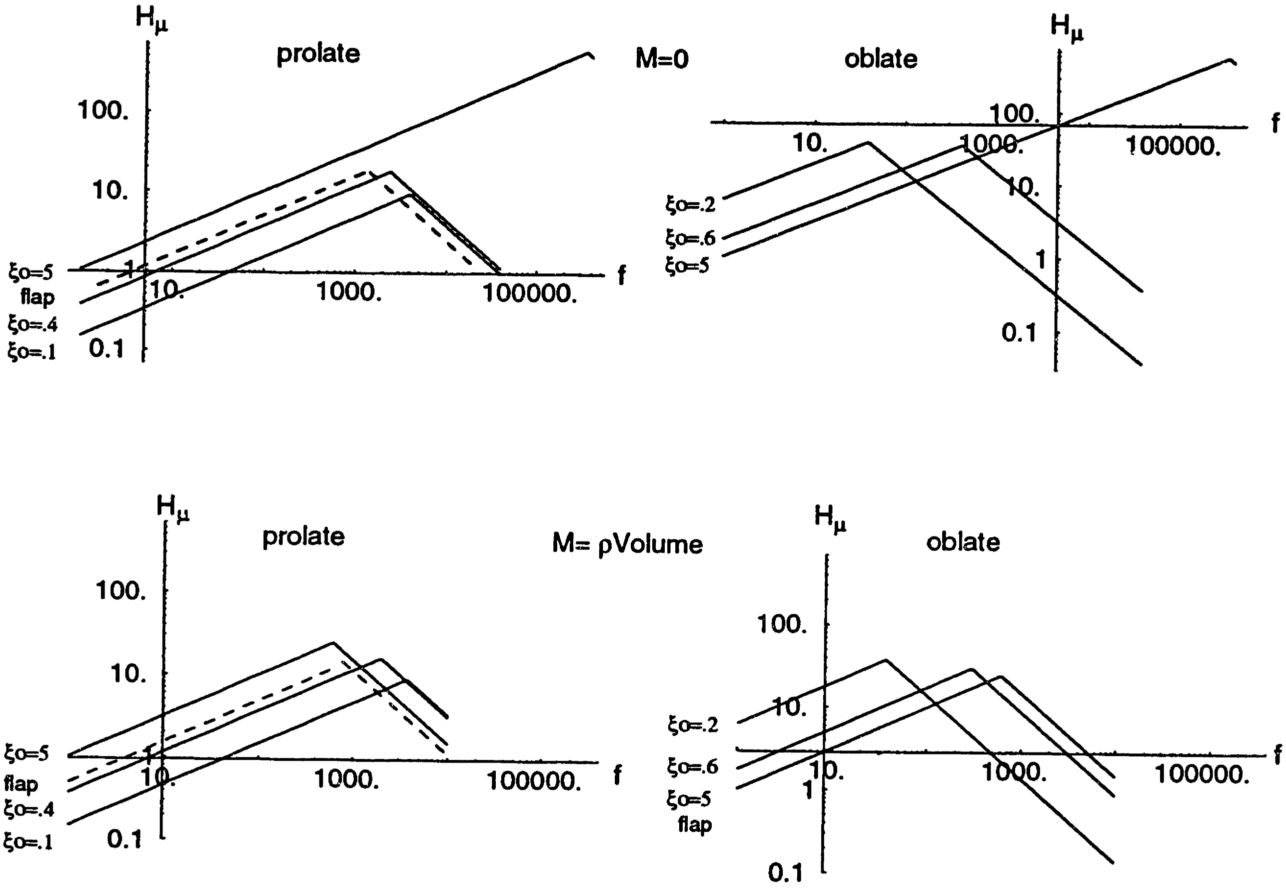

Figure 5-1: Frequency responses for bodies of equal height but different shapes.
Top panels: massless bodies of equal height but different shapes. Bottom panels: neutrally bouyant bodies of equal height but different shapes, $M = \rho\frac{2}{3}\pi h w^2$ for the hemispheroids, and $M_z = \rho h^2$ for the 2-D flap.
For all panels, $h = 10\mu m$, and $C = 4.95 * 10^{13} rad/N - m$. The compliance was chosen so that the massless hemispheroid, $\xi_o = .1$, has a cross-over frequency of 4 kHz. Also shown are the results for the 2-D flap, with $C_z = C * 10^{-5} rad/N$.
Left panels: $H_\mu(f)$ for both low and high frequencies prolate hemispheroids, $\xi_o = .1$, $\xi_o = .4$, and a nearly hemispherical hemispheroid, $\xi_o = 5$.
Right panels: $H_\mu(f)$ for both low and high frequencies oblate hemispheroids, $\xi_o = .2$, $\xi_o = .6$, and a nearly hemispherical hemispheroid, $\xi_o = 5$.

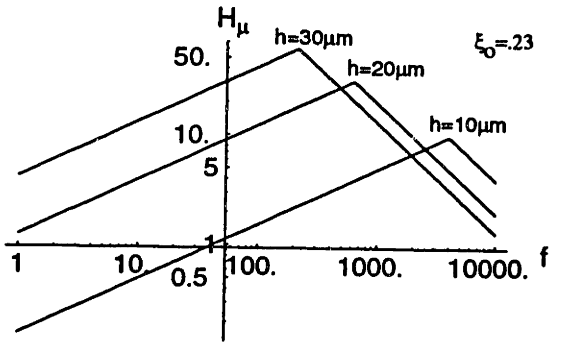

Figure 5-2: $H_\mu(f)$ for both low and high frequencies for a prolate hemispheroid with $\xi_o = .23$, for three different heights, $h = 10\mu m$, $h = 20\mu m$, $h = 30\mu m$ with $C = 3.05 * 10^{13} rad/N - m$, and $M = 0$. The compliance was chosen so that the hemispheroid with $h = 10\mu$m, has a cross-over frequency of 4 kHz.

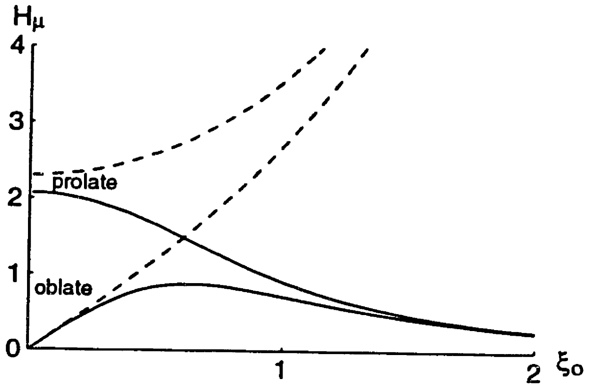

Figure 5-3: $H_\mu(f)$ for high frequencies, plotted for $M = 0$ (dashed lines), and $M = \rho\frac{2}{3}\pi h w^2$ (solid) with $L = 1$.

Let us estimate the effects of inertia by comparing massless and neutrally bouyant bodies. Let the mass density of the hemispheroid be equal to ρ, the mass density of the fluid, so that $M = \rho\frac{2}{3}h\pi w^2$ ($\frac{2}{3}\pi h w^2$ is the volume of the hemispheroid). The effect of the inertia can be seen in Figure 5-3. For prolate, and oblate shapes, ($\xi_o < .6$), the effects of the inertia of the hemispheroid are minimal. As the shape becomes hemispherical, the inertia of the hemispheroid dominates $H_\mu(f)$. These results can also be seen by comparing the bottom panels of Figure 5-1, which illustrate $H_\mu(f)$ for $M = \rho\frac{2}{3}\pi h w^2$ to the top panels of Figure 5-1 which illustrate $H_\mu(f)$ for $M = 0$. The largest difference in these curves occurs for the shapes that approach hemispherical.

Since hair bundles are more often eccentric in shape, the effects of the inertia are small, and we will assume it to be zero for the rest of this chapter.

5.4 Comparison to 2-D study

To compare our results to those of (Freeman and Weiss, 1990a), we will first study the ratio, H_b/Z_r because this parameter has the same dimensions in both 3-D and

2-D. For low frequencies,

$$H_b/Z_r = (H_{bn}/Z_{rn})\sqrt{\frac{j(2\pi f)\rho}{\mu}} \tag{5.5}$$

for prolate hemispheroids and

$$H_b/Z_r = (H_{bn}/Z_{rn})(\frac{h}{w})^2\sqrt{\frac{j(2\pi f)\rho}{\mu}}$$

for oblate. H_{bn} and Z_{rn} are proportional to the curves of Figure 4-40, and their ratio is unity for the infinitemally thin prolate hemispheroid, and close to 1/3 for shapes that range from hemispheres to wide oblate hemispheroids. Figure 5-4 (left fourth panel from bottom) illustrates this ratio.

For low frequencies, for 2-D (Freeman and Weiss, 1990a),

$$H_b/Z_r = \sqrt{\frac{j(2\pi f)\rho}{\mu}}. \tag{5.6}$$

Since, for the infinitesmally thin prolate hemispheroid, Equation 5.5 is equal to Equation 5.6, the hydrodynamics of an infinitesmally thin prolate hemispheroid most resembles that of a 2-D flap for low frequencies.

We can also compare our results with the 2-D sensitivity transfer function $H_\mu(f)$,

$$H_\mu(f) = C_z 3.954 h^2\sqrt{j(2\pi f)\rho\mu}, \tag{5.7}$$

where C_z is a 2-D compliance. Note that in 2-D, $H_\mu(f)$ is proportional to h^2, whereas in 3-D, $H_\mu(f)$ is proportional to h^3, so we see that the 2-D analysis can not adequately model the shape dependence of $H_\mu(f)$. We can roughly compare Equation 5.2 with Equation 5.7, by approximating C_z by the compliance multiplied by the approximate spacing between hair bundles in a row ($\sim$ 10μm) so that $C_z = C * 10^{-5} rad - N$ (Freeman and Weiss, 1990a). Equation 5.7 is plotted in Figure 5-1 and we see that, even with this rough comparison, the 2-D flap represents the hydrodynamics of a prolate hemispheroid.

For high frequencies, in 3-D, H_b/Z_r can be approximated as

$$H_b/Z_r = \frac{2.3h}{L^2},$$

and for 2-D, this ratio is represented by

$$H_b/Z_r = \frac{2.1}{h}.$$

Although these ratios can not be equivalent for any hemispheroidal shape, they are closest (within 10 %) for the infinitesmally thin prolate hemispheroid. Also, $H_\mu(f)$ of the 2-D model is closest to that of the infinitesmally thin prolate hemispheroid. $H_\mu(f)$ for high frequencies for the 2-D flap is given by

$$H_\mu(f) = \frac{2.1}{hj(2\pi f)},$$

and is plotted in Figure 5-1 (top panels).

Thus we see that for all frequencies, a 2-D model best approximates the hydrodynamics of an infinitesmally thin prolate hemispheroid. Figure 5-4 summarizes the results of this section. The first column indicates the results (H_b, Z_r, H_b/Z_r, Θ/U_b) for low frequencies and the second column summarizes the same results for high frequencies. 2-D results are also indicated.

5.5 Comparison of hair bundles in auditory organs and vestibular organs

Equation 5.2 can be used to give insight into the difference in hair bundle height of hair cells in vestibular organs and auditory organs. Hair cells in auditory organs operate over a frequency range between 20 and 20,000 Hz, and have hair bundles with heights that range from .8 to 30 μm. Hair cells in vestibular organs operate at frequencies that are often much less than 1 Hz. For low frequencies, $H_\mu(f)$ (Equation 5.2) is extremely sensitive to hair bundle height; it is proportional to $\sqrt{f}h^3$. If we let the

		Low frequency		High frequency
H_b	3-D	$H_b = H_{bn} h^3 (j\omega\rho\mu)^{1/2}$ lines: full spheroid 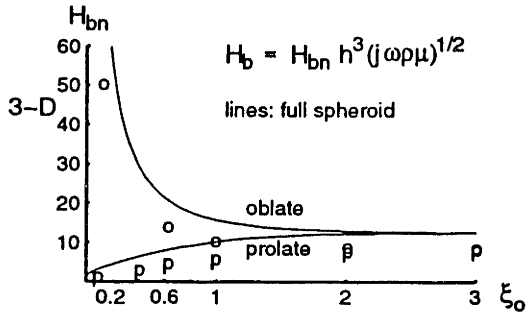 	3-D	$H_b = H_{bn}(j\omega\rho L^2 wh\, \pi/4)$ 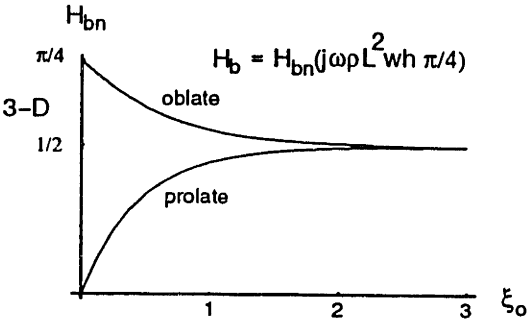
	2-D	$H_{bz} = 3.954\, h^2\, (j\omega\rho\mu)^{1/2}$	2-D	$H_{bz} = 2/3\, j\, h^3 \omega\rho$
Z_r	3-D	$Z_r = \begin{matrix} Z_m h^3 \mu j\omega \text{ (prolate)} \\ Z_m h w^2 \mu j\omega \text{ (oblate)} \end{matrix}$ lines: full spheroid 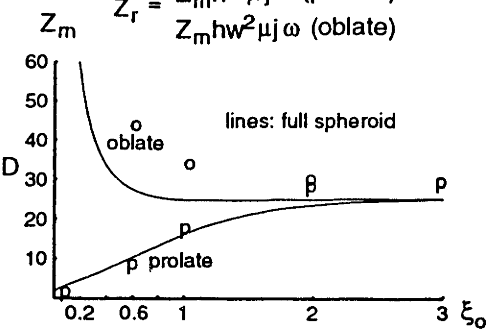 	3-D	$Z_r = Z_m(\omega^2 \rho L^4 w\, \pi)$ 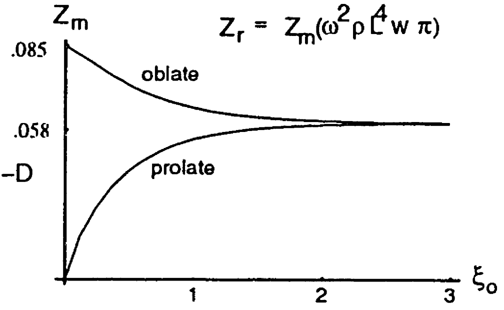
	2-D	$Z_{rz} = 3.954\, h^2 \mu j\omega$	2-D	$Z_{rz} = j\, h^4 \omega\rho/\pi$
$\frac{H_b}{Z_r}$	3-D	$H_b/Z_r = \begin{matrix} (H_b/Z_r)_n (j\omega\rho/\mu)^{1/2} \text{ prolate} \\ (H_b/Z_r)_n (j\omega\rho/\mu)^{1/2} (w/h)^2 \text{ oblate} \end{matrix}$ 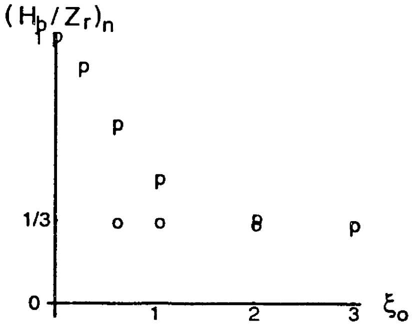 	3-D	$H_b/Z_r = 2.3\, h/L^2$
	2-D	$H_{bz}/Z_{rz} = (j\omega\rho/\mu)^{1/2}$	2-D	$H_{bz}/Z_{rz} = 2.1/h$
$\frac{\vartheta}{U_b}$	3-D	$\vartheta/U_b = C\, H_{bn}\, h^3 (j\omega\rho\mu)^{1/2}$	3-D	$\vartheta/U_b = 2.3\, h/L^2\, 1/j\omega$
	2-D	$\vartheta/U_b = C_z\, 3.954\, h^2 (j\omega\rho\mu)^{1/2}$	2-D	$\vartheta/U_b = 2.1/h\ 1/\rho$

Figure 5-4: Summary of results

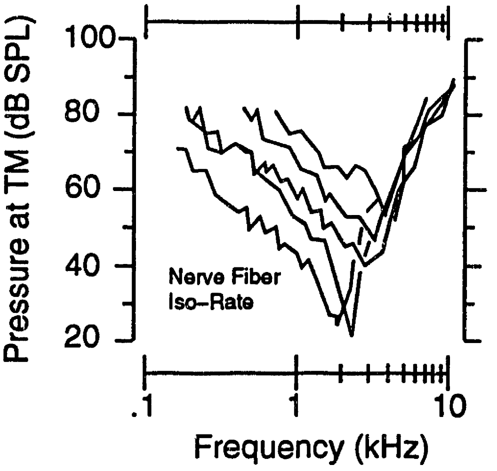

Figure 5-5: Neural sensitivity curves for five neurons.

hair bundle height increase by one order of magnitude, then to keep $H_\mu(f)$ constant, the frequency must decrease by six orders of magnitude. Hair bundles heights of vestibular organs can be one order of magnitude larger, and are often two orders of magnitude larger, than those of auditory organs. This increase in height is needed so that the hair bundles of vestibular organs can operate at low frequencies.

5.6 Neural tuning curves

The iso-DC voltage contour of a neural tuning curve, $P^{V_o}(f)$ describes the magnitude of the pressure applied at the tympanic membrane that results in a threshold rate of nerve fiber firings. Figure 5-5 illustrates neural sensitivity curves for five neurons from the cochlea of the alligator lizard. These neural sensitivity curves, which were obtained from neurons that innervate the free-standing region of the basilar papilla, are believed to result from the effects of the middle ear, the effects of the hair bundle motion, and perhaps the transduction process (Weiss and Leong, 1985). Our aim in this section is to compare a predicted sensitivity curve to a measured one.

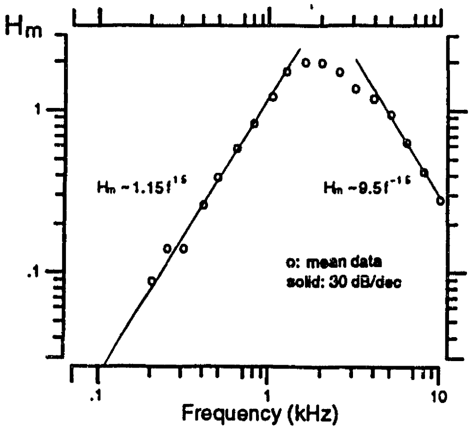

Figure 5-6: Measurements of the middle ear transfer function.

5.6.1 The model

$P_o^V(f)$ was modelled in (Weiss and Leong, 1985) as

$$P^{V_o}(f) = \frac{K(V_o)}{|H_m(f)H_\mu(f)H_a(f)|}, \tag{5.8}$$

where $H_m(f)$ is the middle ear transfer function, which relates pressure at the tympanic membrane to basilar membrane velocity,

$$H_m(f) = \frac{U_b}{P_T}.$$

$H_a(f)$ is an additional lowpass filter,

$$H_a(f) = \frac{K_a}{1 + j2\pi f/f_o}.$$

The source of this additional lowpass filter is unknown but may come from the transduction process (Weiss and Leong, 1985).

Measurements of the middle ear transfer function are illustrated in Figure 5-6 from (Rosowski et al., 1985). For low frequencies ($< 1000Hz$), we have modelled $H_m(f)$ by the curve $1.5(f/1000)^{3/2}$. For high frequencies ($> 4000Hz$), $H_m(f)$ is modelled by by the curve $9.5(f/1000)^{-3/2}$.

In the limit of low frequencies, we substitute Equation 5.2 into Equation 5.8 to obtain

$$P^{V_o}(f) = \frac{K(V_o)}{1.5(f/1000)^{1.5} C\sqrt{2\pi f \rho \mu} h^3 T_{tn}(\xi_o) K_a}, \tag{5.9}$$

and, in the limit of high frequencies, we substitute Equation 5.3 so that Equation 5.8 can be expressed as

$$P^{V_o}(f) = \frac{K(V_o)(2\pi f)^2 L^2 (f/1000)^{1.5}}{f_o 2.3 h 9.5 K_a}. \tag{5.10}$$

We chose to compute Equation 5.9 and Equation 5.10 for hair bundles of the same shape. Results from the free-standing region of the basillar papilla of alligator lizard (Mulroy and Williams, 1987) indicate that the membrane surface area of the hair bundles are proportional to height which would imply that the square of the width of the hair bundle is proportional to its height. Since the height changes by a factor of three, the width changes by a factor of 1.7, which suggests that the shape changes but not by very much. Moreover, in the bobtail lizard, it is known that as the height increases, the number of hairs increase (Koppl, 1988) which also suggest that for lizards, the shape of the hair bundle is more or less fixed. Equation 5.9 and Equation 5.10 are plotted for hair bundles of the same shape on top of the neural sensitivity curves in Figure 5-7. We let $f_o = 7CL^2T_{tn}(\xi_o)$, and $K_a = 3.2910^{13}K_o/(CT_{tn}(\xi_o))$so as to best match the curve tuned to 4 kHz. Although the heights of the hair bundles to which the nerve fibers synapse are unknown, the chosen values are physiologically plausible (Mulroy, 1974). Note that for the chosen values of f_o and K_a, these curves are independent of K_o, C, $T_{tn}(\xi_o)$, and L, and only depend on height.

The match between the model and the data is striking. The model does very well at predicting the spacing between the curves for low frequencies, and predicts that the spacing between the curves at high frequencies will be less. Note that the 2-D model can not predict the spacing between curves at low frequencies— if we set the parameters of the 2-D model so that, for $h = 10\mu$m, it matches the curve most sensitive to 4 kHz (and the 3-D model), then, for $h = 52\mu$m, the 2-D model matches the lowest sensitivity curve; the 3-D model matches the lowest sensitivity curve with the more physiologically relevant height of 30 μm.

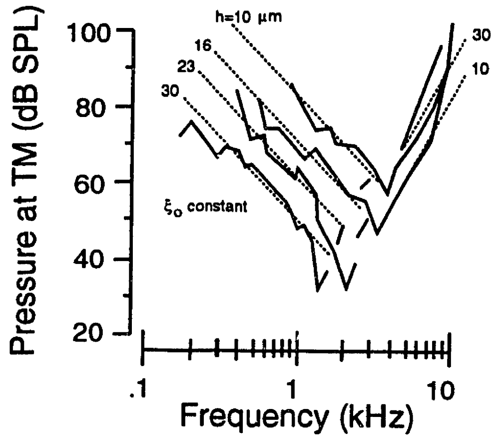

Figure 5-7: Neural sensitivity curves and plots of Equation 5.9 and Equation 5.10 for hemispheroids of the same shape with values chosen to best match the data.

If the width remained fixed the shape would change, and hemispheroids with $h > 10\mu$m would be more prolate than the hemispheroids with $h = 10\mu$m. For a fixed shape, we know from dimensional analysis that the normalized torque (the torque divided by the height cubed) for hemispheroids of all heights remains the same. For a fixed width, the normalized torque decreases as the shape becomes more prolate (see Figure 4-40). This implies that taller hair bundles would be needed to achieve the required spacing between tuning curves. For example, if we chose $h = L\cosh\xi_o = 10\mu$m to match the curve which is most sensitive at 4 kHz and if we chose $w = L\sinh\xi_o = 2.3\mu$m for each curve, then a hemispheroid with $h = 36\mu$m would match the lowest sensitivity curve in Figure 5-7.

If we let the square of the width scale with height so that taller hair bundles are somewhat more prolate than shorter hair bundles, and if we assume a physiological relevent width of $w = 2.3\mu$m for the highest curve with $h = 10\mu$m, then the lowest curve would be obtained with a height of 32μm, which is close to the 30μm result we obtained for hemispheroids of the same height.

5.7 Summary

We compared the results of the 2-D flap model to our 3-D hemispheroid model. For low and high frequencies, the 2-D flap represented the hydrodynamics of an infinitesmally thin prolate hemispheroid. However, for low frequencies, the 2-D flap model, cannot predict the spacing between neural sensitivity curves at low frequencies since for 2-D, $H_\mu(f) \propto h^2\sqrt{f}$ whereas for 3-D, $H_\mu(f) \propto h^3\sqrt{f}$.

We studied the effects of inertia on the hair bundle transfer function $H_\mu(f)$. We found that for eccentric shapes, the effects were small, but increased as the shape became hemispherical. Since hair bundles are not hemispherical in shape, we believe the effects of inertia on hair bundle motion are not significant.

We determined that for hemispheroids of the same shape, for low frequencies, $H_\mu(f) \propto h^3\sqrt{f}$, and for high frequencies, $H_\mu(f) \propto 1/(hf)$. The effect of width on $H_\mu(f)$ is much less important than the effect of height for low and high frequencies.

The low frequency results qualitatively predicted the difference in height between hair bundles in vestibular organs and those of auditory organs. Two hemispheroids whose heights differ by one order of magnitude, will have frequency responses that differ by six orders of magnitude. Hair cells in vestibular organs can operate in frequencies that are six orders of magnitude lower than those of auditory organs, and the heights of hair bundles in vestibular organs can be one order of magnitude large than those of auditory organs.

Our results also predicted the characteristics of neural sensitivity curves of the free-standing region of the basilar papilla of the alligator lizard. For low frequencies, there is a large increase in sensitivity when the hair bundle height is increased; for high frequencies the influence of height is much less. With realistic values of hair bundle sizes, an excellent match between the neural sensitivity curves of four neurons and our model was obtained. These results suggest that it is the change in hair bundle height that accounts for the differences in frequency responses in hair cells for low and high frequencies.

Bibliography

Abramowitz, M. and Stegun, I. (1964). *Handbook of Mathematical Functions with Formulas,Graphs, and Mathematical Tables.* Jon Wiley and Sons, New York, 10th edition.

Batchelor, G. K. (1967). *An Introduction to Fluid Dynamics.* Cambridge Univ. Press, London.

Becker, A. A. (1992). *The Boundary Element Method in Engineering-a Complete Course.* McGraw-Hill Book Company, London, 1st edition.

Blake, J. (1971). A note on the image system for a stokeslet in a no-slip boundary. *Proceedings of the Cambridge Philosophical Society*, 70:303–310.

Brenner, H. (1995). Personal communication.

Brownell, W. E., Bader, C. R., Bertrand, D., and de Ribaupierre, Y. (1985). Evoked mechanical responses of isolated cochlear outer hair cells. *Science*, 227:194–196.

Chwang, A. T. and Wu, T. Y. (1975). Hydromechanics of low-reynolds-number flow. part 2. singularity method for stokes flows. *J. Fluid Mech.*, 67:787–815.

Dean, W. R. and O'Neill, M. E. (1963). A slow motion of viscous liquid caused by the rotation of a solid sphere. *Mathematika*, 10:13–24.

Eatock, R. A., Saeki, M., and Hutzler, M. J. (1993). Electrical resonance of isolated hair cells does not account for acoustic tuning in the free-standing region of the alligator lizard's cochlea. *J. Neurosci.*, 13:1767–1783.

Freeman, D., Hendrix, D., Shah, D., Fan, L., and Weiss, T. (1993). Effect of lymph composition on an in vitro preparation of the alligator lizard cochlea. *Hearing Res.*, 65:83–98.

Freeman, D. M. (1990). Anatomical model of the cochlea of the alligator lizard. *Hearing Res.*, 49:29–38.

Freeman, D. M. and Weiss, T. F. (1988). The role of fluid inertia in mechanical stimulation of hair cells. *Hearing Res.*, 35:201–207.

Freeman, D. M. and Weiss, T. F. (1990a). Hydrodynamic analysis of a two-dimensional model for micromechanical resonance of free-standing hair bundles. *Hearing Res.*, 48:37–68.

Freeman, D. M. and Weiss, T. F. (1990b). Hydrodynamic forces on hair bundles at high frequencies. *Hearing Res.*, 48:31–36.

Freeman, D. M. and Weiss, T. F. (1990c). Hydrodynamic forces on hair bundles at low frequencies. *Hearing Res.*, 48:17–30.

Freeman, D. M. and Weiss, T. F. (1990d). Superposition of hydrodynamic forces on a hair bundle. *Hearing Res.*, 48:1–16.

Frishkopf, L. S. and DeRosier, D. J. (1983). Mechanical tuning of free-standing stereociliary bundles and frequency analysis in the alligator lizard cochlea. *Hearing Res.*, 12:393–404.

Geisler, C. D. and Sang, C. (1995). A cochlear model using feed-forward outer-hair-cell forces. *Hearing Research*, 86:132–146.

Haber, S. (1995). Personal communication.

Holton, T. and Hudspeth, A. J. (1983). A micromechanical contribution to cochlear tuning and tonotopic organization. *Science*, 222:508–510.

Holton, T. and Weiss, T. F. (1983a). Frequency selectivity of hair cells and nerve fibres in the alligator lizard cochlea. *J. Physiol.*, 345:241–260.

Holton, T. and Weiss, T. F. (1983b). Receptor potentials of lizard cochlear hair cells with free-standing stereocilia in response to tones. *J. Physiol.*, 345:205–240.

Hubbard, A. (1993). A traveling-wave amplifier model of the cochlea. *Science*, 259:68–70.

Khanna, S. M. and Leonard, D. G. B. (1982). Basilar membrane tuning in the cat cochlea. *Science*, 215:305–306.

Koppl, C. (1988). Morphology of the basilar papilla of the bobtail lizard tiliqua rugosa. *Hearing Research*, 35:209–228.

Landau, L. D. and Lifshitz, E. M. (1959). *Fluid Mechanics.* Pergamon Press, Elmsford, New York.

Lewis, E. R., Leverenz, E. L., and Bialek, W. S. (1985). *The Vertebrate Inner Ear.* C.R.C. Press, Boca Raton, Fl.

Moon, P. and Spencer, D. (1971). *Field Theory Handbook.* Springer-Verlag, Berlin, 2nd edition.

Morse, P. and Feshbach, H. (1953). *Methods of Theoretical Physics.* McGraw-Hill, New York, 1st edition.

Mulroy, M. J. (1974). Cochlear anatomy of the alligator lizard. *Brain Behav. Evol.*, 10:69–87.

Mulroy, M. J. and Williams, R. S. (1987). Auditory stereocilia in the alligator lizard. *Hearing Res.*, 25:11–21.

Neely, S. T. (1993). A model of cochlear mechanics with outer hair cell motility. *J. Acoust. Soc. Am.*, 94(1):137–146.

Pickles, J. O. (1988). *An Introduction to the Physiology of Hearing.* Academic Press, San Diego, CA, second edition.

Pozrikidis, C. (1989). A study of linearized oscillatory flow past particles by the boundary integral method. *Journal of Fluid Mechanics*, 202:17–41.

Pozrikidis, C. (1992). *Boundary integral and singularity methods for linearized viscous flow.* Cambridge University Press, Cambridge, England.

Prudnikov, Brychkov, M. (1986). *Integrals and Series, Vol.3.* Gordon and Breach, New York.

Rhode, W. S. (1971). Observations on the vibration of the basilar membrane in squirrel monkeys using the mossbauer technique. *J. Acoust. Soc. Am.*, 49:1218–1231.

Rosowski, J. J., Peake, W. T., Lynch, T. J., Leong, R., and Weiss, T. F. (1985). A model for signal transmission in an ear having hair cells with free-standing stereocilia: II. macromechanical stage. *Hearing Res.*, 20:139–155.

Siebert, W. M. (1974). Ranke revisited- a simple short-wave cochlear model. *J. Acoust. Soc. Am.*, 56:594–600.

Steele, C. R. and Taber, L. A. (1978). Comparison of wkb and finite difference calculations for a two-dimensional cochlear model. *J. Acoust. Soc. Am.*, 65(4):1001–1006.

Vater, M. and Lenoir, M. (1992). Ultrastructure of the horseshoe bat's organ of corti scanning electron microscopy. *Journal of Comparative Neurology*, 318:367–379.

Weiss, T. F. and Leong, R. (1985). A model for signal transmission in an ear having hair cells with free-standing stereocilia: III. Micromechanical stage. *Hearing Res.*, 20:157–174.

Zwislocki, J. J. (1965). *Handbook of Mathematical Psychology.* Wiley, Wiley, NY.

THESIS PROCESSING SLIP

FIXED FIELD: ill ______ name ______

index ______ biblio ______

► COPIES: [✓ Archives] Aero Dewey [✓ Eng] Hum

Lindgren Music Rotch Science

TITLE VARIES ►☐ ______

NAME VARIES: ►☐ ______

IMPRINT (COPYRIGHT) ______

►COLLATION: 159 p.

►ADD. DEGREE: ______ ► DEPT.: ______

SUPERVISORS: ______

NOTES:

cat'r: date:

page: J150

►DEPT: E.E.

►YEAR: 1996 ►DEGREE: Ph.D.

►NAME: SHATZ, Lisa Fran